Article

The Global Phosphorylation Landscape of SARS-CoV-2 Infection

Graphical Abstract

Authors

Mehdi Bouhaddou, Danish Memon, Bjoern Meyer, ..., Danielle L. Swaney, Pedro Beltrao, Nevan J. Krogan

Correspondence

robert.grosse@pharmakol.uni-freiburg. de (R.G.), adolfo.garcia-sastre@mssm.edu (A.G.-S.), marco.vignuzzi@pasteur.fr (M.V.), jeffrey.johnson@mssm.edu (J.R.J.), kevan.shokat@ucsf.edu (K.M.S.), danielle.swaney@ucsf.edu (D.L.S.), pbeltrao@ebi.ac.uk (P.B.), nevan.krogan@ucsf.edu (N.J.K.)

In Brief

Phosphoproteomics analysis of SARS-CoV-2-infected Vero E6 cells reveals host cellular pathways hijacked by viral infection, leading to the identification of small molecules that target dysregulated pathways and elicit potent antiviral efficacy.

Highlights

- Phosphoproteomics analysis of SARS-CoV-2-infected cells uncovers signaling rewiring

- Infection promotes host p38 MAPK cascade activity and shutdown of mitotic kinases

- Infection stimulates CK2-containing filopodial protrusions with budding virus

- Kinase activity analysis identifies potent antiviral drugs and compounds

CelPress

Article

The Global Phosphorylation Landscape of SARS-CoV-2 Infection

Mehdi Bouhaddou,[1,2,3,4,21] Danish Memon,[5,21] Bjoern Meyer,[6,21] Kris M. White,[7,8,21] Veronica V. Rezelj,[6,21] Miguel Correa Marrero,[5,21] Benjamin J. Polacco,[1,2,3,4,21] James E. Melnyk,[1,2,4,9,21] Svenja Ulferts,[10,21] Robyn M. Kaake,[1,2,3,4,21] Jyoti Batra,[1,2,3,4,21] Alicia L. Richards,[1,2,3,4] Erica Stevenson,[1,2,3,4] David E. Gordon,[1,2,3,4] Ajda Rojc,[1,2,3,4] Kirsten Obernier,[1,2,3,4] Jacqueline M. Fabius,[1,2,3,4] Margaret Soucheray,[1,2,3,4] Lisa Miorin,[7,8] Elena Moreno,[7,8] Cassandra Koh,[6] Quang Dinh Tran,[6] Alexandra Hardy,[6] Rémy Robinot,[11,12] Thomas Vallet,[6] Benjamin E. Nilsson-Payant,[7] Claudia Hernandez-Armenta,[5] Alistair Dunham,[5] Sebastian Weigang,[13] Julian Knerr,[10] Maya Modak,[1,2,3,4] Diego Quintero,[1,2,3,4] Yuan Zhou,[1,2,3,4] Aurelien Dugourd,[14] Alberto Valdeolivas,[14] Trupti Patil,[1,2,3,4] Qiongyu Li,[1,2,3,4] Ruth Hüttenhain,[1,2,3,4] Merve Cakir,[1,2,3,4] Monita Muralidharan,[1,2,3,4] Minkyu Kim,[1,2,3,4] Gwendolyn Jang,[1,2,3,4] Beril Tutuncuoglu,[1,2,3,4] Joseph Hiatt,[1,2,3,4] Jeffrey Z. Guo,[1,2,3,4] Jiewei Xu,[1,2,3,4] Sophia Bouhaddou,[1] Christopher J.P. Mathy,[1,2,19] Anna Gaulton,[5] Emma J. Manners,[5] Eloy Félix,[5] Ying Shi,[1,2,4,9] Marisa Goff,[7] Jean K. Lim,[7] Timothy McBride,[15] Michael C. O'Neal,[15] Yiming Cai,[15] Jason C.J. Chang,[15] David J. Broadhurst,[15] Saker Klippsten,[15] Emmie De wit,[16] Andrew R. Leach,[5] Tanja Kortemme,[1,2,19] Brian Shoichet,[1,2] Melanie Ott,[3] Julio Saez-Rodriguez,[13] Benjamin R. tenOever,[7] R. Dyche Mullins,[1,2,4,8] Elizabeth R. Fischer,[16] Georg Kochs,[12,17] Robert Grosse,[9,17,18,*] Adolfo García-Sastre,[7,8,20,*] Marco Vignuzzi,[6,*] Jeffery R. Johnson,[7,*] Kevan M. Shokat,[1,2,4,9,*] Danielle L. Swaney,[1,2,3,4,*] Pedro Beltrao,[1,5,*] and Nevan J. Krogan[1,2,3,4,7,22,*]

[1]QBI COVID-19 Research Group (QCRG), San Francisco, CA 94158, USA
[2]Quantitative Biosciences Institute (QBI), University of California, San Francisco, San Francisco, CA 94158, USA
[3]J. David Gladstone Institutes, San Francisco, CA 94158, USA
[4]Department of Cellular and Molecular Pharmacology, University of California, San Francisco, San Francisco, CA 94158, USA
[5]European Molecular Biology Laboratory (EMBL), European Bioinformatics Institute, Wellcome Genome Campus, Hinxton, Cambridge, UK
[6]Viral Populations and Pathogenesis Unit, CNRS UMR 3569, Institut Pasteur, 75724 Paris, Cedex 15, France
[7]Department of Microbiology, Icahn School of Medicine at Mount Sinai, New York, NY 10029, USA
[8]Global Health and Emerging Pathogens Institute, Icahn School of Medicine at Mount Sinai, New York, NY, 10029, USA
[9]Howard Hughes Medical Institute
[10]Institute for Clinical and Experimental Pharmacology and Toxicology, University of Freiburg, Freiburg 79104, Germany
[11]Virus & Immunity Unit, Department of Virology, CNRS UMR 3569, Institut Pasteur, 75724 Paris, Cedex 15, France
[12]Vaccine Research Institute, 94000 Creteil, France
[13]Institute of Virology, Medical Center – University of Freiburg, Freiburg 79104, Germany
[14]Institute for Computational Biomedicine, Bioquant, Heidelberg University, Faculty of Medicine, and Heidelberg University Hospital, Heidelberg 69120, Germany
[15]Zoic Labs, Culver City, CA 90232, USA
[16]NIH/NIAID/Rocky Mountain Laboratories, Hamilton, MT 59840, USA
[17]Faculty of Medicine, University of Freiburg, Freiburg 79008, Germany
[18]Centre for Integrative Biological Signalling Studies (CIBSS), Freiburg 79104, Germany
[19]Department of Bioengineering & Therapeutic Sciences, University of California, San Francisco, San Francisco, CA 94158, USA
[20]The Tisch Cancer Institute, Icahn School of Medicine at Mount Sinai, New York, NY, 10029, USA
[21]These authors contributed equally
[22]Lead Contact
*Correspondence: robert.grosse@pharmakol.uni-freiburg.de (R.G.), adolfo.garcia-sastre@mssm.edu (A.G.-S.), marco.vignuzzi@pasteur.fr (M.V.), jeffrey.johnson@mssm.edu (J.R.J.), kevan.shokat@ucsf.edu (K.M.S.), danielle.swaney@ucsf.edu (D.L.S.), pbeltrao@ebi.ac.uk (P.B.), nevan.krogan@ucsf.edu (N.J.K.)
https://doi.org/10.1016/j.cell.2020.06.034

SUMMARY

The causative agent of the coronavirus disease 2019 (COVID-19) pandemic, severe acute respiratory syndrome coronavirus 2 (SARS-CoV-2), has infected millions and killed hundreds of thousands of people worldwide, highlighting an urgent need to develop antiviral therapies. Here we present a quantitative mass spectrometry-based phosphoproteomics survey of SARS-CoV-2 infection in Vero E6 cells, revealing dramatic rewiring of phosphorylation on host and viral proteins. SARS-CoV-2 infection promoted casein kinase II (CK2) and p38 MAPK activation, production of diverse cytokines, and shutdown of mitotic kinases, resulting in cell cycle arrest. Infection also stimulated a marked induction of CK2-containing filopodial protrusions possessing budding viral particles. Eighty-seven drugs and compounds were identified by mapping global phosphorylation profiles to dysregulated kinases and pathways. We found pharmacologic inhibition of the p38, CK2, CDK, AXL, and PIKFYVE kinases to possess antiviral efficacy, representing potential COVID-19 therapies.

Figure 1. Global Proteomics of Phosphorylation and Abundance Changes upon SARS-CoV-2 Infection

(A) Vero E6 cells were infected with SARS-CoV-2 (MOI 1.0). After 1 h of viral uptake, cells were harvested (0 h) or, subsequently, after 2, 4, 8, 12, or 24 h. As a control, Vero E6 cells were also mock infected for 1 h and harvested immediately thereafter (0 h) or after 24 h of mock infection. All conditions were performed in biological triplicate. Following cell harvest, cells were lysed, and proteins were digested into peptides. Aliquots of all samples were analyzed by mass spectrometry (MS) to measure changes in protein abundance upon infection, whereas the remaining sample was enriched for phosphorylated peptides and subsequently analyzed to measure changes in phosphorylation signaling. A DIA approach was used for all MS acquisitions. Last, all phosphorylation sites and protein identifiers were mapped to their respective human protein orthologs.

(B) Principal-component analysis (PCA) of phosphorylation replicates after removing outliers. See also Figure S1.

(C) Correlation of protein abundance (AB) and phosphorylation sites (PHs) between replicates within a biological condition (red) and across biological conditions (black). Boxplots depict median (horizonal lines), interquartile range (boxes), maximum and minimum values (vertical lines), and outliers (solid circles).

(D) Median AB of individual SARS-CoV-2 proteins in the protein AB analysis.

(E) The number of significantly regulated PH groups across the infection time course.

(F) Volcano plot of PH group quantification 24 h after infection.

(G) The number of significantly regulated proteins across the infection time course.

(H) Volcano plot of protein AB quantification 24 h after infection.

(I) Gene Ontology enrichment analysis of all significantly changing proteins in terms of AB divided into two sets: downregulated (blue) and upregulated (red).

(J) Proportion of significantly regulated PH groups with a correlated (i.e., same direction, AB match) or anticorrelated (i.e., opposite direction, AB mismatch) significant or insignificant (gray) change in protein AB.

In (E)–(H), all infection time points are compared with the mock infection at 0 h, and significantly regulated proteins are defined as (absolute value of $\log_2$(infection/mock) > 1 and adjusted $p < 0.05$ or when only detected in infected or mock based on replicate and MS feature counts; STAR Methods).

See also Figure S1.

and Mohr 2011). Gene Ontology enrichment analysis of significantly downregulated proteins revealed several terms related to platelet regulation (Figures 1I and S1F). Several downregulated host proteins are known to be involved in platelet regulation, thrombosis, and prevention of blood coagulation, including APOH, CD9, TSPAN14, AHSG, SERPINA1, and A2M (Mather et al., 2016; Mangin et al., 2009; Taggart et al., 2000). The downregulation of these proteins suggests that they may mechanisti-

cally contribute to symptoms of blood coagulation and stroke in COVID-19 patients (Han et al., 2020).

Lastly, the contribution of protein abundance to phosphorylation level changes was evaluated. For nearly all cases of a significantly changed phosphorylation site, no corresponding significant change in protein abundance was observed (Figure 1J), further suggesting that phosphorylation signaling represents a primary host response over this time course of infection as

opposed to transcriptional regulation, which would influence protein abundance.

Phosphorylation of SARS-CoV-2 Viral Proteins by the Host Proteome

Viral protein phosphorylation within the host cell may play a role in sensing and responding to cell state. We detected 25 phosphorylation sites in SARS-CoV-2 viral proteins that we combined with another proteomics dataset (Davidson et al., 2020) to amass a total of 49 sites detected across seven viral proteins (Table S2). Of note, this analysis does not distinguish cleaved from uncleaved viral proteins in the assignment of viral phosphorylation sites. The degree of conservation, indicative of functional constraint, was estimated for each residue position (Figure 2A; Ng and Henikoff 2003), and the sites were mapped to positions within structured regions for five proteins, with the majority observed in accessible positions (i.e., loops) (Figure 2B). The top kinase families predicted by sequence to regulate these sites included casein kinase II (CK2), cyclin-dependent kinase (CDK), and protein kinase C (PKC), among others (Figure 2C), suggesting that these kinases may contribute to regulation of viral replication.

Although it is unlikely that all phosphorylation sites on viral proteins play important functional roles, several sites in membrane (M) protein, Nsp9, and nucleocapsid (N) protein (Figures 2D–2F) suggest potential functionality. Five phosphorylation sites were detected in the M protein cluster within a short C-terminal region of the protein (207–215; Figure 2D). Although these acceptor residues are not predicted to be conserved, several are negatively charged residues in M proteins of other related viruses (Figure 2E). This evolutionary pattern suggests that a negative charge in this region may play a functional role, reminiscent of other multi-site phosphorylation events (Serber and Ferrell 2007).

To identify phosphorylation sites that may regulate protein-protein interactions, all sites were mapped to 3D structures, and solvent accessibility based protein-protein interface identification and recognition (SPPIDER) was used to assess whether sites resided within interface regions (Porollo and Meller 2007; Figure 2A; Table S2). The single phosphorylation site in Nsp9 was predicted to be at an interface region ("True"), which was supported by inspection of the homodimer structure (PDB: 6W4B). Additional phosphorylation sites were predicted to be at interface residues within the S protein (Figure 2A). However, inspection of S in complex with the ACE2 receptor (Shang et al., 2020; Lan et al., 2020) reveals some of these phosphorylation sites to be near but not at the interface region.

Finally, phosphorylation sites in N protein, a structural protein that binds to and assists with packaging viral RNA, were investigated. Most sites occurred within the N-terminal portion of the protein, at or near the RNA binding region, but avoided the C-terminal dimerization domain. The cluster of phosphorylation sites within an arginine/serine (RS)-dipeptide rich region, C-terminal to the RNA binding region (Figure 2A), is conserved in other coronavirus N proteins. This region is phosphorylated in SARS-CoV by serine-arginine (SR) protein kinases, modulating the role of SARS-CoV N protein in host translation inhibition (Peng et al., 2008). It is likely that phosphorylation of this same region in SARS-CoV-2 plays a similar role. Interestingly, *in vitro* inhibition

of SARS-CoV N protein phosphorylation at the RS-rich region results in reduced viral load and cytopathic effects (Wu et al., 2009), highlighting its importance for viral fitness. In addition, sites spanning the sequence of the RNA binding domain, which forms a claw-like structure, have been observed (Kang et al., 2020). Several phosphorylation sites cluster in the structural model, predicted to affect the surface charge of the so-called acidic wrist region (Figure 2F) but not the positive surface charge of the RNA binding pocket. We hypothesize that this surface charge difference may modulate N protein function, potentially via allosteric regulation of RNA binding capacity.

Phosphorylation of SARS-CoV-2 Host-Interacting Proteins during Infection

The recently published SARS-CoV-2 virus-human protein-protein interaction map identified 332 human proteins interacting with 27 (26 wild-type and 1 mutant) viral proteins (Gordon et al., 2020). Here we found some of these host proteins (40 of 332) to be significantly differentially phosphorylated upon infection (Figure 3). Virus-host protein-protein interactions could drive changes in phosphorylation by affecting host protein subcellular localization or by sterically blocking kinase access. Furthermore, phosphorylation of these proteins upon infection may signify an additional mode of functional control over these potential dependency and restriction factors.

The SARS-CoV-2 N protein is known to interact with several RNA-processing proteins that are differentially phosphorylated during infection, including LARP1 and RRP9. Here LARP1 phosphorylation decreases on several sites, which is known to consequently increase LARP1 affinity for 3′ untranslated regions (UTRs) of mRNAs encoding ribosomal proteins, driving inhibition of protein synthesis (Hong et al., 2017). This mechanism may be utilized by SARS-CoV-2 to prioritize synthesis of viral proteins over host proteins. In addition, ORF6 interacts with the NUP98/RAE complex, and NUP98 phosphorylation was observed to increase at S888, a site within its peptidase domain. NUP98 autocatalytic cleavage is required for localization to the nuclear pore; thus, it is possible that NUP98 interaction with ORF6 and/or its virus-induced phosphorylation prevents host mRNA export through the nuclear pore (Krull et al., 2010; Hodel et al., 2002). A similar mechanism is employed by vesicular stomatitis virus (VSV) matrix protein to block host mRNA export by targeting the NUP98/RAE complex, leading to exclusive translation of cytoplasmic VSV mRNAs (Quan et al., 2014).

For Nsp12, the majority of its protein interactors displayed decreased phosphorylation during infection. Because Nsp12 is known to encode the RNA-dependent RNA polymerase, responsible for replicating the viral genome, and several of these interacting proteins are related to RNA processing (LARP4B and CRTC3), their regulation may possess functional implications for Nsp12 in viral RNA replication. In addition, Nsp8 interacts with several proteins whose phosphorylation increases (LARP7 and MPHOSPH10) and decreases (CCDC86) on several sites. Notably, LARP7 and MEPCE are important regulators of RNA polymerase II-mediated transcription elongation as part of the 7SK small nuclear ribonucleoprotein particle (snRNP) complex. Regulation of these phosphorylation sites may contribute to
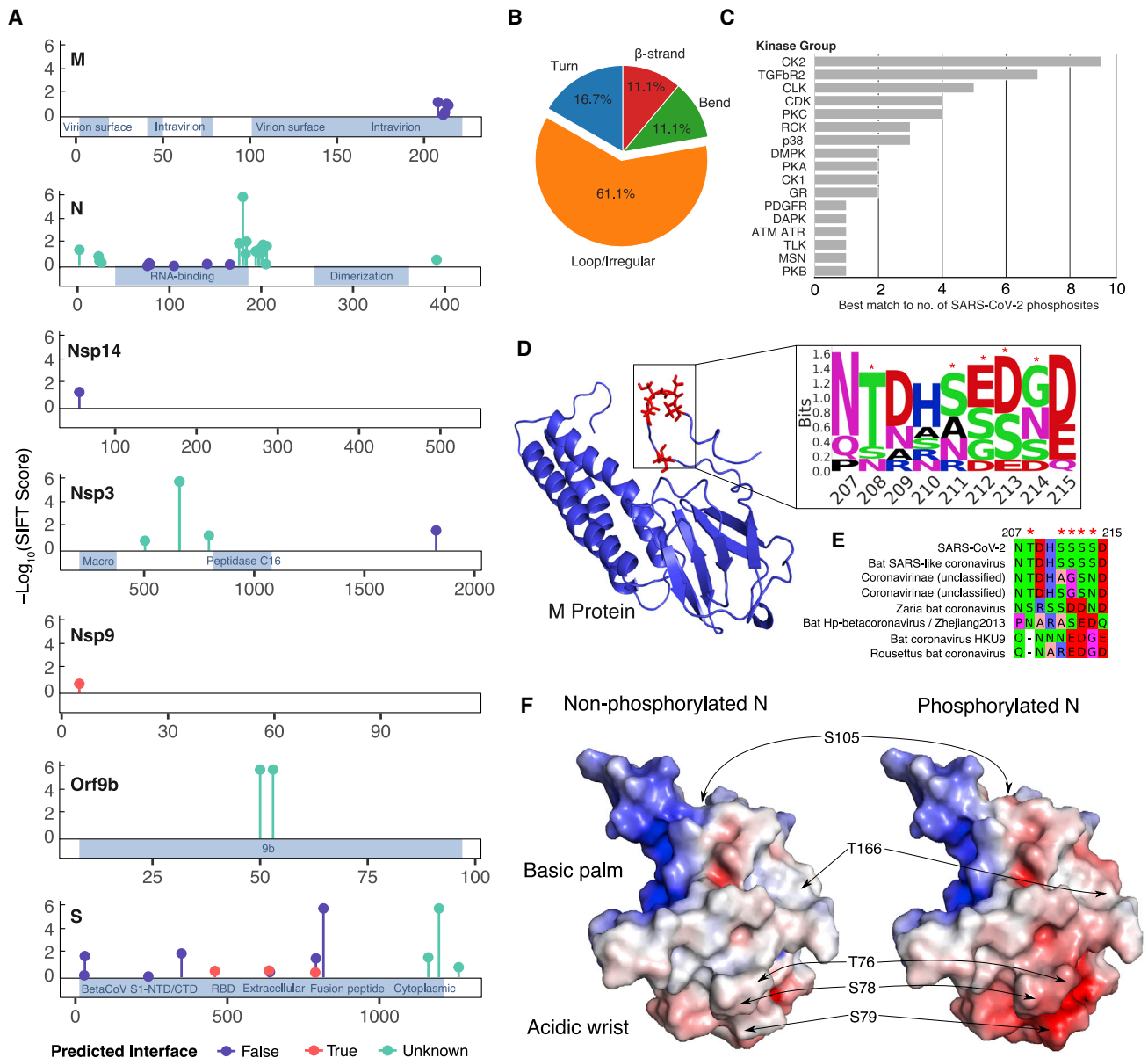
Figure 2. Overview of SARS-CoV-2 Viral Protein PHs in the Host Cell

(A) Localization of PHs across viral protein sequences from this study and a previous study (Davidson et al., 2020). Stem height indicates predicted deleteriousness of alanine substitutions. Dot color indicates whether the residue is (true) or is not (false) predicted to form part of an interaction interface based on SPPIDER analysis. Positions with no structural coverage are excluded from interface prediction.

(B) Distribution of secondary structure elements in which viral PHs were found, as classified by the define secondary structure of proteins (DSSP) tool.

(C) Distribution of top matching host kinases to viral PHs according to NetPhorest tool (Horn et al., 2014).

(D) Phosphorylation cluster in the C-terminal tail of the M protein (red residues) structure (Heo and Feig 2020) and associated sequence motif. Asterisks indicate PHs.

(E) Alignment of M protein phosphorylation clusters across different coronaviruses. Asterisks indicate PHs.

(F) Surface electrostatic potential of non-phosphorylated (left) and phosphorylated (right) RNA-binding domains of the N protein (PDB: 6M3M). Positions of PHs are indicated by arrows. Blue denotes a positive charge potential, and red indicates a negative charge potential. Electrostatic potential was computed with the Advanced Poisson-Boltzmann Solver (APBS) tool after preparation with the PDB2PQR tool.

the regulation of positive transcription elongation factor b (P-TEFb [CDK9]) and transcriptional regulation of the virus, similar to how these proteins are regulated during HIV infection (Mbonye et al., 2015).

SARS-CoV-2 Infection Regulates Host Kinase Signaling

To study global changes in kinase signaling and their effect on host protein phosphorylation, regulated phosphorylation sites were grouped in five clusters based on their dynamics using a

Figure 3. Phosphorylation on SARS-CoV-2 Virus-Human Interacting Proteins

The SARS-CoV-2 virus-host protein-protein interaction map (Gordon et al., 2020) found 332 human proteins interacting with 27 (26 wild-type and 1 mutant) viral proteins. Here we found 40 of 332 proteins significantly differentially phosphorylated across at least two time points (adjusted p < 0.05 and absolute value of $\log_2$ fold change [abs($\log_2$FC)] > 1). Viral proteins are shown as red diamonds. Interacting human proteins are shown as gray circles. PHs emanate from human proteins, colored by their $\log_2$ fold change compared with uninfected control samples (red, increase; blue, decrease) at each time point (0, 2, 4, 8, 12, and 24 h after infection) in a clockwise fashion. An interactive version of phosphorylation data can be found at https://kroganlab.ucsf.edu/network-maps.

data-driven clustering approach (Figure 4A; STAR Methods). For each of the groups, an enrichment analysis was performed for functions and pathways (Figure 4A; Table S3). The dynamics of these changes can be linked to the viral life cycle: entry (0–2 h), replication (4–12 h), and egress (24 h). Clusters 1 and 2 include phosphorylation sites that are, on average, upregulated during infection. Cluster 1 sites tended to be upregulated within 2 h

(i.e., linked to viral entry) and were enriched in mRNA processing, cell cycle, apoptosis, and proteins involved in HIV infection. Cluster 2 included apoptosis proteins with later onset of phosphorylation, associated with replication and/or egress. Phosphorylation sites in clusters 3 and 4 were downregulated and enriched in RNA-processing functions. Sites within cluster 5 possessed a dynamic response to infection, with immediate

Figure 4. Signaling Changes in Host Cells in Response to SARS-CoV-2 Infection

(A) Clusters of significantly changing PHs (abs(log$_2$FC) > 1 and adjusted p < 0.05) across the time course of infection with non-redundant enriched Reactome pathway terms (adjusted p value [q] < 0.01) for each cluster. Horizontal red lines below each pathway term correspond to phosphorylated proteins belonging to the pathway, and a black-bordered rectangle is indicative of a significantly enriched term.

(B) Kinases depicting a strong change in activity upon infection (abs(log$_{10}$(p)) > 2.5) in at least one time point, with predicted activity in at least 5 of 6 time points.

(C) Schematic representation of interaction between host kinases and SARS-CoV-2 viral proteins from Gordon et al. (2020). Substrate PHs for each kinase are color-coded as blue (up) and red (down) based on the direction of change during infection. Only PHs corresponding to the kinase activity direction are shown.

(legend continued on next page)

downregulation followed by a rise during the middle and renewed downregulation at late time points. This cluster was enriched for DNA replication and the cell cycle, among others. These observations are corroborated by standard Gene Ontology (GO) enrichment analyses of biological processes regulated by phosphorylation (Figure S1G; Table S3; STAR Methods).

We estimated activity regulation for 97 kinases based on the regulation of their known substrates (Ochoa et al., 2016; Hernandez-Armenta et al., 2017; Table S4), with the strongest regulation linked to viral entry (0–2 h) and late replication/egress (24 h). The kinases predicted to be most strongly activated (Figures 4B and S2A) include several members of the p38 pathway, including p38γ (MAPK12), CK2 (CSNK2A1/2), Ca^{2+}/calmodulin-dependent protein kinase (CAMK2G), and the guanosine monophosphate (GMP)-dependent protein kinases PRKG1/2, which can inhibit Rho signaling. Kinases predicted to be downregulated include several cell cycle kinases (CDK1/2/5 and AURKA), cell growth-related signaling pathway kinases (PRKACA, AKT1/2, MAPK1/3, and PIM1), and the cytoskeleton regulators (PAK1), among others. Kinase activity estimates based on the 24-h mock control gave highly correlated results (r = 0.81), identifying the same set of highly regulated kinases (Figure S2D). Some of the changes in kinase activity can be directly linked to host-viral protein interactions (Figure 4C). Among the 10 interacting kinases detected in a virus-host protein-protein interaction map (Gordon et al., 2020), an increase in activity for CK2 and a decrease for MARK2 and PRKACA were observed (Figure 4C). Of note, although we predict decreased activity for PRKACA based on phosphorylation of its substrates, we simultaneously detected a significant increase in T198 phosphorylation (8, 12, and 24 h post infection) within its activation loop, suggesting an increase in PRKACA activity. It is possible that Nsp13 is sequestering active PRKACA away from its typical substrates.

To better understand the signaling states of cells over the course of infection, we compared our data with a compilation of public phosphoproteomics datasets of other conditions (Ochoa et al., 2016; Figures 4D and S2B). The first and last time point of infection resembled a kinase activation state induced by inhibition of mTOR, ERK, AKT, and EGFR, consistent with the estimated kinase activities of these growth-related pathways. Between 2 and 12 h after infection, kinase activity states resembling inhibition of phosphatidylinositol 3-kinase (PI3K), p70S6K, and Rho-associated protein kinases (ROCKs) were observed. Finally, several of the time points resembled S/G2 cell cycle state, suggestive of a cell cycle block. Conversely, some conditions were anticorrelated with kinase activity profiles (Figures 4D and S2B). In line with an S/G2 cell-cycle block, infection signaling appeared opposite to that of a mitotic cell. In addition, inhibitors of histone deacetylases (HDACs) (scriptaid and trichostatin A), the proteasome (bortezomib), Hsp90 (geldanamycin), and voltage-gated sodium channels (valproic acid)

were also anticorrelated. These drugs, or drugs targeting these protein activities, could induce a signaling state that inhibits viral replication.

To further link kinase activities to downstream protein complexes, enrichment of up- or downregulated phosphorylation sites was determined within a curated set of human protein complexes defined by CORUM (Giurgiu et al., 2019; Figures 4E and S2C). This analysis revealed significant changes in phosphorylation of splicing related complexes (spliceosome), the proteasome (PA700-20S-PA28), and chromatin remodeling complexes (HuCHRAC and MLL2). In addition, a subset of regulated phosphorylation sites were detected that have known regulatory functions or high predicted functional scores (Ochoa et al., 2020) that are linked to regulation of protein activities (Table S5). Consistent with the observed signaling changes described above, these regulatory phosphorylation sites are involved in activation of chaperones (including HSP90), proteasome activity, inhibition of the anaphase-promoting complex (APC), and regulation of HDACs and cytoskeleton proteins, among others.

CK2 and N Co-localize at Virus-Induced Filopodial Protrusions

The phosphoproteomics data indicated regulation of several kinases and effector proteins related to cytoskeleton organization upon SARS-CoV-2 infection. Kinases downstream of the Rho/Rac/Cdc42 GTPases (PAK1/2 and ROCK1/2) and several well-characterized phosphorylation site targets of PAK1/2 kinase in vimentin (VIM S39 and S56) and stathmin (STMN1 S16 and S25) were found to be downregulated during infection (Figures 5A and 5B). The interaction of Nsp7 with RHOA (Gordon et al., 2020) may contribute to this downregulation. In contrast, signaling via CK2 is strongly upregulated, as determined by the increase in phosphorylation of well-characterized target sites (Figures 5A and 5B). Among the many roles of this kinase, we noted increased phosphorylation of cytoskeleton protein targets such as α-Catenin (CTNNA1 S641) and the heavy chain of the motor protein Myosin IIa (MYH9 S1943). In addition to these kinase-mediated effects, the Nsp2 protein of SARS-CoV-2 also interacts directly with strumpellin (WASHC5), a subunit of the actin assembly-inducing WASH complex (Gordon et al., 2020), further implicating cytoskeleton regulation during infection. To study the relevance of these observations in a human infection model, high-resolution immunofluorescence imaging of fixed Caco-2 human colon epithelial cells was performed 24 h after infection (STAR Methods).

SARS-CoV-2 infected Caco-2 cells were imaged for filamentous actin and the SARS-CoV-2 M protein, revealing prominent M protein clusters, possibly marking assembled SARS-CoV-2 viral particles, localized along the shafts and at the tips of actin-rich filopodia (Figures 5B and S3B). SARS-CoV-2 infection induced a dramatic increase in filopodial protrusions, which were significantly longer and more branched than in uninfected

(D) Correlation of kinase activity profiles of each time point with other biological conditions with at least one significantly changing kinase (abs(log_{10}(p)) > 2.5) and having significant correlation with at least one time-point (false discovery rate [FDR] < 5%).

(E) Overall phosphorylation change ($-log_{10}$(p)) of a protein complex, estimated as the change in phosphorylation on member proteins. Only non-redundant protein complexes with a significant change in phosphorylation (abs(log_{10}(p)) > 2.5) in at least one time point are shown.

See also Figure S2.
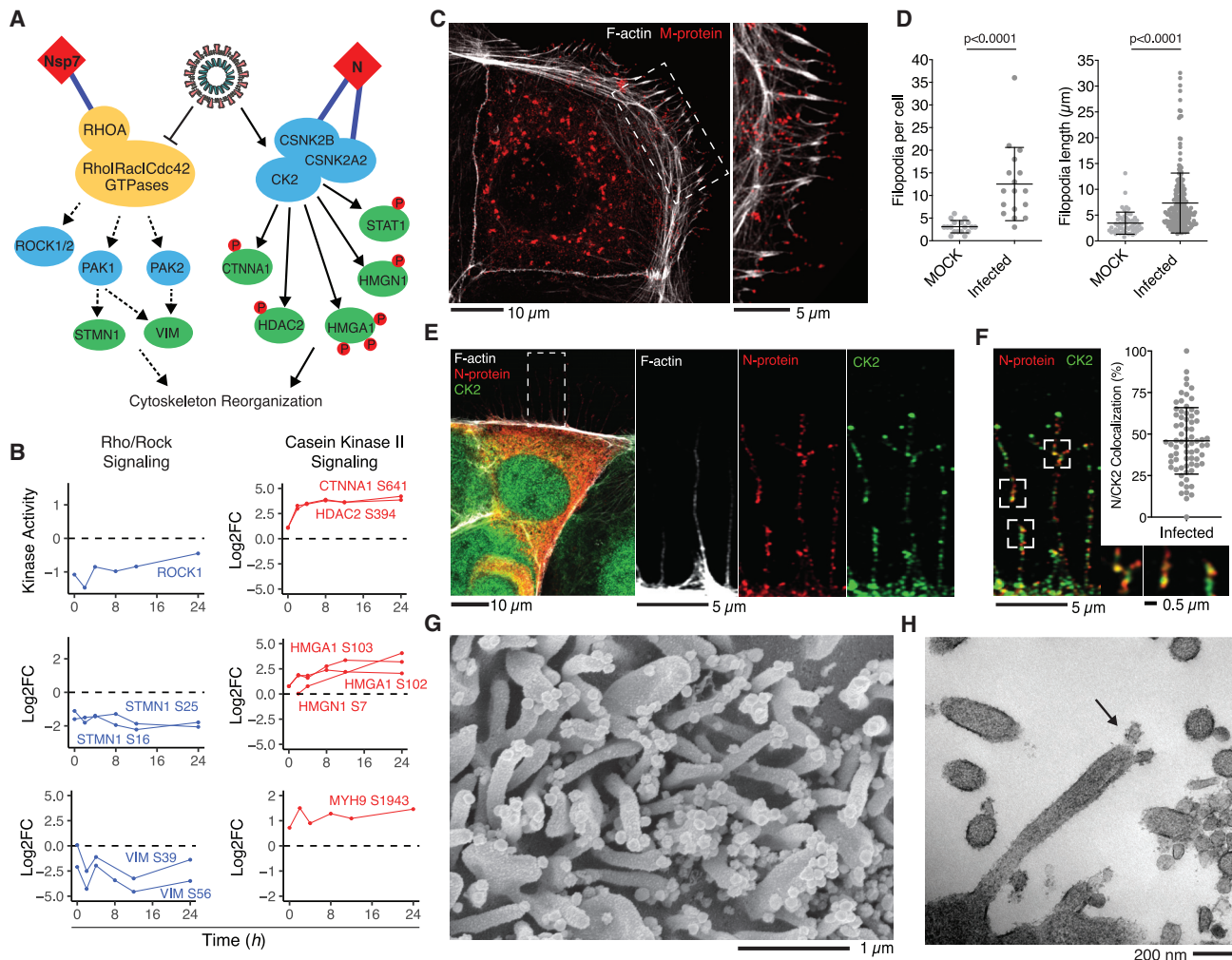
Figure 5. Colocalization of CK2 and Viral Proteins at Actin Protrusions

(A) Pathway of regulated PHs and SARS-CoV-2 interaction partners involved in cytoskeletal reorganization. Dashed lines indicate downregulation of activity, while solid lines indicate upregulation of activity.

(B) Regulation of individual kinase activity or PHs depicted in (A).

(C) Caco-2 cells infected with SARS-CoV-2 at an MOI of 0.1 for 24 h prior to immunostaining for F-actin and M protein, as indicated. Shown is a confocal section revealing M protein localization along and to the tip of filopodia (left) and magnification of the dashed box (right).

(D) Dot plot quantification of the number and length of filopodia in untreated (mock) or infected Caco-2 cells for 24 h with SARS-CoV-2. Filopodium length was measured from the cortical actin to the tip of the filopodium. Error bars represent SD. Statistical testing by Mann-Whitney test.

(E) Caco-2 cells infected with SARS-CoV-2 at an MOI of 0.01 for 24 h prior to immunostaining for F-actin, N protein, and casein kinase II (CK2) as indicated (left). Shown is magnification of the dashed box as single channels (right).

(F) Magnification of the dashed box from (E) with quantification of colocalization between CK2 and N protein throughout infected Caco-2 cells. Displayed is the proportion of N protein-positive particles colocalizing with CK2. Error bars represent SD.

(G and H) Scanning electron microscopy (G) and transmission electron microscopy (H) images of SARS-CoV-2 budding from Vero E6 cell filopodia (black arrow in H).

See also Figure S3.

cells (Figure 5D). Uninfected cells also exhibited filopodial protrusions, but their frequency and shape were dramatically different (Figure S3A). Reorganization of the actin cytoskeleton is a common feature of many viral infections and is associated with different stages of the viral life cycle (Taylor et al., 2011).

We hypothesize that induction of virus-containing filopodia could be important for SARS-CoV-2 egress and/or cell-to-cell spread within epithelial monolayers. Given that Rho/PAK/

ROCK signaling is downregulated, we next asked whether CK2 could play a role in this process. At 24 h, infected cells showed CK2 expression along the thin filopodial protrusions (Figure 5E), partially co-localized with SARS-CoV-2 N protein (Figure 5F). Scanning and transmission electron microscopy were used (Figures 5G, 5H, S3C, and S3D) to image the cellular protrusions at higher resolution. Assembled viral particles are clearly visible along these filopodia (Figure 5G), with instances where the viral
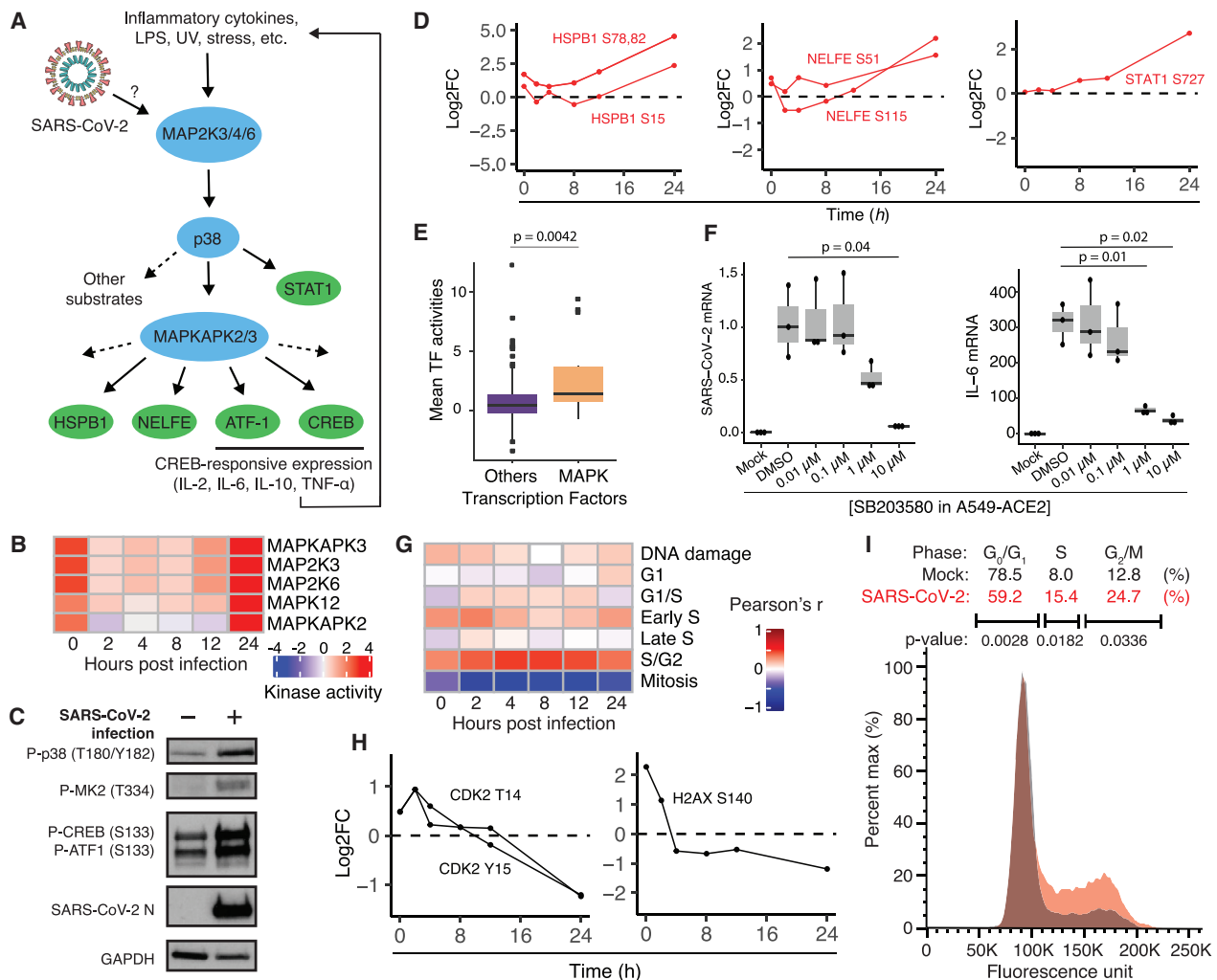
Figure 6. SARS-CoV-2 Activates the p38/MAPK Signaling Pathway and Causes Cell Cycle Arrest

(A) Diagram of the p38/MAPK signaling pathway.

(B) Kinase activity analysis for kinases in the p38/MAPK pathway.

(C) Western blot analysis of phosphorylated p38/MAPK signaling components in mock- and SARS-CoV-2-infected ACE2-A549 cells 24 h after infection.

(D) Log_2 fold change profiles of indicated p38/MAPK substrates during SARS-CoV-2 infection in Vero E6 cells.

(E) Transcription factor activity analysis of SARS-CoV-2-infected A549, Calu-3, and NHBE cells, comparing p38/MAPK transcription factors with transcription factors not associated with the p38/MAPK pathway. Statistical test: Mann-Whitney test.

(F) qRT-PCR analysis of the indicated mRNA from ACE2-A549 cells pre-treated with the p38 inhibitor SB203580 at the indicated concentrations for 1 h prior to infection with SARS-CoV-2 for 24 h. Statistical test: Student's t test. See also Figures S4 and S5.

(G) Heatmap of Pearson's correlation coefficients comparing SARS-CoV-2-infected Vero E6 phosphorylation profiles with profiles of cells with induced DNA damage and cells arrested at the indicated cell cycle stages.

(H) Log_2 fold change profiles of the indicated cell cycle and DNA damage substrates during SARS-CoV-2 infection in Vero E6 cells.

(I) DNA content analysis of cells infected with SARS-CoV-2 for 24 h compared with mock-infected cells.

particles appear to be budding from the protrusions (Figure 5H). Finally, we performed a global phosphoproteomics analysis of Vero E6 cells overexpressing N protein and observed CK2 activity to be significantly upregulated (Figure S3E; Tables S1 and S4). Because CK2 activity can promote actin polymerization (D'Amore et al., 2019), we hypothesize that N protein may allosterically control CK2 activity and regulate cytoskeleton organization.

SARS-CoV-2 Infection Promotes p38/MAPK Signaling Activity and Cell Cycle Arrest

Kinase activity analysis of SARS-CoV-2 phosphorylation profiles predicted upregulation of several components of the p38/mitogen-activated protein kinase (MAPK) signaling pathway, including MAP2K3, MAP2K6, MAPK12, MAPKAPK2 (MK2), and MAPKAPK3 (Figures 6A and 6B). Immunoblotting for activated phospho-p38 (T180/Y182), phospho-MK2 (T334), and
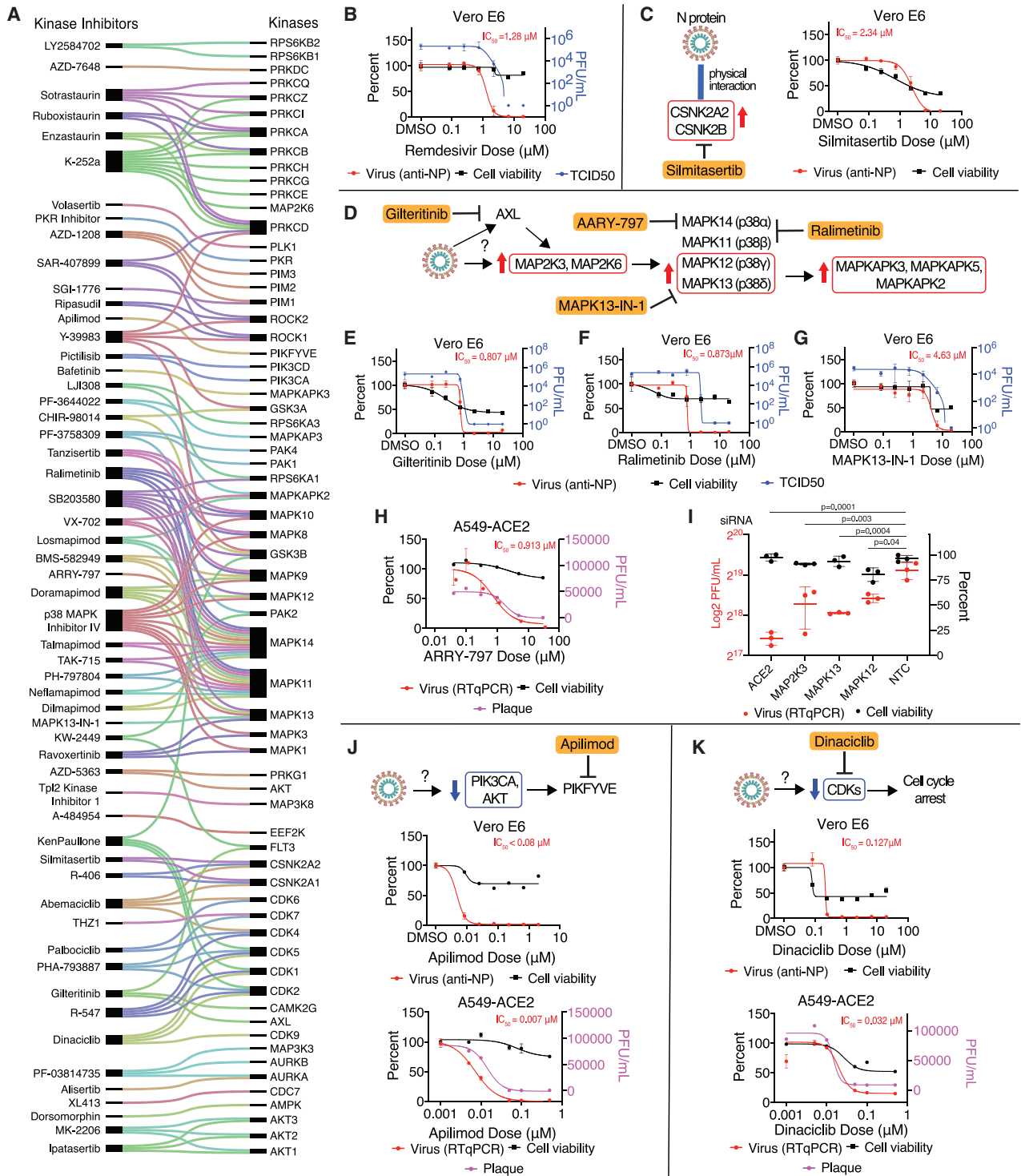
Figure 7. Mapping Regulated Kinases to Kinase Inhibitors Identifies SARS-CoV-2 Therapies

(A) Kinase inhibitors (left) mapped to kinases (right) whose activity was regulated by SARS-CoV-2 infection. Lines connecting them indicate known kinase targets for each drug/compound.

(B) Vero E6 cells pre-treated with remdesivir at the indicated doses, followed by SARS-CoV-2 infection for 48 h. Percent viral titer compared with mock drug treatment (anti-NP antibody; red line, dots, and text) and cell viability (black) is depicted. Error bars represent SD.

(C) As in (B). Vero E6 cells were treated with the CK2 inhibitor silmitasertib. Physical interactions between N protein and the CSNK2A2 and CSNK2B CK2 subunits were observed in a prior study (Gordon et al., 2020).

(legend continued on next page)

phospho-cAMP response element-binding protein (CREB) and phospho-ATF-1 at their respective MAPKAPK2 sites (S133 in both) confirmed activation of the p38/MAPK pathway during SARS-CoV-2 infection in ACE2-expressing A549 human lung carcinoma cells (ACE2-A549) (Figure 6C). Furthermore, phosphoproteomics data depict increased phosphorylation of p38 pathway substrates such as negative elongation factor E (NELFE), heat shock protein beta-1 (HSPB1), and signal transducer and activator of transcription 1-alpha/beta (STAT1), among others (Figure 6D). Regulation of these sites occurs late in the time course (24 h after infection), likely reflecting a more advanced stage of viral infection, replication, and egress.

The p38/MAPK pathway mediates the cellular response to environmental stress, pathogenic infection, and pro-inflammatory cytokine stimulation, whereas downstream effectors of the pathway include transcription factors and RNA binding proteins that promote inflammatory cytokine production (Cuadrado and Nebreda 2010; Wen et al., 2010). Analysis of estimated transcription factor activity from gene expression data (STAR Methods; Table S6) derived from the infection of a human lung carcinoma cell line (A549), a human epithelial lung cancer cell line (Calu3), and primary human bronchial epithelial (NHBE) cells demonstrated that transcription factors regulated by the p38/MAPK pathway were among the most highly activated upon infection (Figure 6E; Blanco-Melo et al., 2020).

To investigate the contribution of the p38/MAPK pathway to cytokine production, SARS-CoV-2-infected ACE2-A549 cells were treated with the p38 inhibitor SB203580. The mRNA of the inflammatory cytokines interleukin-6 (IL-6), tumor necrosis factor alpha (TNF-α), and others increased during infection and were inhibited by p38 inhibition in a dose-dependent manner (Figures 6F, right, and S4A). Interestingly, p38 inhibition also reduced SARS-CoV-2 subgenomic mRNA (Figure 6F, left) in the absence of major cellular toxicity (Figure S5), indicative of reduced viral replication. The SB203580-induced decrease in virus production was further confirmed using an anti-SARS-CoV-2 N protein (anti-NP) antibody-based assay (Figure S5, New York Vero E6). Multiplexed ELISA analysis of supernatants of cells from the same experiment demonstrated strong upregulation of inflammatory cytokines at the protein level, including IL-6, CXCL8, CCL20, and CCL2, which were decreased upon p38 inhibition (Figure S4B; Table S7). However, because SARS-CoV-2 replication is also inhibited by SB203580, we cannot deconvolve the contributions of p38/MAPK pathway activity and SARS-CoV-2 virus presence on cytokine production.

Comparing phosphoproteomics profiles of SARS-CoV-2-infected cells with a database of phosphorylation profiles collected at specific cell cycle stages, viral infection was most highly correlated with cells arrested at the S/G2 transition and was negatively correlated with profiles of cells in mitosis (Figure 6G). We also observed SARS-CoV-2-dependent regulation of CDK2 T14/Y15 phosphorylation, initially increased in response to SARS-CoV-2 infection at 2 h, followed by a decrease over the remainder of the infection time course (Figure 6H, left). CDK2 activity promotes transition from the G2 phase of the cell cycle into mitosis and is inhibited by phosphorylation at positions T14 and Y15 by kinases WEE1 and MYT1, preventing premature entry into mitosis (Parker and Piwnica-Worms 1992; Mueller et al., 1995). CDK2 can also become phosphorylated when the cell cycle is arrested because of checkpoint failure or DNA damage. In addition, H2AX S140 phosphorylation (i.e., γ-H2AX), a hallmark of the DNA damage response, exhibited a profile similar to CDK2, suggesting that the DNA damage response may become activated early during infection (Rogakou et al., 1998; Figure 6H, right).

To more directly test whether SARS-CoV-2 infection affects cell cycle progression, cells were infected with SARS-CoV-2 for 24 h, and their DNA content was measured using DAPI DNA staining and flow cytometry. A significant increase in the fraction of cells in S phase and at the G2/M transition and a decrease in the fraction of cells in G0/G1 phase were observed (Figures 6I and S4C). This observation is consistent with arrest between S and G2 phases of the cell cycle. A relationship between p38 activity and cell cycle arrest has been described previously, and the two could be linked mechanistically during SARS-CoV-2 infection (Lee et al., 2002; Yee et al., 2004).

Mapping Kinase Activities to Pharmacological Modulators Identifies SARS-CoV-2 Therapies

To identify effective therapies for SARS-CoV-2 infection, kinase inhibitors were mapped to the most differentially regulated kinase activities (Figure 7A) and to specific phosphorylation sites (Table S8; STAR Methods). This resulted in a list of 87 drugs and compounds: 10 FDA-approved, 53 undergoing clinical testing, and 24 pre-clinical. Many of the drugs and compounds identified were reported to target several host kinases in cell-free assays at a minimum, but many have been observed to hit targets in cellular assays as well (Figure 7A). We reasoned that testing molecules with both overlapping and unique targets would help specify the molecular targets of greatest importance for SARS-CoV-2. Here, 68 total drugs and compounds were tested for antiviral efficacy (via qRT-PCR, anti-NP antibody, plaque assay, and/or TCID$_{50}$) and cellular toxicity at two different institutions (in New York [Mount Sinai, 25 drugs/compounds] and Paris [Institut Pasteur, 62]) and in two cell lines (Vero E6 [68] and

(D) Predicted increased kinase activity for the p38 signaling pathway and drugs/compounds targeting pathway members (ralimetinib, MAPK13-IN-1, and ARRY-797) and upstream drivers (gilteritinib).

(E–G) As in (B). Vero E6 cells treated with the AXL inhibitor gilteritinib (E), the MAPK11/14 inhibitor ralimetinib (F), or the MAPK13 inhibitor MAPK13-IN-1 (G) prior to SARS-CoV-2 infection.

(H) A549-ACE2 lung epithelial cells were treated with the MAPK14 inhibitor ARRY-797 prior to SARS-CoV-2 infection.

(I) Small interfering RNA (siRNA) knockdown of p38 pathway genes in A549-ACE2 leads to a significant decrease in SARS-CoV-2 viral replication (red), as assessed by qRT-PCR in the absence of effects on cell viability (black). ACE2 and non-targeting siRNAs are included as positive and negative controls, respectively.

(J and K) Vero E6 or A549-ACE2 cells were treated with PIKFYVE inhibitor apilimod (J) or the CDK inhibitor dinaciclib (K) prior to SARS-CoV-2 infection.

See also Figure S6.

A549-ACE2 [61]). All pharmacological profiling results can be found in Figure S5 and Table S8.

We found pharmacological inhibitors of CK2, p38 MAPK signaling, PIKFYVE, and CDKs to possess strong antiviral efficacy. Cells were pre-treated with inhibitor molecules, followed by SARS-CoV-2 infection (STAR Methods), and virus quantity (anti-NP antibody against SARS-CoV-2) and cell viability were quantified 48 h after infection. As a positive control and for comparison, remdesivir was tested, and the expected favorable antiviral activity was observed (half maximal inhibitory concentration [IC_{50}] = 1.28 μM; Figure 7B). Silmitasertib, an inhibitor of CSNK2A1 and CSNK2A2, was found to possess antiviral activity (IC_{50} = 2.34 μM; Figures 7C and S5). In conjunction with data supporting physical interaction (Gordon et al., 2020) and co-localization with N protein (Figure 5F), as well as a potential role in remodeling extracellular matrix upon infection (Figures 5 and S3), CK2 signaling appears to be an important pathway hijacked by SARS-CoV-2. Furthermore, silmitasertib is currently being considered for human testing as a potential treatment for COVID-19.

To probe SARS-CoV-2 dependence on MAPK signaling, SARS-CoV-2 replication was measured in response to pharmacological and genetic perturbation of MAPK components that were upregulated during infection (Figure 7D). Potent antiviral activity was observed for gilteritinib (Figure 7E; IC_{50} = 0.807 μM), an inhibitor of AXL kinase, upstream of p38; ralimetinib (Figure 7F; IC_{50} = 0.873 μM), an inhibitor of MAPK11 (p38α) and MAPK14 (p38β); MAPK13-IN-1 (Figure 7G; IC_{50} = 4.63 μM), an inhibitor of MAPK13 (p38-δ); and ARRY-797 (Figure 7H; IC_{50} = 0.913 μM) in A549-ACE2 cells, a MAPK14 inhibitor. To further probe the dependence of SARS-CoV-2 on p38 pathway members, small interfering RNA (siRNA)-mediated knockdown of MAP2K3, p38-δ (MAPK13), and p38-γ (MAPK12) was performed in A549-ACE2 cells, and a significant decrease in SARS-CoV-2 replication was observed for all three, with little to no effect on cell viability (Figure 7I).

In addition, we noted marked regulation of phosphatidylinositol enzyme activities for PIK3CA, PLCB3, and PIKFYVE, suggesting a potential role for the appropriate balance of phosphatidylinositol species. To target this process, apilimod, a small-molecule inhibitor of PIKFYVE, was tested and found to possess strong antiviral activity in two cell lines (Vero E6, IC_{50} < 0.08 μM; A549-ACE2, IC_{50} = 0.007 μM), corroborated by a recent study (Ou et al., 2020; Figure 7J). Lastly, we noted pronounced regulation of CDK signaling pathways (Figure 4B) and cell cycle stage (Figure 6I) during viral infection, suggesting that the virus may regulate the cell cycle to enhance viral replication. Accordingly, strong antiviral activity for the CDK inhibitor dinaciclib was observed across two cell lines (Vero E6, IC_{50} = 0.127 μM; A549-ACE2, IC_{50} = 0.032 μM) (Figure 7K).

DISCUSSION

We used a mass spectrometry-based approach to study perturbations in protein abundance and phosphorylation during SARS-CoV-2 infection. Viral proteins increased, starting 8 h after infection, indicative of viral replication, whereas only small changes in host protein abundance were observed within 24 h. In contrast, large changes were observed in protein phosphorylation, highlighting the degree by which the virus makes use of the host post-translational regulatory systems to promote rapid changes in cellular signaling.

Changes in phosphorylation reflect altered activities of kinases that are hijacked during the infection. Based on changes in phosphorylation of their annotated substrates, we estimated changes in activity of 97 of the 518 human kinases. The changes in kinase activity offer insights into the biology of viral infection. Kinases represent ideal drug targets; here, we identified kinases and pathways altered by SARS-CoV-2 infection that can be targeted by 87 FDA-approved drugs and compounds in clinical trials or in preclinical development (Table S8).

The most strongly regulated kinases fall into a set of signaling pathways that include p38/MAPK signaling, AKT and ERK signaling, Rho GTPase and CK2 cytoskeleton signaling, and cell cycle regulation. The downregulation of ROCK and PAK kinase activity and upregulation of CK2 cytoskeleton-related targets suggest virus-induced changes in cytoskeleton organization. Imaging of infected cells revealed formation of actin-rich filopodia containing viral proteins. Higher-resolution electron microscopy data confirm the presence of assembled viral particles in these structures. Many viruses, including vaccinia, Ebola, and Marburg, hijack the host cell cytoskeleton to promote egress and rapid cell-to-cell spread across epithelial monolayers. Vaccinia promotes Arp2/3-dependent actin assembly, producing a filopodial protrusion with a virus at the tip (Leite and Way 2015). In contrast, Marburg virus hijacks the unconventional motor protein Myosin X, which promotes filopodium formation and traffics the virus along the filopodium shaft. The SARS-CoV-2 protein clusters peppered throughout the length of filopodial protrusions more closely resemble Marburg than vaccinia, but additional work is required to understand whether SARS-CoV-2 makes use of either Myosin X motor activity or actin filament assembly to move along filopodia. CK2 is known to phosphorylate myosin proteins at endocytic sites to drive actin polymerization (Fernández-Golbano et al., 2014). Furthermore, CK2 has been found to regulate actin tail formation during vaccinia virus infection, enabling efficient cell-to-cell spread of the virus (Alvarez and Agaisse 2012; Smith and Law 2004). Here the CK2 inhibitor silmitasertib displayed robust antiviral activity, suggesting a role of this kinase in regulating the SARS-CoV-2 life cycle.

In addition, kinase activity profiling analysis shows that CDK1/2 activities are significantly reduced by SARS-CoV-2 infection, leading to a S/G2 phase arrest that is similar to infectious bronchitis virus (IBV), a prototypical coronavirus (Dove et al., 2006; Li et al., 2007a), and other RNA viruses (Lilley et al., 2007; Ariumi et al., 2008). Arresting cells in S/G2 phase may provide benefits for viral replication and progeny production by ensuring an abundant supply of nucleotides and other essential host DNA repair/replication proteins (Chaurushiya and Weitzman 2009).

The predicted increase in p38/MAPK activity led us to investigate the effects of p38/MAPK inhibition on pro-inflammatory cytokine production and viral replication in SARS-CoV-2-infected cells. Recent immunological studies have indicated that increased IL-6, IL-10, and TNF-α and lymphopenia are associated with severe COVID-19 cases (Pedersen and Ho 2020).

The p38/MAPK pathway responds to and controls production of potentially harmful pro-inflammatory cytokines. Several pathogenic viral infections induce a p38/MAPK signaling state that exhibits uncontrolled positive feedback regulation, leading to excessive inflammation associated with severe disease. Inhibition of p38/MAPK signaling suppressed the overproduction of inflammatory cytokines induced by several viral infections, including SARS-CoV, Dengue virus, and influenza A virus, improving survival in mice (Fu et al., 2014; Growcott et al., 2018; Jimenez-Guardeño et al., 2014). However, p38/MAPK inhibition did not directly impair the virus in these cases but, instead, the host's immune response to the infection. In contrast, during SARS-CoV-2 infection, p38/MAPK inhibition suppressed cytokine production and impaired viral replication by a still unknown mechanism, suggesting that p38/MAPK inhibition may target multiple mechanisms related to COVID-19 pathogenesis.

We tested 68 drugs and compounds and found antiviral activity for several that are FDA approved, in clinical testing, or under preclinical development for various diseases, including silmitasertib (CK2, phase 2), gilteritinib (AXL, FDA approved), ARRY-797 (p38, phase 2/3), MAPK13-IN-1 (p38, preclinical), SB203580 (p38, preclinical), ralimetinib (p38, phase 2), apilimod (PIKFYVE, phase 1), and dinaciclib (CDK, phase 3), among others (Figure S5; Table S8). Silmitasertib, a small molecule undergoing clinical trials for various cancers, is now being considered for testing in humans to combat COVID-19. Although the effectiveness of CK2 inhibition may be attributed to its regulation of stress granules (Gordon et al., 2020), viral egress and dissemination could be facilitated by CK2-mediated remodeling of the extracellular matrix (Figure 5).

Ralimetinib is currently in phase 2 clinical trials for treatment of ovarian cancer (Patnaik et al., 2016), and ARRY-797 is in phase 3 clinical trials for treatment of cardiomyopathy. The antiviral activity observed for gilteritinib, an FDA-approved drug for treatment of acute myeloid leukemia, is supported by involvement of another AXL inhibitor, bencentinib, in the RECOVERY COVID-19 clinical trial in the United Kingdom. AXL is known to regulate various intracellular signaling pathways (Allen et al., 2002; Hafizi and Dahlbäck 2006), including Ras/ERK, PI3K, and p38 (Allen et al., 2002); AXL inhibition here may contribute to the downregulation of p38 signaling. Apilimod, a PIKFYVE inhibitor, has been described in a recent study to have antiviral capacity (Ou et al., 2020). Here we expand this into a mechanism of regulation by phosphorylation of PIKFYVE upon SARS-CoV-2 infection.

Similar to successful antiretroviral therapy for HIV, a combinatorial drug cocktail may be a viable treatment option for SARS-CoV-2 infection. Specifically, combining remdesivir with the kinase inhibitors identified in this study as well as with translation inhibitors and/or modulators of sigma-1 receptor (Gordon et al., 2020) warrants further testing. Furthermore, pairing genetic and pharmacological perturbations in a systematic fashion could identify new combination therapy approaches and illuminate disease mechanisms.

The unbiased, global phosphoproteomics approaches used here highlight cellular processes hijacked during SARS-CoV-2 infection. To address the need for improved therapeutic strategies to fight COVID-19, we employed a data-driven approach by mapping phosphorylation profiles of dysregulated signaling pathways to drugs and compounds targeting those signaling pathways. We hope this paradigm can be employed in the future to find additional therapies for COVID-19 and other infectious diseases.

Limitations of Study

A limitation of the current study is the use of a non-human cell line for proteomics analysis upon SARS-CoV-2 infection; here, an African green monkey cell line (Vero E6) was used because it has been shown previously to be highly permissible to SARS-CoV-2 infection (Harcourt et al., 2020). However, pharmacological inhibition of SARS-CoV-2 was assessed in human lung A549-ACE2 cells in addition to Vero E6 cells. The majority of drug effects were found to be replicated between cell lines.

STAR★METHODS

Detailed methods are provided in the online version of this paper and include the following:

- KEY RESOURCES TABLE
- RESOURCE AVAILABILITY
  ○ Lead Contact
  ○ Materials Availability
  ○ Data and Code Availability
- EXPERIMENTAL MODEL AND SUBJECT DETAILS
  ○ Cells
  ○ Viruses (Institut Pasteur, Paris)
  ○ Viruses (Mount Sinai, New York)
  ○ Viruses (University of Freiburg, Germany)
- METHODS DETAILS
  ○ Vero E6 cell infection for proteomic analysis
  ○ Cell lysis and digestion
  ○ Phosphopeptide enrichment
  ○ Mass spectrometry data acquisition
  ○ Spectral library generation and raw data processing
  ○ Immunofluorescence microscopy
  ○ Electron microscopy
  ○ N overexpression in Vero E6 cells
  ○ Cell cycle analysis
  ○ SARS-CoV-2 infections in ACE2-A549 cells and lysis for cytokine analysis
  ○ Cytokine RT-qPCR analysis
  ○ Multiplexed cytokine ELISA
  ○ SARS-CoV-2 viral quantification via antibody staining in presence of inhibitors
  ○ Cytotoxicity cell viability assays
  ○ siRNA-based knockdown of host kinases
  ○ SARS-CoV-2 viral quantification via RT-qPCR in presence of inhibitors
  ○ SARS-CoV-2 titration by plaque assay
  ○ siRNA Cell viability assays
- QUANTIFICATION AND STATISTICAL ANALYSIS
  ○ Mass spectrometry data pre-processing
  ○ Identifying significantly regulated proteins
  ○ Mapping C. sabaeus and *H. sapiens* proteins
  ○ GO enrichment analysis
  ○ Clustering of phosphorylation changes

- ○ Estimation of kinase activities in the time-course experiment
- ○ Comparison of phosphorylation profiles with other conditions
- ○ Phosphorylation of protein complexes
- ○ Transcription factor activity after SARS-CoV-2 infection
- ○ Pharmacological profiling dose response analysis

SUPPLEMENTAL INFORMATION

Supplemental Information can be found online at https://doi.org/10.1016/j.cell.2020.06.034.

SUPPORTING CITATIONS

The following references appear in the Supplemental Information: Abraham et al. (2000); Alfonso et al. (2011); Ali et al. (2000); Amin et al. (2014); Aoh et al. (2009); Araujo et al. (1993); Archambault and Carmena (2012); Aubrey et al. (2016); Auld et al. (2005); Bai et al. (1996); Bakircioglu et al. (2011); Bandau et al. (2012); Barkley et al. (2012); Bartrons et al. (2018); Bassermann et al. (2005); Bayliss et al. (2012); Beeson (2013); Beli et al. (2012); Ben Djoudi Ouadda et al. (2018); Beurel et al. (2015); Biaoxue et al. (2016); Bieling et al. (2008); Bischoff et al. (1990); Bitko et al. (2008); Blethrow et al. (2008); Böck et al. (2010); Boeing et al. (2016); Bradshaw et al. (2013); Brattsand et al. (1994); Bromberg and Darnell (2000); Bruinsma et al. (2014); Byon et al. (1998); Cahill et al. (2016a); Cahill et al. (2016b); Cai et al. (2006); Cai et al. (2007); Casado et al. (2014); Chang et al. (2004); Chen et al. (1999); Chen et al. (2002); Chen et al. (2004); Chen et al. (2009); Chen et al. (2013); Chen et al. (2017); Cheng et al. (1998); Cheng et al. (2000); Chiu et al. (2012); Cho et al. (2019); Chou et al. (1990); Chu et al. (2012); Corkery et al. (2015); Costa-Mattioli et al. (2004); Courcelles et al. (2013); Cox et al. (2003); Das et al. (2018); Das et al. (2019); Day et al. (2010); de Haan and Rottier (2005); Decker and Kovarik (2000); DeDiego et al. (2011); DeDiego et al. (2014); Degryse et al. (2018); Deora et al. (2004); Dephoure et al. (2008); Díaz-Moreno et al. (2009); Dou et al. (2015); Eguchi et al. (2009); Elia et al. (2015); Ellis et al. (2019); Eriksson et al. (2004); Escobar et al. (2015); Eto et al. (2012); Eulalio et al. (2007); Fallahi et al. (2016); Fan et al. (1997); Fan et al. (2018); Fang et al. (2000); Farquar et al. (2008); Feldman et al. (1997); Fleming et al. (2000); Folker et al. (2005); Foltz et al. (2009); Formstecher et al. (2001); Franchin et al. (2015); Frémin et al. (2016); Fujimoto et al. (2017); Gagnon and Delpire (2010); Gao and Luo (2006); Garcia-Moreno et al. (2018); Geuens et al. (2017); Gherzi et al. (2004); Goel et al. (2015); Goldstein et al. (2000); Grzenda et al. (2009); Guo et al. (2017); Hajjar (1991); Hajjar et al. (1994); Halder and Johnson (2011); Handschick et al. (2014); Harder et al. (2014); He et al. (2010); He et al. (2018); Heald and McKeon (1990); Heaton et al. (2016); Hedglin and Benkovic (2015); Hein and Nilsson (2016); Hensley and Kursula (2016); Holz et al. (2005); Hou et al. (2011); Hu et al. (2010); Hu et al. (2013); Hu et al. (2015); Huang and Lai (2001); Huang et al. (2006); Huang et al. (2014); Hwang et al. (2014); Ichimura et al. (2005); Inoki et al. (2002); Inoue et al. (2011); Intine et al. (2003); Ishii et al. (2013); Ishikawa et al. (2015); Izawa and Inagaki (2006); Jacque and Stevenson (2006); Jang et al. (2015); Jiang et al. (2014); Johnson et al. (2011); Kane et al. (2002); Kanzawa et al. (2006); Karin (1995); Kastenhuber and Lowe (2017); Katayama et al. (2004); Kennedy et al. (2017); Khurana and Bhattacharyya (2015); Killoran et al. (2015); Kim et al. (2006); Kindrachuk et al. (2015); Kishimoto et al. (2003); Kjolby et al. (2010); Koff et al. (1992); Kohl et al. (2019); Koseki et al. (1999); Kostenko et al. (2009); Kotula et al. (2013); Kovacina et al. (2003); Kraft et al. (2003); Kramer et al. (1998); Kremer et al. (2007); Kuang et al. (2016); Kumar et al. (2014); Kumar et al. (2018); Kunapuli et al. (2006); Labit et al. (2012); Lamarche-Vane and Hall (1998); Larance et al. (2010); Lau et al. (2006); Law et al. (2007); Le Sage et al. (2016); Lee and Myung (2008); Lee et al. (2011); Lee et al. (2012); Lee et al. (2013); Leite and Way (2015); Lekmine et al. (2003); Lekmine et al. (2004); Leukel and Jost (1995); Levy and Lee (2002); Li and Martinez (2011);

Li and Nagy (2011); Li et al. (2007a); Li et al. (2007b); Li et al. (2008); Li et al. (2016); Li et al. (2017); Liang et al. (2016); Liao et al. (2005); Lieberman et al. (2017); Lim et al. (2013); Lin et al. (2009); Lin et al. (2013); Lingel et al. (2017); Lisnock et al. (2000); Liu and Schneider (2013); Liu et al. (2011); Liu et al. (2013); Liu et al. (2015); Lobry et al. (2007); Lokireddy et al. (2015); Long et al. (2014); Lu et al. (2014); Lu et al. (2017); Lubas et al. (2011); Luciani et al. (2000); Lukas et al. (2011); Luo et al. (2005); Ly et al. (2014); Ly et al. (2017); Machado-Neto et al. (2014); Machowska et al. (2015); Madureira et al. (2012); Magnuson et al. (2012); Magron et al. (2015); Mahony et al. (2017); Mancini et al. (2017); Mandl et al. (2005); Manning and Toker (2017); Marcos-Villar et al. (2016); Marklund et al. (1993); Marklund et al. (1996); Marquette et al. (2011); Matsuhashi et al. (2019); Matsumoto et al. (2015); Matsuoka et al. (2003); McCamphill et al. (2015); McClain et al. (2002); Mehellou et al. (2018); Meier and Blobel (1990); Meier and Blobel (1992); Meier and Blobel 1992; Mendoza et al. (2011); Menon et al. (2014); Mizutani et al. (2004); Mo et al. (2012); Moldave (1985); Morris et al. (2017); Muda et al. (1996); Mueller et al. (2007); Müller et al. (2014); Na et al. (2015); Nairn et al. (2001); Nandi et al. (2007); Needham et al. (2019); Nielsen et al. (2001); Ogiso et al. (2004); Ohtsubo et al. (1995); Old et al. (2009); Olsen et al. (2006); Olsen et al. (2010); Oshiro et al. (2007); Palamarchuk et al. (2005); Pan (2010); Paquette et al. (2018); Park et al. (2000); Parplys et al. (2015); Patel et al. (2015); Penzo et al. (2019); Pfeiffer et al. (2011); Pires et al. (2017); Ponnam et al. (2019); Popov (2012); Poppe et al. (2017); Potter et al. (2002); Potthoff and Olson (2007); Preisinger et al. (2004); Proteau et al. (2005); Qiao et al. (2016); Qiu et al. (2016); Radic (2016); Radtke et al. (2006); Radulescu and Cleveland (2010); Rahim et al. (2018); Rai et al. (2017); Ramm et al. (2006); Raught et al. (2004); Ravichandran et al. (2001); Rebeaud et al. (2008); Renganathan et al. (2005); Revenko et al. (2010); Riad et al. (2018); Robinson et al. (2018); Robinson-White and Stratakis (2002); Robitaille et al. (2013); Rogalla et al. (1999); Rogers et al. (2015); Roy et al. (2014); Roy et al. (2017); Ryan et al. (2016); Salvi et al. (2009); Sanborn et al. (2011); Sánchez-Martín and Komatsu (2018); Santamaria et al. (2003); Saredi et al. (1997); Schmucker and Sumara (2014); Schweppe et al. (2013); Sengupta et al. (2013); Shah et al. (2018); Shahbazian et al. (2006); Shandilya et al. (2014); Sharma et al. (2011); Sharma et al. (2014); Shi and Sun (2015); Shi et al. (2008); Shih et al. (2012); Sinclair et al. (2006); Smith and Enquist (2002); Snyder et al. (2004); Stoilov et al. (2004); Stokoe et al. (1992); Su et al. (2001); Tacke et al. (1998); Tafforeau et al. (2011); Tan et al. (2004); Tan et al. (2012); Tanenbaum et al. (2006); Tantos et al. (2013); Tarakhovsky and Prinjha (2018); Tavares et al. (2015); Tee et al. (2002); Thaker et al. (2019); Thejer et al. (2020); Tiedje et al. (2015); Tokuyama et al. (2001); Toughiri et al. (2013); Trencia et al. (2003); Trigg and Ferguson (2015); Tsai and Seto (2002); Tsai et al. (1993); Tsoi et al. (2014); Tsvetkov and Stern (2005); Ui et al. (2015); Ujike and Taguchi (2015); Valvezan and Klein (2012); Vind et al. (2011); Vishwanatha and Kumble (1993); Wada et al. (2001); Walter et al. (2002); Walter et al. (2016); Wang and Prives (1995); Wang and Zhang (1999); Wang et al. (2000); Wang et al. (2007); Wang et al. (2008); Wang et al. (2013); Wang et al. (2020); Ward et al. (2004); Wen et al. (1995); Wertz et al. (2015); Willems et al. (1996); Williams et al. (1997); Wohlbold et al. (2012); Wolin and Cedervall (2002); Wortzel and Seger (2011); Wu et al. (2014); Wu et al. (2018); Wurm et al. (2001); Xu et al. (2011); Yang et al. (2012a); Yang et al. (2012b); Yang et al (2014); Yao et al. (2017); Ye et al. (2008); Yim et al. (2013); Yoo et al. (2019); Yu et al. (2009); Yu et al. (2011); Yu et al. (2012); Yui et al. (2001); Zhang et al. (1998); Zhang et al. (2009); Zhang et al. (2015); Zhang et al. (2019a); Zhang et al. (2019b); Zhao et al. (2015); Zhou et al. (2016); Zhu et al. (2001); Zhu et al. (2017); Zou et al. (2007); Zuo and Manley (1993).

REFERENCES

Abraham, J., Kelly, J., Thibault, P., and Benchimol, S. (2000). Post-translational modification of p53 protein in response to ionizing radiation analyzed by mass spectrometry. J. Mol. Biol. 295, 853–864.

Alfonso, R., Lutz, T., Rodriguez, A., Chavez, J.P., Rodriguez, P., Gutierrez, S., and Nieto, A. (2011). CHD6 chromatin remodeler is a negative modulator of influenza virus replication that relocates to inactive chromatin upon infection. Cell. Microbiol. 13, 1894–1906.

Ali, N., Pruijn, G.J., Kenan, D.J., Keene, J.D., and Siddiqui, A. (2000). Human La antigen is required for the hepatitis C virus internal ribosome entry site-mediated translation. J. Biol. Chem. 275, 27531–27540.

Allen, M.P., Linseman, D.A., Udo, H., Xu, M., Schaack, J.B., Varnum, B., Kandel, E.R., Heidenreich, K.A., and Wierman, M.E. (2002). Novel mechanism for gonadotropin-releasing hormone neuronal migration involving Gas6/Ark signaling to p38 mitogen-activated protein kinase. Mol. Cell. Biol. 22, 599–613.

Alvarez, D.E., and Agaisse, H. (2012). Casein kinase 2 regulates vaccinia virus actin tail formation. Virology 423, 143–151.

Alvarez, M.J., Shen, Y., Giorgi, F.M., Lachmann, A., Ding, B.B., Ye, B.H., and Califano, A. (2016). Functional characterization of somatic mutations in cancer using network-based inference of protein activity. Nat. Genet. 48, 838–847.

Amin, M.A., Itoh, G., Iemura, K., Ikeda, M., and Tanaka, K. (2014). CLIP-170 recruits PLK1 to kinetochores during early mitosis for chromosome alignment. J. Cell Sci. 127, 2818–2824.

Aoh, Q.L., Castle, A.M., Hubbard, C.H., Katsumata, O., and Castle, J.D. (2009). SCAMP3 negatively regulates epidermal growth factor receptor degradation and promotes receptor recycling. Mol. Biol. Cell 20, 1816–1832.

Araujo, H., Danziger, N., Cordier, J., Glowinski, J., and Chneiweiss, H. (1993). Characterization of PEA-15, a major substrate for protein kinase C in astrocytes. J. Biol. Chem. 268, 5911–5920.

Archambault, V., and Carmena, M. (2012). Polo-like kinase-activating kinases: Aurora A, Aurora B and what else? Cell Cycle 11, 1490–1495.

Ariumi, Y., Kuroki, M., Dansako, H., Abe, K., Ikeda, M., Wakita, T., and Kato, N. (2008). The DNA damage sensors ataxia-telangiectasia mutated kinase and checkpoint kinase 2 are required for hepatitis C virus RNA replication. J. Virol. 82, 9639–9646.

Aubrey, B.J., Strasser, A., and Kelly, G.L. (2016). Tumor-Suppressor Functions of the TP53 Pathway. Cold Spring Harb. Perspect. Med. 6, a026062.

Auld, G.C., Campbell, D.G., Morrice, N., and Cohen, P. (2005). Identification of calcium-regulated heat-stable protein of 24 kDa (CRHSP24) as a physiological substrate for PKB and RSK using KESTREL. Biochem. J. 389, 775–783.

Bachman, J.A., Gyori, B.M., and Sorger, P.K. (2019). Assembling a phosphoproteomic knowledge base using ProtMapper to normalize phosphosite information from databases and text mining. bioRxiv. https://doi.org/10.1101/822668.

Bai, C., Sen, P., Hofmann, K., Ma, L., Goebl, M., Harper, J.W., and Elledge, S.J. (1996). SKP1 connects cell cycle regulators to the ubiquitin proteolysis machinery through a novel motif, the F-box. Cell 86, 263–274.

Bai, Y., Yao, L., Wei, T., Tian, F., Jin, D.-Y., Chen, L., and Wang, M. (2020). Presumed Asymptomatic Carrier Transmission of COVID-19. JAMA 323, 1406–1407.

Bakircioglu, M., Carvalho, O.P., Khurshid, M., Cox, J.J., Tuysuz, B., Barak, T., Yilmaz, S., Caglayan, O., Dincer, A., Nicholas, A.K., et al. (2011). The essential role of centrosomal NDE1 in human cerebral cortex neurogenesis. Am. J. Hum. Genet. 88, 523–535.

Bandau, S., Knebel, A., Gage, Z.O., Wood, N.T., and Alexandru, G. (2012). UBXN7 docks on neddylated cullin complexes using its UIM motif and causes HIF1α accumulation. BMC Biol. 10, 36.

Barkley, L.R., Palle, K., Durando, M., Day, T.A., Gurkar, A., Kakusho, N., Li, J., Masai, H., and Vaziri, C. (2012). c-Jun N-terminal kinase-mediated Rad18 phosphorylation facilitates Polη recruitment to stalled replication forks. Mol. Biol. Cell 23, 1943–1954.

Bartrons, R., Simon-Molas, H., Rodríguez-García, A., Castaño, E., Navarro-Sabaté, À., Manzano, A., and Martinez-Outschoorn, U.E. (2018). Fructose 2,6-Bisphosphate in Cancer Cell Metabolism. Front. Oncol. 8, 331.

Bassermann, F., von Klitzing, C., Münch, S., Bai, R.-Y., Kawaguchi, H., Morris, S.W., Peschel, C., and Duyster, J. (2005). NIPA defines an SCF-type mammalian E3 ligase that regulates mitotic entry. Cell 122, 45–57.

Bayliss, R., Fry, A., Haq, T., and Yeoh, S. (2012). On the molecular mechanisms of mitotic kinase activation. Open Biol. 2, 120136.

Beeson, D. (2013). Hereditary and Autoimmune Myasthenias. In Emery and Rimoin's Principles and Practice of Medical Genetics, D. Rimoin, R. Pyeritz, and B. Korf, eds. (Elsevier), pp. 1–17.

Beli, P., Lukashchuk, N., Wagner, S.A., Weinert, B.T., Olsen, J.V., Baskcomb, L., Mann, M., Jackson, S.P., and Choudhary, C. (2012). Proteomic investigations reveal a role for RNA processing factor THRAP3 in the DNA damage response. Mol. Cell 46, 212–225.

Ben Djoudi Ouadda, A., He, Y., Calabrese, V., Ishii, H., Chidiac, R., Gratton, J.-P., Roux, P.P., and Lamarche-Vane, N. (2018). CdGAP/ARHGAP31 is regulated by RSK phosphorylation and binding to 14-3-3β adaptor protein. Oncotarget 9, 11646–11664.

Beurel, E., Grieco, S.F., and Jope, R.S. (2015). Glycogen synthase kinase-3 (GSK3): regulation, actions, and diseases. Pharmacol. Ther. 148, 114–131.

Biaoxue, R., Hua, L., Wenlong, G., and Shuanying, Y. (2016). Overexpression of stathmin promotes metastasis and growth of malignant solid tumors: a systemic review and meta-analysis. Oncotarget 7, 78994–79007.

Bieling, P., Kandels-Lewis, S., Telley, I.A., van Dijk, J., Janke, C., and Surrey, T. (2008). CLIP-170 tracks growing microtubule ends by dynamically recognizing composite EB1/tubulin-binding sites. J. Cell Biol. 183, 1223–1233.

Bischoff, J.R., Friedman, P.N., Marshak, D.R., Prives, C., and Beach, D. (1990). Human p53 is phosphorylated by p60-cdc2 and cyclin B-cdc2. Proc. Natl. Acad. Sci. USA 87, 4766–4770.

Bitko, V., Musiyenko, A., Bayfield, M.A., Maraia, R.J., and Barik, S. (2008). Cellular La protein shields nonsegmented negative-strand RNA viral leader RNA from RIG-I and enhances virus growth by diverse mechanisms. J. Virol. 82, 7977–7987.

Blanco-Melo, D., Nilsson-Payant, B.E., Liu, W.-C., Uhl, S., Hoagland, D., Møller, R., Jordan, T.X., Oishi, K., Panis, M., Sachs, D., et al. (2020). Imbalanced Host Response to SARS-CoV-2 Drives Development of COVID-19. Cell 181, 1036–1045.e9.

Blethrow, J.D., Glavy, J.S., Morgan, D.O., and Shokat, K.M. (2008). Covalent capture of kinase-specific phosphopeptides reveals Cdk1-cyclin B substrates. Proc. Natl. Acad. Sci. USA 105, 1442–1447.

Böck, B.C., Tagscherer, K.E., Fassl, A., Krämer, A., Oehme, I., Zentgraf, H.-W., Keith, M., and Roth, W. (2010). The PEA-15 protein regulates autophagy via activation of JNK. J. Biol. Chem. 285, 21644–21654.

Boeing, S., Williamson, L., Encheva, V., Gori, I., Saunders, R.E., Instrell, R., Aygün, O., Rodriguez-Martinez, M., Weems, J.C., Kelly, G.P., et al. (2016). Multiomic Analysis of the UV-Induced DNA Damage Response. Cell Rep. 15, 1597–1610.

Bradshaw, N.J., Hennah, W., and Soares, D.C. (2013). NDE1 and NDEL1: twin neurodevelopmental proteins with similar 'nature' but different 'nurture'. Biomol. Concepts 4, 447–464.

Brattsand, G., Marklund, U., Nylander, K., Roos, G., and Gullberg, M. (1994). Cell-cycle-regulated phosphorylation of oncoprotein 18 on Ser16, Ser25 and Ser38. Eur. J. Biochem. 220, 359–368.

Bromberg, J., and Darnell, J.E., Jr. (2000). The role of STATs in transcriptional control and their impact on cellular function. Oncogene 19, 2468–2473.

Bruderer, R., Bernhardt, O.M., Gandhi, T., Miladinović, S.M., Cheng, L.-Y., Messner, S., Ehrenberger, T., Zanotelli, V., Butscheid, Y., Escher, C., et al. (2015). Extending the limits of quantitative proteome profiling with data-independent acquisition and application to acetaminophen-treated three-dimensional liver microtissues. Mol. Cell. Proteomics 14, 1400–1410.

Bruinsma, W., Macurek, L., Freire, R., Lindqvist, A., and Medema, R.H. (2014). Bora and Aurora-A continue to activate Plk1 in mitosis. J. Cell Sci. 127, 801–811.

Byon, J.C., Kusari, A.B., and Kusari, J. (1998). Protein-tyrosine phosphatase-1B acts as a negative regulator of insulin signal transduction. Mol. Cell. Biochem. 182, 101–108.

Cahill, M.A., Jazayeri, J.A., Kovacevic, Z., and Richardson, D.R. (2016a). PGRMC1 regulation by phosphorylation: potential new insights in controlling biological activity. Oncotarget 7, 50822–50827.

Cahill, M.A., Jazayeri, J.A., Catalano, S.M., Toyokuni, S., Kovacevic, Z., and Richardson, D.R. (2016b). The emerging role of progesterone receptor membrane component 1 (PGRMC1) in cancer biology. Biochim. Biophys. Acta 1866, 339–349.

Cai, S.-L., Tee, A.R., Short, J.D., Bergeron, J.M., Kim, J., Shen, J., Guo, R., Johnson, C.L., Kiguchi, K., and Walker, C.L. (2006). Activity of TSC2 is inhibited by AKT-mediated phosphorylation and membrane partitioning. J. Cell Biol. 173, 279–289.

Cai, Y., Liu, Y., and Zhang, X. (2007). Suppression of coronavirus replication by inhibition of the MEK signaling pathway. J. Virol. 81, 446–456.

Casado, P., Rodriguez-Prados, J.-C., Cosulich, S.C., Guichard, S., Vanhaesebroeck, B., Joel, S., and Cutillas, P.R. (2013). Kinase-substrate enrichment analysis provides insights into the heterogeneity of signaling pathway activation in leukemia cells. Sci. Signal. 6, rs6.

Casado, P., Bilanges, B., Rajeeve, V., Vanhaesebroeck, B., and Cutillas, P.R. (2014). Environmental stress affects the activity of metabolic and growth factor signaling networks and induces autophagy markers in MCF7 breast cancer cells. Mol. Cell. Proteomics 13, 836–848.

Chang, Y.-J., Liu, C.Y., Chiang, B.L., Chao, Y.C., and Chen, C.C. (2004). Induction of IL-8 release in lung cells via activator protein-1 by recombinant baculovirus displaying severe acute respiratory syndrome-coronavirus spike proteins: identification of two functional regions. J. Immunol. 173, 7602–7614.

Chaurushiya, M.S., and Weitzman, M.D. (2009). Viral manipulation of DNA repair and cell cycle checkpoints. DNA Repair (Amst.) 8, 1166–1176.

Chen, H.K., Pai, C.Y., Huang, J.Y., and Yeh, N.H. (1999). Human Nopp140, which interacts with RNA polymerase I: implications for rRNA gene transcription and nucleolar structural organization. Mol. Cell. Biol. 19, 8536–8546.

Chen, H., Wurm, T., Britton, P., Brooks, G., and Hiscox, J.A. (2002). Interaction of the coronavirus nucleoprotein with nucleolar antigens and the host cell. J. Virol. 76, 5233–5250.

Chen, W., Yazicioglu, M., and Cobb, M.H. (2004). Characterization of OSR1, a member of the mammalian Ste20p/germinal center kinase subfamily. J. Biol. Chem. 279, 11129–11136.

Chen, C.-B., Ng, J.K.W., Choo, P.-H., Wu, W., and Porter, A.G. (2009). Mammalian sterile 20-like kinase 3 (MST3) mediates oxidative-stress-induced cell death by modulating JNK activation. Biosci. Rep. 29, 405–415.

Chen, J.-T., Ho, C.-W., Chi, L.-M., Chien, K.-Y., Hsieh, Y.-J., Lin, S.-J., and Yu, J.-S. (2013). Identification of the lamin A/C phosphoepitope recognized by the antibody P-STM in mitotic HeLa S3 cells. BMC Biochem. 14, 18.

Chen, J.-Y., Lin, C.-H., and Chen, B.-C. (2017). Hypoxia-induced ADAM 17 expression is mediated by RSK1-dependent C/EBPβ activation in human lung fibroblasts. Mol. Immunol. 88, 155–163.

Cheng, X., Ma, Y., Moore, M., Hemmings, B.A., and Taylor, S.S. (1998). Phosphorylation and activation of cAMP-dependent protein kinase by phosphoinositide-dependent protein kinase. Proc. Natl. Acad. Sci. USA 95, 9849–9854.

Cheng, J., Yang, J., Xia, Y., Karin, M., and Su, B. (2000). Synergistic interaction of MEK kinase 2, c-Jun N-terminal kinase (JNK) kinase 2, and JNK1 results in efficient and specific JNK1 activation. Mol. Cell. Biol. 20, 2334–2342.

Chiu, M., Tardito, S., Barilli, A., Bianchi, M.G., Dall'Asta, V., and Bussolati, O. (2012). Glutamine stimulates mTORC1 independent of the cell content of essential amino acids. Amino Acids 43, 2561–2567.

Cho, H., Lee, W., Kim, G.-W., Lee, S.-H., Moon, J.-S., Kim, M., Kim, H.S., and Oh, J.-W. (2019). Regulation of La/SSB-dependent viral gene expression by pre-tRNA 3′ trailer-derived tRNA fragments. Nucleic Acids Res. 47, 9888–9901.

Choi, M., Chang, C.-Y., Clough, T., Broudy, D., Killeen, T., MacLean, B., and Vitek, O. (2014). MSstats: an R package for statistical analysis of quantitative mass spectrometry-based proteomic experiments. Bioinformatics 30, 2524–2526.

Chou, Y.H., Bischoff, J.R., Beach, D., and Goldman, R.D. (1990). Intermediate filament reorganization during mitosis is mediated by p34cdc2 phosphorylation of vimentin. Cell 62, 1063–1071.

Chu, J., Loughlin, E.A., Gaur, N.A., SenBanerjee, S., Jacob, V., Monson, C., Kent, B., Oranu, A., Ding, Y., Ukomadu, C., and Sadler, K.C. (2012). UHRF1 phosphorylation by cyclin A2/cyclin-dependent kinase 2 is required for zebrafish embryogenesis. Mol. Biol. Cell 23, 59–70.

Chu, D.K.W., Pan, Y., Cheng, S.M.S., Hui, K.P.Y., Krishnan, P., Liu, Y., Ng, D.Y.M., Wan, C.K.C., Yang, P., Wang, Q., et al. (2020). Molecular Diagnosis of a Novel Coronavirus (2019-nCoV) Causing an Outbreak of Pneumonia. Clin. Chem. 66, 549–555.

Corkery, D.P., Holly, A.C., Lahsaee, S., and Dellaire, G. (2015). Connecting the speckles: Splicing kinases and their role in tumorigenesis and treatment response. Nucleus 6, 279–288.

Costa-Mattioli, M., Svitkin, Y., and Sonenberg, N. (2004). La autoantigen is necessary for optimal function of the poliovirus and hepatitis C virus internal ribosome entry site in vivo and in vitro. Mol. Cell. Biol. 24, 6861–6870.

Courcelles, M., Frémin, C., Voisin, L., Lemieux, S., Meloche, S., and Thibault, P. (2013). Phosphoproteome dynamics reveal novel ERK1/2 MAP kinase substrates with broad spectrum of functions. Mol. Syst. Biol. 9, 669.

Cox, D.M., Du, M., Marback, M., Yang, E.C.C., Chan, J., Siu, K.W.M., and McDermott, J.C. (2003). Phosphorylation motifs regulating the stability and function of myocyte enhancer factor 2A. J. Biol. Chem. 278, 15297–15303.

Cuadrado, A., and Nebreda, A.R. (2010). Mechanisms and functions of p38 MAPK signalling. Biochem. J. 429, 403–417.

D'Amore, C., Salizzato, V., Borgo, C., Cesaro, L., Pinna, L.A., and Salvi, M. (2019). A Journey through the Cytoskeleton with Protein Kinase CK2. Curr. Protein Pept. Sci. 20, 547–562.

Das, T., Chen, Z., Hendriks, R.W., and Kool, M. (2018). A20/Tumor Necrosis Factor α-Induced Protein 3 in Immune Cells Controls Development of Autoinflammation and Autoimmunity: Lessons from Mouse Models. Front. Immunol. 9, 104.

Das, T., Kim, E.E., and Song, E.J. (2019). Phosphorylation of USP15 and USP4 Regulates Localization and Spliceosomal Deubiquitination. J. Mol. Biol. 431, 3900–3912.

Davidson, A.D., Williamson, M.K., Lewis, S., Shoemark, D., Carroll, M.W., Heesom, K., Zambon, M., Ellis, J., Lewis, P.A., Hiscox, J.A., et al. (2020). Characterisation of the transcriptome and proteome of SARS-CoV-2 using direct RNA sequencing and tandem mass spectrometry reveals evidence for a cell passage induced in-frame deletion in the spike glycoprotein that removes the furin-like cleavage site. bioRxiv. https://doi.org/10.1101/2020.03.22.002204.

Day, T.A., Palle, K., Barkley, L.R., Kakusho, N., Zou, Y., Tateishi, S., Verreault, A., Masai, H., and Vaziri, C. (2010). Phosphorylated Rad18 directs DNA polymerase η to sites of stalled replication. J. Cell Biol. 191, 953–966.

de Haan, C.A.M., and Rottier, P.J.M. (2005). Molecular interactions in the assembly of coronaviruses. Adv. Virus Res. 64, 165–230.

Decker, T., and Kovarik, P. (2000). Serine phosphorylation of STATs. Oncogene 19, 2628–2637.

DeDiego, M.L., Nieto-Torres, J.L., Jiménez-Guardeño, J.M., Regla-Nava, J.A., Álvarez, E., Oliveros, J.C., Zhao, J., Fett, C., Perlman, S., and Enjuanes, L. (2011). Severe acute respiratory syndrome coronavirus envelope protein regulates cell stress response and apoptosis. PLoS Pathog. 7, e1002315.

DeDiego, M.L., Nieto-Torres, J.L., Regla-Nava, J.A., Jimenez-Guardeño, J.M., Fernandez-Delgado, R., Fett, C., Castaño-Rodriguez, C., Perlman, S., and Enjuanes, L. (2014). Inhibition of NF-κB-mediated inflammation in severe acute respiratory syndrome coronavirus-infected mice increases survival. J. Virol. 88, 913–924.

Degryse, S., de Bock, C.E., Demeyer, S., Govaerts, I., Bornschein, S., Verbeke, D., Jacobs, K., Binos, S., Skerrett-Byrne, D.A., Murray, H.C., et al. (2018). Mutant JAK3 phosphoproteomic profiling predicts synergism between JAK3 inhibitors and MEK/BCL2 inhibitors for the treatment of T-cell acute lymphoblastic leukemia. Leukemia 32, 788–800.

Deora, A.B., Kreitzer, G., Jacovina, A.T., and Hajjar, K.A. (2004). An annexin 2 phosphorylation switch mediates p11-dependent translocation of annexin 2 to the cell surface. J. Biol. Chem. 279, 43411–43418.

Dephoure, N., Zhou, C., Villén, J., Beausoleil, S.A., Bakalarski, C.E., Elledge, S.J., and Gygi, S.P. (2008). A quantitative atlas of mitotic phosphorylation. Proc. Natl. Acad. Sci. USA 105, 10762–10767.

Díaz-Moreno, I., Hollingworth, D., Frenkiel, T.A., Kelly, G., Martin, S., Howell, S., García-Mayoral, M., Gherzi, R., Briata, P., and Ramos, A. (2009). Phosphorylation-mediated unfolding of a KH domain regulates KSRP localization via 14-3-3 binding. Nat. Struct. Mol. Biol. 16, 238–246.

Dou, X., Wei, J., Sun, A., Shao, G., Childress, C., Yang, W., and Lin, Q. (2015). PBK/TOPK mediates geranylgeranylation signaling for breast cancer cell proliferation. Cancer Cell Int. 15, 27.

Dove, B., Brooks, G., Bicknell, K., Wurm, T., and Hiscox, J.A. (2006). Cell cycle perturbations induced by infection with the coronavirus infectious bronchitis virus and their effect on virus replication. J. Virol. 80, 4147–4156.

Eguchi, S., Oshiro, N., Miyamoto, T., Yoshino, K., Okamoto, S., Ono, T., Kikkawa, U., and Yonezawa, K. (2009). AMP-activated protein kinase phosphorylates glutamine : fructose-6-phosphate amidotransferase 1 at Ser243 to modulate its enzymatic activity. Genes Cells 14, 179–189.

Elia, A.E.H., Boardman, A.P., Wang, D.C., Huttlin, E.L., Everley, R.A., Dephoure, N., Zhou, C., Koren, I., Gygi, S.P., and Elledge, S.J. (2015). Quantitative Proteomic Atlas of Ubiquitination and Acetylation in the DNA Damage Response. Mol. Cell 59, 867–881.

Elias, J.E., and Gygi, S.P. (2007). Target-decoy search strategy for increased confidence in large-scale protein identifications by mass spectrometry. Nat. Methods 4, 207–214.

Ellis, R., Katerelos, M., Choy, S.W., Cook, N., Lee, M., Paizis, K., Pell, G., Walker, S., Power, D.A., and Mount, P.F. (2019). Increased expression and phosphorylation of 6-phosphofructo-2-kinase/fructose-2,6-bisphosphatase isoforms in urinary exosomes in pre-eclampsia. J. Transl. Med. 17, 60.

Eriksson, J.E., He, T., Trejo-Skalli, A.V., Härmälä-Braskén, A.-S., Hellman, J., Chou, Y.-H., and Goldman, R.D. (2004). Specific in vivo phosphorylation sites determine the assembly dynamics of vimentin intermediate filaments. J. Cell Sci. 117, 919–932.

Escobar, D.J., Desai, R., Ishiyama, N., Folmsbee, S.S., Novak, M.N., Flozak, A.S., Daugherty, R.L., Mo, R., Nanavati, D., Sarpal, R., et al. (2015). α-Catenin phosphorylation promotes intercellular adhesion through a dual-kinase mechanism. J. Cell Sci. 128, 1150–1165.

Eto, K., Goto, S., Nakashima, W., Ura, Y., and Abe, S.-I. (2012). Loss of programmed cell death 4 induces apoptosis by promoting the translation of procaspase-3 mRNA. Cell Death Differ. 19, 573–581.

Eulalio, A., Behm-Ansmant, I., and Izaurralde, E. (2007). P bodies: at the crossroads of post-transcriptional pathways. Nat. Rev. Mol. Cell Biol. 8, 9–22.

Fallahi, E., O'Driscoll, N.A., and Matallanas, D. (2016). The MST/Hippo Pathway and Cell Death: A Non-Canonical Affair. Genes (Basel) 7, 28.

Fan, H., Sakulich, A.L., Goodier, J.L., Zhang, X., Qin, J., and Maraia, R.J. (1997). Phosphorylation of the human La antigen on serine 366 can regulate recycling of RNA polymerase III transcription complexes. Cell 88, 707–715.

Fan, Y., Sanyal, S., and Bruzzone, R. (2018). Breaking Bad: How Viruses Subvert the Cell Cycle. Front. Cell. Infect. Microbiol. 8, 396.

Fang, X., Yu, S.X., Lu, Y., Bast, R.C., Jr., Woodgett, J.R., and Mills, G.B. (2000). Phosphorylation and inactivation of glycogen synthase kinase 3 by protein kinase A. Proc. Natl. Acad. Sci. USA 97, 11960–11965.

Farquhar, M.J., Harris, H.J., Diskar, M., Jones, S., Mee, C.J., Nielsen, S.U., Brimacombe, C.L., Molina, S., Toms, G.L., Maurel, P., et al. (2008). Protein kinase A-dependent step(s) in hepatitis C virus entry and infectivity. J. Virol. 82, 8797–8811.

Fehr, A.R., and Perlman, S. (2015). Coronaviruses: an overview of their replication and pathogenesis. Methods Mol. Biol. 1282, 1–23.

Feldman, R.M., Correll, C.C., Kaplan, K.B., and Deshaies, R.J. (1997). A complex of Cdc4p, Skp1p, and Cdc53p/cullin catalyzes ubiquitination of the phosphorylated CDK inhibitor Sic1p. Cell 91, 221–230.

Fernández-Golbano, I.M., Idrissi, F.-Z., Giblin, J.P., Grosshans, B.L., Robles, V., Grötsch, H., Borrás, Mdel.M., and Geli, M.I. (2014). Crosstalk between

PI(4,5)P$_2$and CK2 modulates actin polymerization during endocytic uptake. Dev. Cell *30*, 746–758.

Fleming, Y., Armstrong, C.G., Morrice, N., Paterson, A., Goedert, M., and Cohen, P. (2000). Synergistic activation of stress-activated protein kinase 1/c-Jun N-terminal kinase (SAPK1/JNK) isoforms by mitogen-activated protein kinase kinase 4 (MKK4) and MKK7. Biochem. J. *352*, 145–154.

Folker, E.S., Baker, B.M., and Goodson, H.V. (2005). Interactions between CLIP-170, tubulin, and microtubules: implications for the mechanism of Clip-170 plus-end tracking behavior. Mol. Biol. Cell *16*, 5373–5384.

Foltz, D.R., Jansen, L.E.T., Bailey, A.O., Yates, J.R., 3rd, Bassett, E.A., Wood, S., Black, B.E., and Cleveland, D.W. (2009). Centromere-specific assembly of CENP-a nucleosomes is mediated by HJURP. Cell *137*, 472–484.

Formstecher, E., Ramos, J.W., Fauquet, M., Calderwood, D.A., Hsieh, J.C., Canton, B., Nguyen, X.T., Barnier, J.V., Camonis, J., Ginsberg, M.H., and Chneiweiss, H. (2001). PEA-15 mediates cytoplasmic sequestration of ERK MAP kinase. Dev. Cell *1*, 239–250.

Franchin, C., Cesaro, L., Salvi, M., Millioni, R., Iori, E., Cifani, P., James, P., Arrigoni, G., and Pinna, L. (2015). Quantitative analysis of a phosphoproteome readily altered by the protein kinase CK2 inhibitor quinalizarin in HEK-293T cells. Biochim. Biophys. Acta *1854*, 609–623.

Frémin, C., Guégan, J.-P., Plutoni, C., Mahaffey, J., Philips, M.R., Emery, G., and Meloche, S. (2016). ERK1/2-induced phosphorylation of R-Ras GTPases stimulates their oncogenic potential. Oncogene *35*, 5692–5698.

Fu, Y., Yip, A., Seah, P.G., Blasco, F., Shi, P.-Y., and Hervé, M. (2014). Modulation of inflammation and pathology during dengue virus infection by p38 MAPK inhibitor SB203580. Antiviral Res. *110*, 151–157.

Fujimoto, M., Takii, R., Takaki, E., Katiyar, A., Nakato, R., Shirahige, K., and Nakai, A. (2017). The HSF1-PARP13-PARP1 complex facilitates DNA repair and promotes mammary tumorigenesis. Nat. Commun. *8*, 1638.

Gagnon, K.B., and Delpire, E. (2010). On the substrate recognition and negative regulation of SPAK, a kinase modulating Na+-K+-2Cl- cotransport activity. Am. J. Physiol. Cell Physiol. *299*, C614–C620.

Gao, G., and Luo, H. (2006). The ubiquitin-proteasome pathway in viral infections. Can. J. Physiol. Pharmacol. *84*, 5–14.

Garcia-Alonso, L., Holland, C.H., Ibrahim, M.M., Turei, D., and Saez-Rodriguez, J. (2019). Benchmark and integration of resources for the estimation of human transcription factor activities. Genome Res. *29*, 1363–1375.

Garcia-Moreno, M., Järvelin, A.I., and Castello, A. (2018). Unconventional RNA-binding proteins step into the virus-host battlefront. Wiley Interdiscip. Rev. RNA *9*, e1498.

Geuens, T., De Winter, V., Rajan, N., Achsel, T., Mateiu, L., Almeida-Souza, L., Asselbergh, B., Bouhy, D., Auer-Grumbach, M., Bagni, C., and Timmerman, V. (2017). Mutant HSPB1 causes loss of translational repression by binding to PCBP1, an RNA binding protein with a possible role in neurodegenerative disease. Acta Neuropathol. Commun. *5*, 5.

Gherzi, R., Lee, K.-Y., Briata, P., Wegmüller, D., Moroni, C., Karin, M., and Chen, C.-Y. (2004). A KH domain RNA binding protein, KSRP, promotes ARE-directed mRNA turnover by recruiting the degradation machinery. Mol. Cell *14*, 571–583.

Giurgiu, M., Reinhard, J., Brauner, B., Dunger-Kaltenbach, I., Fobo, G., Frishman, G., Montrone, C., and Ruepp, A. (2019). CORUM: the comprehensive resource of mammalian protein complexes-2019. Nucleic Acids Res. *47* (D1), D559–D563.

Goel, P., Manning, J.A., and Kumar, S. (2015). NEDD4-2 (NEDD4L): the ubiquitin ligase for multiple membrane proteins. Gene *557*, 1–10.

Goldstein, B.J., Bittner-Kowalczyk, A., White, M.F., and Harbeck, M. (2000). Tyrosine dephosphorylation and deactivation of insulin receptor substrate-1 by protein-tyrosine phosphatase 1B. Possible facilitation by the formation of a ternary complex with the Grb2 adaptor protein. J. Biol. Chem. *275*, 4283–4289.

Gordon, D.E., Jang, G.M., Bouhaddou, M., Xu, J., Obernier, K., White, K.M., O'Meara, M.J., Rezelj, V.V., Guo, J.Z., Swaney, D.L., et al. (2020). A SARS-CoV-2 protein interaction map reveals targets for drug repurposing. Nature. Published online April 30, 2020. https://doi.org/10.1038/s41586-020-2286-9.

Grein, J., Ohmagari, N., Shin, D., Diaz, G., Asperges, E., Castagna, A., Feldt, T., Green, G., Green, M.L., Lescure, F.-X., et al. (2020). Compassionate Use of Remdesivir for Patients with Severe Covid-19. N. Engl. J. Med. *382*, 2327–2336.

Growcott, E.J., Bamba, D., Galarneau, J.-R., Leonard, V.H.J., Schul, W., Stein, D., and Osborne, C.S. (2018). The effect of P38 MAP kinase inhibition in a mouse model of influenza. J. Med. Microbiol. *67*, 452–462.

Grzenda, A., Lomberk, G., Zhang, J.-S., and Urrutia, R. (2009). Sin3: master scaffold and transcriptional corepressor. Biochim. Biophys. Acta *1789*, 443–450.

Guan, W.-J., Ni, Z.-Y., Hu, Y., Liang, W.-H., Ou, C.-Q., He, J.-X., Liu, L., Shan, H., Lei, C.-L., Hui, D.S.C., et al.; China Medical Treatment Expert Group for Covid-19 (2020). Clinical Characteristics of Coronavirus Disease 2019 in China. N. Engl. J. Med. *382*, 1708–1720.

Guo, X., Huang, X., and Chen, M.J. (2017). Reversible phosphorylation of the 26S proteasome. Protein Cell *8*, 255–272.

Hafizi, S., and Dahlbäck, B. (2006). Signalling and functional diversity within the Axl subfamily of receptor tyrosine kinases. Cytokine Growth Factor Rev. *17*, 295–304.

Hajjar, K.A. (1991). The endothelial cell tissue plasminogen activator receptor. Specific interaction with plasminogen. J. Biol. Chem. *266*, 21962–21970.

Hajjar, K.A., Jacovina, A.T., and Chacko, J. (1994). An endothelial cell receptor for plasminogen/tissue plasminogen activator. I. Identity with annexin II. J. Biol. Chem. *269*, 21191–21197.

Halder, G., and Johnson, R.L. (2011). Hippo signaling: growth control and beyond. Development *138*, 9–22.

Han, H., Yang, L., Liu, R., Liu, F., Wu, K.-L., Li, J., Liu, X.-H., and Zhu, C.-L. (2020). Prominent changes in blood coagulation of patients with SARS-CoV-2 infection. Clin. Chem. Lab. Med. *58*, 1116–1120.

Handschick, K., Beuerlein, K., Jurida, L., Bartkuhn, M., Müller, H., Soelch, J., Weber, A., Dittrich-Breiholz, O., Schneider, H., Scharfe, M., et al. (2014). Cyclin-dependent kinase 6 is a chromatin-bound cofactor for NF-κB-dependent gene expression. Mol. Cell *53*, 193–208.

Harcourt, J., Tamin, A., Lu, X., Kamili, S., Sakthivel, S.K., Murray, J., Queen, K., Tao, Y., Paden, C.R., Zhang, J., et al. (2020). Severe Acute Respiratory Syndrome Coronavirus 2 From Patient With Coronavirus Disease, United States. Emerg. Infect. Dis. *26*, 1266–1273.

Harder, L.M., Bunkenborg, J., and Andersen, J.S. (2014). Inducing autophagy: a comparative phosphoproteomic study of the cellular response to ammonia and rapamycin. Autophagy *10*, 339–355.

He, N., Liu, M., Hsu, J., Xue, Y., Chou, S., Burlingame, A., Krogan, N.J., Alber, T., and Zhou, Q. (2010). HIV-1 Tat and host AFF4 recruit two transcription elongation factors into a bifunctional complex for coordinated activation of HIV-1 transcription. Mol. Cell *38*, 428–438.

He, L., Gomes, A.P., Wang, X., Yoon, S.O., Lee, G., Nagiec, M.J., Cho, S., Chavez, A., Islam, T., Yu, Y., et al. (2018). mTORC1 Promotes Metabolic Reprogramming by the Suppression of GSK3-Dependent Foxk1 Phosphorylation. Mol. Cell *70*, 949–960.e4.

Heald, R., and McKeon, F. (1990). Mutations of phosphorylation sites in lamin A that prevent nuclear lamina disassembly in mitosis. Cell *61*, 579–589.

Heaton, N.S., Moshkina, N., Fenouil, R., Gardner, T.J., Aguirre, S., Shah, P.S., Zhao, N., Manganaro, L., Hultquist, J.F., Noel, J., et al. (2016). Targeting Viral Proteostasis Limits Influenza Virus, HIV, and Dengue Virus Infection. Immunity *44*, 46–58.

Hedglin, M., and Benkovic, S.J. (2015). Regulation of Rad6/Rad18 Activity During DNA Damage Tolerance. Annu. Rev. Biophys. *44*, 207–228.

Hein, J.B., and Nilsson, J. (2016). Interphase APC/C-Cdc20 inhibition by cyclin A2-Cdk2 ensures efficient mitotic entry. Nat. Commun. *7*, 10975.

Hensley, K., and Kursula, P. (2016). Collapsin Response Mediator Protein-2 (CRMP2) is a Plausible Etiological Factor and Potential Therapeutic Target in

Alzheimer's Disease: Comparison and Contrast with Microtubule-Associated Protein Tau. J. Alzheimers Dis. 53, 1–14.

Heo, L., and Feig, M. (2020). Modeling of Severe Acute Respiratory Syndrome Coronavirus 2 (SARS-CoV-2) Proteins by Machine Learning and Physics-Based Refinement. bioRxiv. https://doi.org/10.1101/2020.03.25.008904.

Hernandez-Armenta, C., Ochoa, D., Gonçalves, E., Saez-Rodriguez, J., and Beltrao, P. (2017). Benchmarking substrate-based kinase activity inference using phosphoproteomic data. Bioinformatics 33, 1845–1851.

Hodel, A.E., Hodel, M.R., Griffis, E.R., Hennig, K.A., Ratner, G.A., Xu, S., and Powers, M.A. (2002). The three-dimensional structure of the autoproteolytic, nuclear pore-targeting domain of the human nucleoporin Nup98. Mol. Cell 10, 347–358.

Hoffmann, M., Kleine-Weber, H., Schroeder, S., Krüger, N., Herrler, T., Erichsen, S., Schiergens, T.S., Herrler, G., Wu, N.-H., Nitsche, A., et al. (2020). SARS-CoV-2 Cell Entry Depends on ACE2 and TMPRSS2 and Is Blocked by a Clinically Proven Protease Inhibitor. Cell 181, 271–280.e8.

Holz, M.K., Ballif, B.A., Gygi, S.P., and Blenis, J. (2005). mTOR and S6K1 mediate assembly of the translation preinitiation complex through dynamic protein interchange and ordered phosphorylation events. Cell 123, 569–580.

Hong, S., Freeberg, M.A., Han, T., Kamath, A., Yao, Y., Fukuda, T., Suzuki, T., Kim, J.K., and Inoki, K. (2017). LARP1 functions as a molecular switch for mTORC1-mediated translation of an essential class of mRNAs. eLife 6, e25237.

Horn, H., Schoof, E.M., Kim, J., Robin, X., Miller, M.L., Diella, F., Palma, A., Cesareni, G., Jensen, L.J., and Linding, R. (2014). KinomeXplorer: an integrated platform for kinome biology studies. Nat. Methods 11, 603–604.

Hou, H., Wang, F., Zhang, W., Wang, D., Li, X., Bartlam, M., Yao, X., and Rao, Z. (2011). Structure-functional analyses of CRHSP-24 plasticity and dynamics in oxidative stress response. J. Biol. Chem. 286, 9623–9635.

Hu, F., Gartenhaus, R.B., Eichberg, D., Liu, Z., Fang, H.-B., and Rapoport, A.P. (2010). PBK/TOPK interacts with the DBD domain of tumor suppressor p53 and modulates expression of transcriptional targets including p21. Oncogene 29, 5464–5474.

Hu, J., Stites, E.C., Yu, H., Germino, E.A., Meharena, H.S., Stork, P.J.S., Kornev, A.P., Taylor, S.S., and Shaw, A.S. (2013). Allosteric activation of functionally asymmetric RAF kinase dimers. Cell 154, 1036–1046.

Hu, C.-W., Hsu, C.-L., Wang, Y.-C., Ishihama, Y., Ku, W.-C., Huang, H.-C., and Juan, H.-F. (2015). Temporal Phosphoproteome Dynamics Induced by an ATP Synthase Inhibitor Citreoviridin. Mol. Cell. Proteomics 14, 3284–3298.

Huang, P., and Lai, M.M. (2001). Heterogeneous nuclear ribonucleoprotein a1 binds to the 3′-untranslated region and mediates potential 5′-3′-end cross talks of mouse hepatitis virus RNA. J. Virol. 75, 5009–5017.

Huang, Y.-W., Surka, M.C., Reynaud, D., Pace-Asciak, C., and Trimble, W.S. (2006). GTP binding and hydrolysis kinetics of human septin 2. FEBS J. 273, 3248–3260.

Huang, G., Yan, H., Ye, S., Tong, C., and Ying, Q.-L. (2014). STAT3 phosphorylation at tyrosine 705 and serine 727 differentially regulates mouse ESC fates. Stem Cells 32, 1149–1160.

Hwang, S.-K., Baker, A.R., Young, M.R., and Colburn, N.H. (2014). Tumor suppressor PDCD4 inhibits NF-κB-dependent transcription in human glioblastoma cells by direct interaction with p65. Carcinogenesis 35, 1469–1480.

Ichimura, T., Yamamura, H., Sasamoto, K., Tominaga, Y., Taoka, M., Kakiuchi, K., Shinkawa, T., Takahashi, N., Shimada, S., and Isobe, T. (2005). 14-3-3 proteins modulate the expression of epithelial Na+ channels by phosphorylation-dependent interaction with Nedd4-2 ubiquitin ligase. J. Biol. Chem. 280, 13187–13194.

Inoki, K., Li, Y., Zhu, T., Wu, J., and Guan, K.-L. (2002). TSC2 is phosphorylated and inhibited by Akt and suppresses mTOR signalling. Nat. Cell Biol. 4, 648–657.

Inoue, Y., Sato, H., Fujita, K., Tsukiyama-Kohara, K., Yoneda, M., and Kai, C. (2011). Selective translation of the measles virus nucleocapsid mRNA by la protein. Front. Microbiol. 2, 173.

Intine, R.V., Tenenbaum, S.A., Sakulich, A.L., Keene, J.D., and Maraia, R.J. (2003). Differential phosphorylation and subcellular localization of La RNPs associated with precursor tRNAs and translation-related mRNAs. Mol. Cell 12, 1301–1307.

Ishii, T., Warabi, E., Siow, R.C.M., and Mann, G.E. (2013). Sequestosome1/p62: a regulator of redox-sensitive voltage-activated potassium channels, arterial remodeling, inflammation, and neurite outgrowth. Free Radic. Biol. Med. 65, 102–116.

Ishikawa, Y., Kawabata, S., and Sakurai, H. (2015). HSF1 transcriptional activity is modulated by IER5 and PP2A/B55. FEBS Lett. 589, 1150–1155.

Izawa, I., and Inagaki, M. (2006). Regulatory mechanisms and functions of intermediate filaments: a study using site- and phosphorylation state-specific antibodies. Cancer Sci. 97, 167–174.

Jacque, J.-M., and Stevenson, M. (2006). The inner-nuclear-envelope protein emerin regulates HIV-1 infectivity. Nature 441, 641–645.

Jang, S.H., Jun, C.-D., and Park, Z.-Y. (2015). Label-free quantitative phosphorylation analysis of human transgelin2 in Jurkat T cells reveals distinct phosphorylation patterns under PKA and PKC activation conditions. Proteome Sci. 13, 14.

Jassal, B., Matthews, L., Viteri, G., Gong, C., Lorente, P., Fabregat, A., Sidiropoulos, K., Cook, J., Gillespie, M., Haw, R., et al. (2020). The reactome pathway knowledgebase. Nucleic Acids Res. 48 (D1), D498–D503.

Jiang, Y., Li, X., Yang, W., Hawke, D.H., Zheng, Y., Xia, Y., Aldape, K., Wei, C., Guo, F., Chen, Y., and Lu, Z. (2014). PKM2 regulates chromosome segregation and mitosis progression of tumor cells. Mol. Cell 53, 75–87.

Jimenez-Guardeño, J.M., Nieto-Torres, J.L., DeDiego, M.L., Regla-Nava, J.A., Fernandez-Delgado, R., Castaño-Rodriguez, C., and Enjuanes, L. (2014). The PDZ-binding motif of severe acute respiratory syndrome coronavirus envelope protein is a determinant of viral pathogenesis. PLoS Pathog. 10, e1004320.

Johnson, C., Tinti, M., Wood, N.T., Campbell, D.G., Toth, R., Dubois, F., Geraghty, K.M., Wong, B.H.C., Brown, L.J., Tyler, J., et al. (2011). Visualization and biochemical analyses of the emerging mammalian 14-3-3-phosphoproteome. Mol. Cell. Proteomics 10, M110.005751.

Johnson, J.R., Crosby, D.C., Hultquist, J.F., Li, D., Marlett, J., Swann, J., Hüttenhain, R., Verschueren, E., Johnson, T.L., Newton, B.W., et al. (2020). Global post-translational modification profiling of HIV-1-infected cells reveals mechanisms of host cellular pathway remodeling. bioRxiv. https://doi.org/10.1101/2020.01.06.896365.

Kane, S., Sano, H., Liu, S.C.H., Asara, J.M., Lane, W.S., Garner, C.C., and Lienhard, G.E. (2002). A method to identify serine kinase substrates. Akt phosphorylates a novel adipocyte protein with a Rab GTPase-activating protein (GAP) domain. J. Biol. Chem. 277, 22115–22118.

Kang, S., Yang, M., Hong, Z., Zhang, L., Huang, Z., Chen, X., He, S., Zhou, Z., Zhou, Z., Chen, Q., et al. (2020). Crystal structure of SARS-CoV-2 nucleocapsid protein RNA binding domain reveals potential unique drug targeting sites. Acta Pharm. Sin. B. Published online April 20, 2020. https://doi.org/10.1016/j.apsb.2020.04.009.

Kanzawa, N., Nishigaki, K., Hayashi, T., Ishii, Y., Furukawa, S., Niiro, A., Yasui, F., Kohara, M., Morita, K., Matsushima, K., et al. (2006). Augmentation of chemokine production by severe acute respiratory syndrome coronavirus 3a/X1 and 7a/X4 proteins through NF-kappaB activation. FEBS Lett. 580, 6807–6812.

Karin, M. (1995). The regulation of AP-1 activity by mitogen-activated protein kinases. J. Biol. Chem. 270, 16483–16486.

Kastenhuber, E.R., and Lowe, S.W. (2017). Putting p53 in Context. Cell 170, 1062–1078.

Katayama, H., Sasai, K., Kawai, H., Yuan, Z.-M., Bondaruk, J., Suzuki, F., Fujii, S., Arlinghaus, R.B., Czerniak, B.A., and Sen, S. (2004). Phosphorylation by aurora kinase A induces Mdm2-mediated destabilization and inhibition of p53. Nat. Genet. 36, 55–62.

Kennedy, D., Mnich, K., Oommen, D., Chakravarthy, R., Almeida-Souza, L., Krols, M., Saveljeva, S., Doyle, K., Gupta, S., Timmerman, V., et al. (2017). HSPB1 facilitates ERK-mediated phosphorylation and degradation of BIM to

attenuate endoplasmic reticulum stress-induced apoptosis. Cell Death Dis. *8*, e3026.

Khurana, N., and Bhattacharyya, S. (2015). Hsp90, the concertmaster: tuning transcription. Front. Oncol. *5*, 100.

Killoran, R.C., Fan, J., Yang, D., Shilton, B.H., and Choy, W.-Y. (2015). Structural Analysis of the 14-3-3ζ/Chibby Interaction Involved in Wnt/β-Catenin Signaling. PLoS ONE *10*, e0123934.

Kim, Y.-K., Lee, K.J., Jeon, H., and Yu, Y.G. (2006). Protein kinase CK2 is inhibited by human nucleolar phosphoprotein p140 in an inositol hexakisphosphate-dependent manner. J. Biol. Chem. *281*, 36752–36757.

Kindrachuk, J., Ork, B., Hart, B.J., Mazur, S., Holbrook, M.R., Frieman, M.B., Traynor, D., Johnson, R.F., Dyall, J., Kuhn, J.H., et al. (2015). Antiviral potential of ERK/MAPK and PI3K/AKT/mTOR signaling modulation for Middle East respiratory syndrome coronavirus infection as identified by temporal kinome analysis. Antimicrob. Agents Chemother. *59*, 1088–1099.

Kishimoto, H., Nakagawa, K., Watanabe, T., Kitagawa, D., Momose, H., Seo, J., Nishitai, G., Shimizu, N., Ohata, S., Tanemura, S., et al. (2003). Different properties of SEK1 and MKK7 in dual phosphorylation of stress-induced activated protein kinase SAPK/JNK in embryonic stem cells. J. Biol. Chem. *278*, 16595–16601.

Kjolby, M., Andersen, O.M., Breiderhoff, T., Fjorback, A.W., Pedersen, K.M., Madsen, P., Jansen, P., Heeren, J., Willnow, T.E., and Nykjaer, A. (2010). Sort1, encoded by the cardiovascular risk locus 1p13.3, is a regulator of hepatic lipoprotein export. Cell Metab. *12*, 213–223.

Koff, A., Giordano, A., Desai, D., Yamashita, K., Harper, J.W., Elledge, S., Nishimoto, T., Morgan, D.O., Franza, B.R., and Roberts, J.M. (1992). Formation and activation of a cyclin E-cdk2 complex during the G1 phase of the human cell cycle. Science *257*, 1689–1694.

Kohl, B., Zhong, X., Herrmann, C., and Stoll, R. (2019). Phosphorylation orchestrates the structural ensemble of the intrinsically disordered protein HMGA1a and modulates its DNA binding to the NFκB promoter. Nucleic Acids Res. *47*, 11906–11920.

Koseki, T., Inohara, N., Chen, S., Carrio, R., Merino, J., Hottiger, M.O., Nabel, G.J., and Núñez, G. (1999). CIPER, a novel NF kappaB-activating protein containing a caspase recruitment domain with homology to Herpesvirus-2 protein E10. J. Biol. Chem. *274*, 9955–9961.

Kostenko, S., Johannessen, M., and Moens, U. (2009). PKA-induced F-actin rearrangement requires phosphorylation of Hsp27 by the MAPKAP kinase MK5. Cell. Signal. *21*, 712–718.

Kotula, E., Faigle, W., Berthault, N., Dingli, F., Loew, D., Sun, J.-S., Dutreix, M., and Quanz, M. (2013). DNA-PK target identification reveals novel links between DNA repair signaling and cytoskeletal regulation. PLoS ONE *8*, e80313.

Kovacina, K.S., Park, G.Y., Bae, S.S., Guzzetta, A.W., Schaefer, E., Birnbaum, M.J., and Roth, R.A. (2003). Identification of a proline-rich Akt substrate as a 14-3-3 binding partner. J. Biol. Chem. *278*, 10189–10194.

Kraft, C., Herzog, F., Gieffers, C., Mechtler, K., Hagting, A., Pines, J., and Peters, J.M. (2003). Mitotic regulation of the human anaphase-promoting complex by phosphorylation. EMBO J. *22*, 6598–6609.

Kramer, E.R., Gieffers, C., Hölzl, G., Hengstschläger, M., and Peters, J.M. (1998). Activation of the human anaphase-promoting complex by proteins of the CDC20/Fizzy family. Curr. Biol. *8*, 1207–1210.

Kremer, B.E., Adang, L.A., and Macara, I.G. (2007). Septins regulate actin organization and cell-cycle arrest through nuclear accumulation of NCK mediated by SOCS7. Cell *130*, 837–850.

Krull, S., Dörries, J., Boysen, B., Reidenbach, S., Magnius, L., Norder, H., Thyberg, J., and Cordes, V.C. (2010). Protein Tpr is required for establishing nuclear pore-associated zones of heterochromatin exclusion. EMBO J. *29*, 1659–1673.

Kuang, X.-Y., Jiang, H.-S., Li, K., Zheng, Y.-Z., Liu, Y.-R., Qiao, F., Li, S., Hu, X., and Shao, Z.-M. (2016). The phosphorylation-specific association of STMN1 with GRP78 promotes breast cancer metastasis. Cancer Lett. *377*, 87–96.

Kumar, R., Whitehurst, C.B., and Pagano, J.S. (2014). The Rad6/18 ubiquitin complex interacts with the Epstein-Barr virus deubiquitinating enzyme, BPLF1, and contributes to virus infectivity. J. Virol. *88*, 6411–6422.

Kumar, R., Khandelwal, N., Thachamvally, R., Tripathi, B.N., Barua, S., Kashyap, S.K., Maherchandani, S., and Kumar, N. (2018). Role of MAPK/MNK1 signaling in virus replication. Virus Res. *253*, 48–61.

Kunapuli, P., Kasyapa, C.S., Chin, S.-F., Caldas, C., and Cowell, J.K. (2006). ZNF198, a zinc finger protein rearranged in myeloproliferative disease, localizes to the PML nuclear bodies and interacts with SUMO-1 and PML. Exp. Cell Res. *312*, 3739–3751.

Kuss, S.K., Mata, M.A., Zhang, L., and Fontoura, B.M.A. (2013). Nuclear imprisonment: viral strategies to arrest host mRNA nuclear export. Viruses *5*, 1824–1849.

Labit, H., Fujimitsu, K., Bayin, N.S., Takaki, T., Gannon, J., and Yamano, H. (2012). Dephosphorylation of Cdc20 is required for its C-box-dependent activation of the APC/C. EMBO J. *31*, 3351–3362.

Lai, C.-C., Shih, T.-P., Ko, W.-C., Tang, H.-J., and Hsueh, P.-R. (2020). Severe acute respiratory syndrome coronavirus 2 (SARS-CoV-2) and coronavirus disease-2019 (COVID-19): The epidemic and the challenges. Int. J. Antimicrob. Agents *55*, 105924.

Lamarche-Vane, N., and Hall, A. (1998). CdGAP, a novel proline-rich GTPase-activating protein for Cdc42 and Rac. J. Biol. Chem. *273*, 29172–29177.

Lan, J., Ge, J., Yu, J., Shan, S., Zhou, H., Fan, S., Zhang, Q., Shi, X., Wang, Q., Zhang, L., and Wang, X. (2020). Structure of the SARS-CoV-2 spike receptor-binding domain bound to the ACE2 receptor. Nature *581*, 215–220.

Langfelder, P., Zhang, B., and Horvath, S. (2008). Defining clusters from a hierarchical cluster tree: the Dynamic Tree Cut package for R. Bioinformatics *24*, 719–720.

Larance, M., Rowland, A.F., Hoehn, K.L., Humphreys, D.T., Preiss, T., Guilhaus, M., and James, D.E. (2010). Global phosphoproteomics identifies a major role for AKT and 14-3-3 in regulating EDC3. Mol. Cell. Proteomics *9*, 682–694.

Lau, E., Zhu, C., Abraham, R.T., and Jiang, W. (2006). The functional role of Cdc6 in S-G2/M in mammalian cells. EMBO Rep. *7*, 425–430.

Law, A.H.Y., Lee, D.C.W., Cheung, B.K.W., Yim, H.C.H., and Lau, A.S.Y. (2007). Role for nonstructural protein 1 of severe acute respiratory syndrome coronavirus in chemokine dysregulation. J. Virol. *81*, 416–422.

Le Sage, V., Cinti, A., Amorim, R., and Mouland, A.J. (2016). Adapting the Stress Response: Viral Subversion of the mTOR Signaling Pathway. Viruses *8*, 152.

Lee, K.-Y., and Myung, K. (2008). PCNA modifications for regulation of post-replication repair pathways. Mol. Cells *26*, 5–11.

Lee, J., Hong, F., Kwon, S., Kim, S.S., Kim, D.O., Kang, H.S., Lee, S.J., Ha, J., and Kim, S.S. (2002). Activation of p38 MAPK induces cell cycle arrest via inhibition of Raf/ERK pathway during muscle differentiation. Biochem. Biophys. Res. Commun. *298*, 765–771.

Lee, S., Salwinski, L., Zhang, C., Chu, D., Sampankanpanich, C., Reyes, N.A., Vangeloff, A., Xing, F., Li, X., Wu, T.-T., et al. (2011). An integrated approach to elucidate the intra-viral and viral-cellular protein interaction networks of a gamma-herpesvirus. PLoS Pathog. *7*, e1002297.

Lee, K.-Y., Liu, L., Jin, Y., Fu, S.-B., and Rosales, J.L. (2012). Cdk5 mediates vimentin Ser56 phosphorylation during GTP-induced secretion by neutrophils. J. Cell. Physiol. *227*, 739–750.

Lee, W.-K., Son, S.H., Jin, B.-S., Na, J.-H., Kim, S.-Y., Kim, K.-H., Kim, E.E., Yu, Y.G., and Lee, H.H. (2013). Structural and functional insights into the regulation mechanism of CK2 by IP6 and the intrinsically disordered protein Nopp140. Proc. Natl. Acad. Sci. USA *110*, 19360–19365.

Leite, F., and Way, M. (2015). The role of signalling and the cytoskeleton during Vaccinia Virus egress. Virus Res. *209*, 87–99.

Lekmine, F., Uddin, S., Sassano, A., Parmar, S., Brachmann, S.M., Majchrzak, B., Sonenberg, N., Hay, N., Fish, E.N., and Platanias, L.C. (2003). Activation of the p70 S6 kinase and phosphorylation of the 4E-BP1 repressor of mRNA translation by type I interferons. J. Biol. Chem. *278*, 27772–27780.

Lekmine, F., Sassano, A., Uddin, S., Smith, J., Majchrzak, B., Brachmann, S.M., Hay, N., Fish, E.N., and Platanias, L.C. (2004). Interferon-gamma engages the p70 S6 kinase to regulate phosphorylation of the 40S S6 ribosomal protein. Exp. Cell Res. 295, 173–182.

Leukel, M., and Jost, E. (1995). Two conserved serines in the nuclear localization signal flanking region are involved in the nuclear targeting of human lamin A. Eur. J. Cell Biol. 68, 133–142.

Levy, D.E., and Lee, C.-K. (2002). What does Stat3 do? J. Clin. Invest. 109, 1143–1148.

Li, Q., and Martinez, J.D. (2011). Loss of HSF1 results in defective radiation-induced G(2) arrest and DNA repair. Radiat. Res. 176, 17–24.

Li, Z., and Nagy, P.D. (2011). Diverse roles of host RNA binding proteins in RNA virus replication. RNA Biol. 8, 305–315.

Li, F.Q., Tam, J.P., and Liu, D.X. (2007a). Cell cycle arrest and apoptosis induced by the coronavirus infectious bronchitis virus in the absence of p53. Virology 365, 435–445.

Li, Y., Roux, C., Lazereg, S., LeCaer, J.-P., Laprévote, O., Badet, B., and Badet-Denisot, M.-A. (2007b). Identification of a novel serine phosphorylation site in human glutamine:fructose-6-phosphate amidotransferase isoform 1. Biochemistry 46, 13163–13169.

Li, F.-Q., Mofunanya, A., Harris, K., and Takemaru, K. (2008). Chibby cooperates with 14-3-3 to regulate beta-catenin subcellular distribution and signaling activity. J. Cell Biol. 181, 1141–1154.

Li, G., Ma, D., and Chen, Y. (2016). Cellular functions of programmed cell death 5. Biochim. Biophys. Acta 1863, 572–580.

Li, J., Chen, C., Li, Y., Matye, D.J., Wang, Y., Ding, W.-X., and Li, T. (2017). Inhibition of insulin/PI3K/AKT signaling decreases adipose Sortilin 1 in mice and 3T3-L1 adipocytes. Biochim Biophys Acta Mol Basis Dis 1863, 2924–2933.

Liang, J., Cao, R., Zhang, Y., Xia, Y., Zheng, Y., Li, X., Wang, L., Yang, W., and Lu, Z. (2016). PKM2 dephosphorylation by Cdc25A promotes the Warburg effect and tumorigenesis. Nat. Commun. 7, 12431.

Liao, Q.-J., Ye, L.-B., Timani, K.A., Zeng, Y.-C., She, Y.-L., Ye, L., and Wu, Z.-H. (2005). Activation of NF-kappaB by the full-length nucleocapsid protein of the SARS coronavirus. Acta Biochim. Biophys. Sin. (Shanghai) 37, 607–612.

Lieberman, H.B., Panigrahi, S.K., Hopkins, K.M., Wang, L., and Broustas, C.G. (2017). p53 and RAD9, the DNA Damage Response, and Regulation of Transcription Networks. Radiat. Res. 187, 424–432.

Lilley, C.E., Schwartz, R.A., and Weitzman, M.D. (2007). Using or abusing: viruses and the cellular DNA damage response. Trends Microbiol. 15, 119–126.

Lim, H.C., Xie, L., Zhang, W., Li, R., Chen, Z.-C., Wu, G.-Z., Cui, S.-S., Tan, E.K., and Zeng, L. (2013). Ribosomal S6 Kinase 2 (RSK2) maintains genomic stability by activating the Atm/p53-dependent DNA damage pathway. PLoS ONE 8, e74334.

Lin, J.-Y., Li, M.-L., and Shih, S.-R. (2009). Far upstream element binding protein 2 interacts with enterovirus 71 internal ribosomal entry site and negatively regulates viral translation. Nucleic Acids Res. 37, 47–59.

Lin, X., Li, S., Zhao, Y., Ma, X., Zhang, K., He, X., and Wang, Z. (2013). Interaction domains of p62: a bridge between p62 and selective autophagy. DNA Cell Biol. 32, 220–227.

Lingel, H., Wissing, J., Arra, A., Schanze, D., Lienenklaus, S., Klawonn, F., Pierau, M., Zenker, M., Jänsch, L., and Brunner-Weinzierl, M.C. (2017). CTLA-4-mediated posttranslational modifications direct cytotoxic T-lymphocyte differentiation. Cell Death Differ. 24, 1739–1749.

Lisnock, J., Griffin, P., Calaycay, J., Frantz, B., Parsons, J., O'Keefe, S.J., and LoGrasso, P. (2000). Activation of JNK3 alpha 1 requires both MKK4 and MKK7: kinetic characterization of in vitro phosphorylated JNK3 alpha 1. Biochemistry 39, 3141–3148.

Lista, M.J., Page, R., Sertkaya, H., Matos, P., Ortiz-Zapater, E., Maguire, T.J.A., Poulton, K., O'Byrne, A., Bouton, C., Dickenson, R.E., et al. (2020). Resilient SARS-CoV-2 diagnostics workflows including viral heat inactivation. Nature 581, 215–220.

Liu, Y., and Schneider, M.F. (2013). Opposing HDAC4 nuclear fluxes due to phosphorylation by β-adrenergic activated protein kinase A or by activity or Epac activated CaMKII in skeletal muscle fibres. J. Physiol. 591, 3605–3623.

Liu, Y., Tan, H., Tian, H., Liang, C., Chen, S., and Liu, Q. (2011). Autoantigen La promotes efficient RNAi, antiviral response, and transposon silencing by facilitating multiple-turnover RISC catalysis. Mol. Cell 44, 502–508.

Liu, R.-Y., Diao, C.-F., Zhang, Y., Wu, N., Wan, H.-Y., Nong, X.-Y., Liu, M., and Tang, H. (2013). miR-371-5p down-regulates pre mRNA processing factor 4 homolog B (PRPF4B) and facilitates the G1/S transition in human hepatocellular carcinoma cells. Cancer Lett. 335, 351–360.

Liu, A.-L., Li, Y.-F., Qi, W., Ma, X.-L., Yu, K.-X., Huang, B., Liao, M., Li, F., Pan, J., and Song, M.-X. (2015). Comparative analysis of selected innate immune-related genes following infection of immortal DF-1 cells with highly pathogenic (H5N1) and low pathogenic (H9N2) avian influenza viruses. Virus Genes 50, 189–199.

Lobry, C., Lopez, T., Israël, A., and Weil, R. (2007). Negative feedback loop in T cell activation through IkappaB kinase-induced phosphorylation and degradation of Bcl10. Proc. Natl. Acad. Sci. USA 104, 908–913.

Lokireddy, S., Kukushkin, N.V., and Goldberg, A.L. (2015). cAMP-induced phosphorylation of 26S proteasomes on Rpn6/PSMD11 enhances their activity and the degradation of misfolded proteins. Proc. Natl. Acad. Sci. USA 112, E7176–E7185.

Long, L., Thelen, J.P., Furgason, M., Haj-Yahya, M., Brik, A., Cheng, D., Peng, J., and Yao, T. (2014). The U4/U6 recycling factor SART3 has histone chaperone activity and associates with USP15 to regulate H2B deubiquitination. J. Biol. Chem. 289, 8916–8930.

Love, M.I., Huber, W., and Anders, S. (2014). Moderated estimation of fold change and dispersion for RNA-seq data with DESeq2. Genome Biol. 15, 550.

Lu, Y., Liu, C., Xu, Y.-F., Cheng, H., Shi, S., Wu, C.-T., and Yu, X.-J. (2014). Stathmin destabilizing microtubule dynamics promotes malignant potential in cancer cells by epithelial-mesenchymal transition. HBPD INT 13, 386–394.

Lu, H., Shamanna, R.A., de Freitas, J.K., Okur, M., Khadka, P., Kulikowicz, T., Holland, P.P., Tian, J., Croteau, D.L., Davis, A.J., and Bohr, V.A. (2017). Cell cycle-dependent phosphorylation regulates RECQL4 pathway choice and ubiquitination in DNA double-strand break repair. Nat. Commun. 8, 2039.

Lubas, M., Christensen, M.S., Kristiansen, M.S., Domanski, M., Falkenby, L.G., Lykke-Andersen, S., Andersen, J.S., Dziembowski, A., and Jensen, T.H. (2011). Interaction profiling identifies the human nuclear exosome targeting complex. Mol. Cell 43, 624–637.

Luciani, M.G., Hutchins, J.R., Zheleva, D., and Hupp, T.R. (2000). The C-terminal regulatory domain of p53 contains a functional docking site for cyclin A. J. Mol. Biol. 300, 503–518.

Lukas, J., Lukas, C., and Bartek, J. (2011). More than just a focus: The chromatin response to DNA damage and its role in genome integrity maintenance. Nat. Cell Biol. 13, 1161–1169.

Luo, H., Chen, Q., Chen, J., Chen, K., Shen, X., and Jiang, H. (2005). The nucleocapsid protein of SARS coronavirus has a high binding affinity to the human cellular heterogeneous nuclear ribonucleoprotein A1. FEBS Lett. 579, 2623–2628.

Ly, T., Ahmad, Y., Shlien, A., Soroka, D., Mills, A., Emanuele, M.J., Stratton, M.R., and Lamond, A.I. (2014). A proteomic chronology of gene expression through the cell cycle in human myeloid leukemia cells. eLife 3, e01630.

Ly, T., Whigham, A., Clarke, R., Brenes-Murillo, A.J., Estes, B., Madhessian, D., Lundberg, E., Wadsworth, P., and Lamond, A.I. (2017). Proteomic analysis of cell cycle progression in asynchronous cultures, including mitotic subphases, using PRIMMUS. eLife 6, e27574.

Machado-Neto, J.A., Saad, S.T.O., and Traina, F. (2014). Stathmin 1 in normal and malignant hematopoiesis. BMB Rep. 47, 660–665.

Machowska, M., Piekarowicz, K., and Rzepecki, R. (2015). Regulation of lamin properties and functions: does phosphorylation do it all? Open Biol. 5, 150094.

Madureira, P.A., Hill, R., Lee, P.W.K., and Waisman, D.M. (2012). Genotoxic agents promote the nuclear accumulation of annexin A2: role of annexin A2 in mitigating DNA damage. PLoS ONE 7, e50591.

Magnuson, B., Ekim, B., and Fingar, D.C. (2012). Regulation and function of ribosomal protein S6 kinase (S6K) within mTOR signalling networks. Biochem. J. *441*, 1–21.

Magron, A., Elowe, S., and Carreau, M. (2015). The Fanconi Anemia C Protein Binds to and Regulates Stathmin-1 Phosphorylation. PLoS ONE *10*, e0140612.

Mahony, R., Broadbent, L., Maier-Moore, J.S., Power, U.F., and Jefferies, C.A. (2017). The RNA binding protein La/SS-B promotes RIG-I-mediated type I and type III IFN responses following Sendai viral infection. Sci. Rep. *7*, 14537.

Mancini, M., Soverini, S., Gugliotta, G., Santucci, M.A., Rosti, G., Cavo, M., Martinelli, G., and Castagnetti, F. (2017). Chibby 1: a new component of β-catenin-signaling in chronic myeloid leukemia. Oncotarget *8*, 88244–88250.

Mandl, M., Slack, D.N., and Keyse, S.M. (2005). Specific inactivation and nuclear anchoring of extracellular signal-regulated kinase 2 by the inducible dual-specificity protein phosphatase DUSP5. Mol. Cell. Biol. *25*, 1830–1845.

Mangin, P.H., Kleitz, L., Boucheix, C., Gachet, C., and Lanza, F. (2009). CD9 negatively regulates integrin alphaIIbbeta3 activation and could thus prevent excessive platelet recruitment at sites of vascular injury. J. Thromb. Haemost. *7*, 900–902.

Manning, B.D., and Toker, A. (2017). AKT/PKB Signaling: Navigating the Network. Cell *169*, 381–405.

Marcos-Villar, L., Pazo, A., and Nieto, A. (2016). Influenza Virus and Chromatin: Role of the CHD1 Chromatin Remodeler in the Virus Life Cycle. J. Virol. *90*, 3694–3707.

Marklund, U., Brattsand, G., Osterman, O., Ohlsson, P.I., and Gullberg, M. (1993). Multiple signal transduction pathways induce phosphorylation of serines 16, 25, and 38 of oncoprotein 18 in T lymphocytes. J. Biol. Chem. *268*, 25671–25680.

Marklund, U., Larsson, N., Gradin, H.M., Brattsand, G., and Gullberg, M. (1996). Oncoprotein 18 is a phosphorylation-responsive regulator of microtubule dynamics. EMBO J. *15*, 5290–5298.

Marquette, A., André, J., Bagot, M., Bensussan, A., and Dumaz, N. (2011). ERK and PDE4 cooperate to induce RAF isoform switching in melanoma. Nat. Struct. Mol. Biol. *18*, 584–591.

Mather, K.A., Thalamuthu, A., Oldmeadow, C., Song, F., Armstrong, N.J., Poljak, A., Holliday, E.G., McEvoy, M., Kwok, J.B., Assareh, A.A., et al. (2016). Genome-wide significant results identified for plasma apolipoprotein H levels in middle-aged and older adults. Sci. Rep. *6*, 23675.

Matsuhashi, S., Manirujjaman, M., Hamajima, H., and Ozaki, I. (2019). Control Mechanisms of the Tumor Suppressor PDCD4: Expression and Functions. Int. J. Mol. Sci. *20*, 2304.

Matsumoto, T., Urushido, M., Ide, H., Ishihara, M., Hamada-Ode, K., Shimamura, Y., Ogata, K., Inoue, K., Taniguchi, Y., Taguchi, T., et al. (2015). Small Heat Shock Protein Beta-1 (HSPB1) Is Upregulated and Regulates Autophagy and Apoptosis of Renal Tubular Cells in Acute Kidney Injury. PLoS ONE *10*, e0126229.

Matsuoka, Y., Nagahara, Y., Ikekita, M., and Shinomiya, T. (2003). A novel immunosuppressive agent FTY720 induced Akt dephosphorylation in leukemia cells. Br. J. Pharmacol. *138*, 1303–1312.

Mbonye, U.R., Wang, B., Gokulrangan, G., Chance, M.R., and Karn, J. (2015). Phosphorylation of HEXIM1 at Tyr271 and Tyr274 Promotes Release of P-TEFb from the 7SK snRNP Complex and Enhances Proviral HIV Gene Expression. Proteomics *15*, 2078–2086.

McCamphill, P.K., Farah, C.A., Anadolu, M.N., Hoque, S., and Sossin, W.S. (2015). Bidirectional regulation of eEF2 phosphorylation controls synaptic plasticity by decoding neuronal activity patterns. J. Neurosci. *35*, 4403–4417.

McClain, D.A., Lubas, W.A., Cooksey, R.C., Hazel, M., Parker, G.J., Love, D.C., and Hanover, J.A. (2002). Altered glycan-dependent signaling induces insulin resistance and hyperleptinemia. Proc. Natl. Acad. Sci. USA *99*, 10695–10699.

Mehellou, Y., Alamri, M.A., Dhiani, B.A., and Kadri, H. (2018). C-terminal phosphorylation of SPAK and OSR1 kinases promotes their binding and activation by the scaffolding protein MO25. Biochem. Biophys. Res. Commun. *503*, 1868–1873.

Meier, U.T., and Blobel, G. (1990). A nuclear localization signal binding protein in the nucleolus. J. Cell Biol. *111*, 2235–2245.

Meier, U.T., and Blobel, G. (1992). Nopp140 shuttles on tracks between nucleolus and cytoplasm. Cell *70*, 127–138.

Mendoza, M.C., Er, E.E., Zhang, W., Ballif, B.A., Elliott, H.L., Danuser, G., and Blenis, J. (2011). ERK-MAPK drives lamellipodia protrusion by activating the WAVE2 regulatory complex. Mol. Cell *41*, 661–671.

Menon, S., Dibble, C.C., Talbott, G., Hoxhaj, G., Valvezan, A.J., Takahashi, H., Cantley, L.C., and Manning, B.D. (2014). Spatial control of the TSC complex integrates insulin and nutrient regulation of mTORC1 at the lysosome. Cell *156*, 771–785.

Mizutani, T., Fukushi, S., Saijo, M., Kurane, I., and Morikawa, S. (2004). Phosphorylation of p38 MAPK and its downstream targets in SARS coronavirus-infected cells. Biochem. Biophys. Res. Commun. *319*, 1228–1234.

Mo, M., Shahar, S., Fleming, S.B., and Mercer, A.A. (2012). How viruses affect the cell cycle through manipulation of the APC/C. Trends Microbiol. *20*, 440–448.

Moldave, K. (1985). Eukaryotic protein synthesis. Annu. Rev. Biochem. *54*, 1109–1149.

Morris, E.J., Kawamura, E., Gillespie, J.A., Balgi, A., Kannan, N., Muller, W.J., Roberge, M., and Dedhar, S. (2017). Stat3 regulates centrosome clustering in cancer cells via Stathmin/PLK1. Nat. Commun. *8*, 15289.

Muda, M., Theodosiou, A., Rodrigues, N., Boschert, U., Camps, M., Gillieron, C., Davies, K., Ashworth, A., and Arkinstall, S. (1996). The dual specificity phosphatases M3/6 and MKP-3 are highly selective for inactivation of distinct mitogen-activated protein kinases. J. Biol. Chem. *271*, 27205–27208.

Mueller, P.R., Coleman, T.R., Kumagai, A., and Dunphy, W.G. (1995). Myt1: a membrane-associated inhibitory kinase that phosphorylates Cdc2 on both threonine-14 and tyrosine-15. Science *270*, 86–90.

Mueller, D., Bach, C., Zeisig, D., Garcia-Cuellar, M.-P., Monroe, S., Sreekumar, A., Zhou, R., Nesvizhskii, A., Chinnaiyan, A., Hess, J.L., and Slany, R.K. (2007). A role for the MLL fusion partner ENL in transcriptional elongation and chromatin modification. Blood *110*, 4445–4454.

Müller, S., Montes de Oca, R., Lacoste, N., Dingli, F., Loew, D., and Almouzni, G. (2014). Phosphorylation and DNA binding of HJURP determine its centromeric recruitment and function in CenH3(CENP-A) loading. Cell Rep. *8*, 190–203.

Na, B.-R., Kim, H.-R., Piragyte, I., Oh, H.-M., Kwon, M.-S., Akber, U., Lee, H.-S., Park, D.-S., Song, W.K., Park, Z.-Y., et al. (2015). TAGLN2 regulates T cell activation by stabilizing the actin cytoskeleton at the immunological synapse. J. Cell Biol. *209*, 143–162.

Nairn, A.C., Matsushita, M., Nastiuk, K., Horiuchi, A., Mitsui, K., Shimizu, Y., and Palfrey, H.C. (2001). Elongation factor-2 phosphorylation and the regulation of protein synthesis by calcium. Prog. Mol. Subcell. Biol. *27*, 91–129.

Nandi, A.K., Ford, T., Fleksher, D., Neuman, B., and Rapoport, A.P. (2007). Attenuation of DNA damage checkpoint by PBK, a novel mitotic kinase, involves protein-protein interaction with tumor suppressor p53. Biochem. Biophys. Res. Commun. *358*, 181–188.

Needham, E.J., Humphrey, S.J., Cooke, K.C., Fazakerley, D.J., Duan, X., Parker, B.L., and James, D.E. (2019). Phosphoproteomics of Acute Cell Stressors Targeting Exercise Signaling Networks Reveal Drug Interactions Regulating Protein Secretion. Cell Rep. *29*, 1524–1538.e6.

Ng, P.C., and Henikoff, S. (2003). SIFT: Predicting amino acid changes that affect protein function. Nucleic Acids Res. *31*, 3812–3814.

Nielsen, M.S., Madsen, P., Christensen, E.I., Nykjaer, A., Gliemann, J., Kasper, D., Pohlmann, R., and Petersen, C.M. (2001). The sortilin cytoplasmic tail conveys Golgi-endosome transport and binds the VHS domain of the GGA2 sorting protein. EMBO J. *20*, 2180–2190.

Ochoa, D., Jonikas, M., Lawrence, R.T., El Debs, B., Selkrig, J., Typas, A., Villén, J., Santos, S.D., and Beltrao, P. (2016). An atlas of human kinase regulation. Mol. Syst. Biol. *12*, 888.

Ochoa, D., Jarnuczak, A.F., Viéitez, C., Gehre, M., Soucheray, M., Mateus, A., Kleefeldt, A.A., Hill, A., Garcia-Alonso, L., Stein, F., et al. (2020). The functional landscape of the human phosphoproteome. Nat. Biotechnol. *38*, 365–373.

Ogiso, H., Kagi, N., Matsumoto, E., Nishimoto, M., Arai, R., Shirouzu, M., Mimura, J., Fujii-Kuriyama, Y., and Yokoyama, S. (2004). Phosphorylation analysis of 90 kDa heat shock protein within the cytosolic arylhydrocarbon receptor complex. Biochemistry *43*, 15510–15519.

Ohtsubo, M., Theodoras, A.M., Schumacher, J., Roberts, J.M., and Pagano, M. (1995). Human cyclin E, a nuclear protein essential for the G1-to-S phase transition. Mol. Cell. Biol. *15*, 2612–2624.

Old, W.M., Shabb, J.B., Houel, S., Wang, H., Couts, K.L., Yen, C.-Y., Litman, E.S., Croy, C.H., Meyer-Arendt, K., Miranda, J.G., et al. (2009). Functional proteomics identifies targets of phosphorylation by B-Raf signaling in melanoma. Mol. Cell *34*, 115–131.

Olsen, J.V., Blagoev, B., Gnad, F., Macek, B., Kumar, C., Mortensen, P., and Mann, M. (2006). Global, in vivo, and site-specific phosphorylation dynamics in signaling networks. Cell *127*, 635–648.

Olsen, J.V., Vermeulen, M., Santamaria, A., Kumar, C., Miller, M.L., Jensen, L.J., Gnad, F., Cox, J., Jensen, T.S., Nigg, E.A., et al. (2010). Quantitative phosphoproteomics reveals widespread full phosphorylation site occupancy during mitosis. Sci. Signal. *3*, ra3.

Osada, N., Kohara, A., Yamaji, T., Hirayama, N., Kasai, F., Sekizuka, T., Kuroda, M., and Hanada, K. (2014). The genome landscape of the african green monkey kidney-derived vero cell line. DNA Res. *21*, 673–683.

Oshiro, N., Takahashi, R., Yoshino, K., Tanimura, K., Nakashima, A., Eguchi, S., Miyamoto, T., Hara, K., Takehana, K., Avruch, J., et al. (2007). The proline-rich Akt substrate of 40 kDa (PRAS40) is a physiological substrate of mammalian target of rapamycin complex 1. J. Biol. Chem. *282*, 20329–20339.

Ou, X., Liu, Y., Lei, X., Li, P., Mi, D., Ren, L., Guo, L., Guo, R., Chen, T., Hu, J., et al. (2020). Characterization of spike glycoprotein of SARS-CoV-2 on virus entry and its immune cross-reactivity with SARS-CoV. Nat. Commun. *11*, 1620.

Palamarchuk, A., Efanov, A., Maximov, V., Aqeilan, R.I., Croce, C.M., and Pekarsky, Y. (2005). Akt phosphorylates and regulates Pdcd4 tumor suppressor protein. Cancer Res. *65*, 11282–11286.

Pan, D. (2010). The hippo signaling pathway in development and cancer. Dev. Cell *19*, 491–505.

Paquette, M., El-Houjeiri, L., and Pause, A. (2018). mTOR Pathways in Cancer and Autophagy. Cancers (Basel) *10*, 18.

Park, E.S., Kim, H., Suh, J.M., Park, S.J., You, S.H., Chung, H.K., Lee, K.W., Kwon, O.Y., Cho, B.Y., Kim, Y.K., et al. (2000). Involvement of JAK/STAT (Janus kinase/signal transducer and activator of transcription) in the thyrotropin signaling pathway. Mol. Endocrinol. *14*, 662–670.

Parker, L.L., and Piwnica-Worms, H. (1992). Inactivation of the p34cdc2-cyclin B complex by the human WEE1 tyrosine kinase. Science *257*, 1955–1957.

Parplys, A.C., Zhao, W., Sharma, N., Groesser, T., Liang, F., Maranon, D.G., Leung, S.G., Grundt, K., Dray, E., Idate, R., et al. (2015). NUCKS1 is a novel RAD51AP1 paralog important for homologous recombination and genome stability. Nucleic Acids Res. *43*, 9817–9834.

Patel, K.M., Strong, A., Tohyama, J., Jin, X., Morales, C.R., Billheimer, J., Millar, J., Kruth, H., and Rader, D.J. (2015). Macrophage sortilin promotes LDL uptake, foam cell formation, and atherosclerosis. Circ. Res. *116*, 789–796.

Patnaik, A., Haluska, P., Tolcher, A.W., Erlichman, C., Papadopoulos, K.P., Lensing, J.L., Beeram, M., Molina, J.R., Rasco, D.W., Arcos, R.R., et al. (2016). A First-in-Human Phase I Study of the Oral p38 MAPK Inhibitor, Ralimetinib (LY2228820 Dimesylate), in Patients with Advanced Cancer. Clin. Cancer Res. *22*, 1095–1102.

Pedersen, S.F., and Ho, Y.-C. (2020). SARS-CoV-2: a storm is raging. J. Clin. Invest. *130*, 2202–2205.

Peiris, J.S.M., Yuen, K.Y., Osterhaus, A.D.M.E., and Stöhr, K. (2003). The severe acute respiratory syndrome. N. Engl. J. Med. *349*, 2431–2441.

Peng, T.-Y., Lee, K.-R., and Tarn, W.-Y. (2008). Phosphorylation of the arginine/serine dipeptide-rich motif of the severe acute respiratory syndrome coronavirus nucleocapsid protein modulates its multimerization, translation inhibitory activity and cellular localization. FEBS J. *275*, 4152–4163.

Penzo, C., Arnoldo, L., Pegoraro, S., Petrosino, S., Ros, G., Zanin, R., Wiśniewski, J.R., Manfioletti, G., and Sgarra, R. (2019). HMGA1 Modulates Gene Transcription Sustaining a Tumor Signalling Pathway Acting on the Epigenetic Status of Triple-Negative Breast Cancer Cells. Cancers (Basel) *11*, 1105.

Perez-Riverol, Y., Csordas, A., Bai, J., Bernal-Llinares, M., Hewapathirana, S., Kundu, D.J., Inuganti, A., Griss, J., Mayer, G., Eisenacher, M., et al. (2019). The PRIDE database and related tools and resources in 2019: improving support for quantification data. Nucleic Acids Res. *47* (D1), D442–D450.

Pfeiffer, J.R., McAvoy, B.L., Fecteau, R.E., Deleault, K.M., and Brooks, S.A. (2011). CARHSP1 is required for effective tumor necrosis factor alpha mRNA stabilization and localizes to processing bodies and exosomes. Mol. Cell. Biol. *31*, 277–286.

Pires, E., Sung, P., and Wiese, C. (2017). Role of RAD51AP1 in homologous recombination DNA repair and carcinogenesis. DNA Repair (Amst.) *59*, 76–81.

Ponnam, S., Sevrieva, I., Sun, Y.-B., Irving, M., and Kampourakis, T. (2019). Site-specific phosphorylation of myosin binding protein-C coordinates thin and thick filament activation in cardiac muscle. Proc. Natl. Acad. Sci. USA *116*, 15485–15494.

Popov, D. (2012). Endoplasmic reticulum stress and the on site function of resident PTP1B. Biochem. Biophys. Res. Commun. *422*, 535–538.

Poppe, M., Wittig, S., Jurida, L., Bartkuhn, M., Wilhelm, J., Müller, H., Beuerlein, K., Karl, N., Bhuju, S., Ziebuhr, J., et al. (2017). The NF-κB-dependent and -independent transcriptome and chromatin landscapes of human coronavirus 229E-infected cells. PLoS Pathog. *13*, e1006286.

Porollo, A., and Meller, J. (2007). Prediction-based fingerprints of protein-protein interactions. Proteins *66*, 630–645.

Potter, C.J., Pedraza, L.G., and Xu, T. (2002). Akt regulates growth by directly phosphorylating Tsc2. Nat. Cell Biol. *4*, 658–665.

Potthoff, M.J., and Olson, E.N. (2007). MEF2: a central regulator of diverse developmental programs. Development *134*, 4131–4140.

Preisinger, C., Short, B., De Corte, V., Bruyneel, E., Haas, A., Kopajtich, R., Gettemans, J., and Barr, F.A. (2004). YSK1 is activated by the Golgi matrix protein GM130 and plays a role in cell migration through its substrate 14-3-3zeta. J. Cell Biol. *164*, 1009–1020.

Proteau, A., Blier, S., Albert, A.L., Lavoie, S.B., Traish, A.M., and Vincent, M. (2005). The multifunctional nuclear protein p54nrb is multiphosphorylated in mitosis and interacts with the mitotic regulator Pin1. J. Mol. Biol. *346*, 1163–1172.

Qiao, R., Weissmann, F., Yamaguchi, M., Brown, N.G., VanderLinden, R., Imre, R., Jarvis, M.A., Brunner, M.R., Davidson, I.F., Litos, G., et al. (2016). Mechanism of APC/CCDC20 activation by mitotic phosphorylation. Proc. Natl. Acad. Sci. USA *113*, E2570–E2578.

Qiu, Q., Jiang, J., Lin, L., Cheng, S., Xin, D., Jiang, W., Shen, J., and Hu, Z. (2016). Downregulation of RSK2 influences the biological activities of human osteosarcoma cells through inactivating AKT/mTOR signaling pathways. Int. J. Oncol. *48*, 2508–2520.

Quan, B., Seo, H.-S., Blobel, G., and Ren, Y. (2014). Vesiculoviral matrix (M) protein occupies nucleic acid binding site at nucleoporin pair (Rae1 ● Nup98). Proc. Natl. Acad. Sci. USA *111*, 9127–9132.

R Core Team. (2019). R: A language and environment for statistical computing (R Foundation for Statistical Computing).

Radic, V. (2016). A Novel Role for SCAMP3 as an Innate Immune Factor (UC Riverside).

Radtke, K., Döhner, K., and Sodeik, B. (2006). Viral interactions with the cytoskeleton: a hitchhiker's guide to the cell. Cell. Microbiol. *8*, 387–400.

Radulescu, A.E., and Cleveland, D.W. (2010). NuMA after 30 years: the matrix revisited. Trends Cell Biol. *20*, 214–222.

Rahim, M.N., Klewes, L., Zahedi-Amiri, A., Mai, S., and Coombs, K.M. (2018). Global Interactomics Connect Nuclear Mitotic Apparatus Protein NUMA1 to Influenza Virus Maturation. Viruses *10*, 731.

Rai, R., Hu, C., Broton, C., Chen, Y., Lei, M., and Chang, S. (2017). NBS1 Phosphorylation Status Dictates Repair Choice of Dysfunctional Telomeres. Mol. Cell *65*, 801–817.e4.

Ramm, G., Larance, M., Guilhaus, M., and James, D.E. (2006). A role for 14-3-3 in insulin-stimulated GLUT4 translocation through its interaction with the Rab-GAP AS160. J. Biol. Chem. *281*, 29174–29180.

Raught, B., Peiretti, F., Gingras, A.-C., Livingstone, M., Shahbazian, D., Mayeur, G.L., Polakiewicz, R.D., Sonenberg, N., and Hershey, J.W.B. (2004). Phosphorylation of eucaryotic translation initiation factor 4B Ser422 is modulated by S6 kinases. EMBO J. *23*, 1761–1769.

Ravichandran, L.V., Chen, H., Li, Y., and Quon, M.J. (2001). Phosphorylation of PTP1B at Ser(50) by Akt impairs its ability to dephosphorylate the insulin receptor. Mol. Endocrinol. *15*, 1768–1780.

Rebeaud, F., Hailfinger, S., Posevitz-Fejfar, A., Tapernoux, M., Moser, R., Rueda, D., Gaide, O., Guzzardi, M., Iancu, E.M., Rufer, N., et al. (2008). The proteolytic activity of the paracaspase MALT1 is key in T cell activation. Nat. Immunol. *9*, 272–281.

Renganathan, H., Vaidyanathan, H., Knapinska, A., and Ramos, J.W. (2005). Phosphorylation of PEA-15 switches its binding specificity from ERK/MAPK to FADD. Biochem. J. *390*, 729–735.

Revenko, A.S., Kalashnikova, E.V., Gemo, A.T., Zou, J.X., and Chen, H.-W. (2010). Chromatin loading of E2F-MLL complex by cancer-associated coregulator ANCCA via reading a specific histone mark. Mol. Cell. Biol. *30*, 5260–5272.

Riad, A., Zeng, C., Weng, C.-C., Winters, H., Xu, K., Makvandi, M., Metz, T., Carlin, S., and Mach, R.H. (2018). Sigma-2 Receptor/TMEM97 and PGRMC-1 Increase the Rate of Internalization of LDL by LDL Receptor through the Formation of a Ternary Complex. Sci. Rep. *8*, 16845.

Robinson, M., Schor, S., Barouch-Bentov, R., and Einav, S. (2018). Viral journeys on the intracellular highways. Cell. Mol. Life Sci. *75*, 3693–3714.

Robinson-White, A., and Stratakis, C.A. (2002). Protein kinase A signaling: "cross-talk" with other pathways in endocrine cells. Ann. N Y Acad. Sci. *968*, 256–270.

Robitaille, A.M., Christen, S., Shimobayashi, M., Cornu, M., Fava, L.L., Moes, S., Prescianotto-Baschong, C., Sauer, U., Jenoe, P., and Hall, M.N. (2013). Quantitative phosphoproteomics reveal mTORC1 activates de novo pyrimidine synthesis. Science *339*, 1320–1323.

Rogakou, E.P., Pilch, D.R., Orr, A.H., Ivanova, V.S., and Bonner, W.M. (1998). DNA double-stranded breaks induce histone H2AX phosphorylation on serine 139. J. Biol. Chem. *273*, 5858–5868.

Rogalla, T., Ehrnsperger, M., Preville, X., Kotlyarov, A., Lutsch, G., Ducasse, C., Paul, C., Wieske, M., Arrigo, A.P., Buchner, J., and Gaestel, M. (1999). Regulation of Hsp27 oligomerization, chaperone function, and protective activity against oxidative stress/tumor necrosis factor α by phosphorylation. J. Biol. Chem. *274*, 18947–18956.

Rogers, S., McCloy, R.A., Parker, B.L., Chaudhuri, R., Gayevskiy, V., Hoffman, N.J., Watkins, D.N., Daly, R.J., James, D.E., and Burgess, A. (2015). Dataset from the global phosphoproteomic mapping of early mitotic exit in human cells. Data Brief *5*, 45–52.

Rothe, C., Schunk, M., Sothmann, P., Bretzel, G., Froeschl, G., Wallrauch, C., Zimmer, T., Thiel, V., Janke, C., Guggemos, W., et al. (2020). Transmission of 2019-nCoV Infection from an Asymptomatic Contact in Germany. N. Engl. J. Med. *382*, 970–971.

Roy, R., Durie, D., Li, H., Liu, B.-Q., Skehel, J.M., Mauri, F., Cuorvo, L.V., Barbareschi, M., Guo, L., Holcik, M., et al. (2014). hnRNPA1 couples nuclear export and translation of specific mRNAs downstream of FGF-2/S6K2 signalling. Nucleic Acids Res. *42*, 12483–12497.

Roy, R., Huang, Y., Seckl, M.J., and Pardo, O.E. (2017). Emerging roles of hnRNPA1 in modulating malignant transformation. Wiley Interdiscip. Rev. RNA *8*.

Ryan, E.L., Hollingworth, R., and Grand, R.J. (2016). Activation of the DNA Damage Response by RNA Viruses. Biomolecules *6*, 2.

Salvi, M., Xu, D., Chen, Y., Cabrelle, A., Sarno, S., and Pinna, L.A. (2009). Programmed cell death protein 5 (PDCD5) is phosphorylated by CK2 in vitro and in 293T cells. Biochem. Biophys. Res. Commun. *387*, 606–610.

Sanborn, K.B., Mace, E.M., Rak, G.D., Difeo, A., Martignetti, J.A., Pecci, A., Bussel, J.B., Favier, R., and Orange, J.S. (2011). Phosphorylation of the myosin IIA tailpiece regulates single myosin IIA molecule association with lytic granules to promote NK-cell cytotoxicity. Blood *118*, 5862–5871.

Sánchez-Martín, P., and Komatsu, M. (2018). p62/SQSTM1 - steering the cell through health and disease. J. Cell Sci. *131*, jcs222836.

Santamaria, P.G., Finley, D., Ballesta, J.P.G., and Remacha, M. (2003). Rpn6p, a proteasome subunit from Saccharomyces cerevisiae, is essential for the assembly and activity of the 26 S proteasome. J. Biol. Chem. *278*, 6687–6695.

Saredi, A., Howard, L., and Compton, D.A. (1997). Phosphorylation regulates the assembly of NuMA in a mammalian mitotic extract. J. Cell Sci. *110*, 1287–1297.

Schmucker, S., and Sumara, I. (2014). Molecular dynamics of PLK1 during mitosis. Mol. Cell. Oncol. *1*, e954507.

Schweppe, D.K., Rigas, J.R., and Gerber, S.A. (2013). Quantitative phosphoproteomic profiling of human non-small cell lung cancer tumors. J. Proteomics *91*, 286–296.

Sengupta, S., Lorente-Rodríguez, A., Earnest, S., Stippec, S., Guo, X., Trudgian, D.C., Mirzaei, H., and Cobb, M.H. (2013). Regulation of OSR1 and the sodium, potassium, two chloride cotransporter by convergent signals. Proc. Natl. Acad. Sci. USA *110*, 18826–18831.

Serber, Z., and Ferrell, J.E., Jr. (2007). Tuning bulk electrostatics to regulate protein function. Cell *128*, 441–444.

Shah, P.S., Link, N., Jang, G.M., Sharp, P.P., Zhu, T., Swaney, D.L., Johnson, J.R., Von Dollen, J., Ramage, H.R., Satkamp, L., et al. (2018). Comparative Flavivirus-Host Protein Interaction Mapping Reveals Mechanisms of Dengue and Zika Virus Pathogenesis. Cell *175*, 1931–1945.e18.

Shahbazian, D., Roux, P.P., Mieulet, V., Cohen, M.S., Raught, B., Taunton, J., Hershey, J.W.B., Blenis, J., Pende, M., and Sonenberg, N. (2006). The mTOR/PI3K and MAPK pathways converge on eIF4B to control its phosphorylation and activity. EMBO J. *25*, 2781–2791.

Shandilya, J., Senapati, P., Dhanasekaran, K., Bangalore, S.S., Kumar, M., Kishore, A.H., Bhat, A., Kodaganur, G.S., and Kundu, T.K. (2014). Phosphorylation of multifunctional nucleolar protein nucleophosmin (NPM1) by aurora kinase B is critical for mitotic progression. FEBS Lett. *588*, 2198–2205.

Shang, J., Ye, G., Shi, K., Wan, Y., Luo, C., Aihara, H., Geng, Q., Auerbach, A., and Li, F. (2020). Structural basis of receptor recognition by SARS-CoV-2. Nature *581*, 221–224.

Sharma, K., Åkerström, S., Sharma, A.K., Chow, V.T.K., Teow, S., Abrenica, B., Booth, S.A., Booth, T.F., Mirazimi, A., and Lal, S.K. (2011). SARS-CoV 9b protein diffuses into nucleus, undergoes active Crm1 mediated nucleocytoplasmic export and triggers apoptosis when retained in the nucleus. PLoS ONE *6*, e19436.

Sharma, K., D'Souza, R.C.J., Tyanova, S., Schaab, C., Wiśniewski, J.R., Cox, J., and Mann, M. (2014). Ultradeep human phosphoproteome reveals a distinct regulatory nature of Tyr and Ser/Thr-based signaling. Cell Rep. *8*, 1583–1594.

Shi, J.-H., and Sun, S.-C. (2015). TCR signaling to NF-κB and mTORC1: Expanding roles of the CARMA1 complex. Mol. Immunol. *68* (2 Pt C), 546–557.

Shi, J., Zhang, T., Zhou, C., Chohan, M.O., Gu, X., Wegiel, J., Zhou, J., Hwang, Y.-W., Iqbal, K., Grundke-Iqbal, I., et al. (2008). Increased dosage of Dyrk1A alters alternative splicing factor (ASF)-regulated alternative splicing of tau in Down syndrome. J. Biol. Chem. *283*, 28660–28669.

Shih, M.-C., Chen, J.-Y., Wu, Y.-C., Jan, Y.-H., Yang, B.-M., Lu, P.-J., Cheng, H.-C., Huang, M.-S., Yang, C.-J., Hsiao, M., and Lai, J.M. (2012). TOPK/PBK promotes cell migration via modulation of the PI3K/PTEN/AKT pathway and is associated with poor prognosis in lung cancer. Oncogene *31*, 2389–2400.

Sinclair, A., Yarranton, S., and Schelcher, C. (2006). DNA-damage response pathways triggered by viral replication. Expert Rev. Mol. Med. *8*, 1–11.

Smith, G.A., and Enquist, L.W. (2002). Break ins and break outs: viral interactions with the cytoskeleton of Mammalian cells. Annu. Rev. Cell Dev. Biol. *18*, 135–161.

Smith, G.L., and Law, M. (2004). The exit of vaccinia virus from infected cells. Virus Res. *106*, 189–197.

Snyder, P.M., Olson, D.R., Kabra, R., Zhou, R., and Steines, J.C. (2004). cAMP and serum and glucocorticoid-inducible kinase (SGK) regulate the epithelial Na(+) channel through convergent phosphorylation of Nedd4-2. J. Biol. Chem. *279*, 45753–45758.

Stoilov, P., Daoud, R., Nayler, O., and Stamm, S. (2004). Human tra2-beta1 autoregulates its protein concentration by influencing alternative splicing of its pre-mRNA. Hum. Mol. Genet. *13*, 509–524.

Stokoe, D., Engel, K., Campbell, D.G., Cohen, P., and Gaestel, M. (1992). Identification of MAPKAP kinase 2 as a major enzyme responsible for the phosphorylation of the small mammalian heat shock proteins. FEBS Lett. *313*, 307–313.

Su, B., Cheng, J., Yang, J., and Guo, Z. (2001). MEKK2 is required for T-cell receptor signals in JNK activation and interleukin-2 gene expression. J. Biol. Chem. *276*, 14784–14790.

Subramanian, A., Tamayo, P., Mootha, V.K., Mukherjee, S., Ebert, B.L., Gillette, M.A., Paulovich, A., Pomeroy, S.L., Golub, T.R., Lander, E.S., and Mesirov, J.P. (2005). Gene set enrichment analysis: a knowledge-based approach for interpreting genome-wide expression profiles. Proc. Natl. Acad. Sci. USA *102*, 15545–15550.

Tacke, R., Tohyama, M., Ogawa, S., and Manley, J.L. (1998). Human Tra2 proteins are sequence-specific activators of pre-mRNA splicing. Cell *93*, 139–148.

Tafforeau, L., Chantier, T., Pradezynski, F., Pellet, J., Mangeot, P.E., Vidalain, P.-O., Andre, P., Rabourdin-Combe, C., and Lotteau, V. (2011). Generation and comprehensive analysis of an influenza virus polymerase cellular interaction network. J. Virol. *85*, 13010–13018.

Taggart, C., Cervantes-Laurean, D., Kim, G., McElvaney, N.G., Wehr, N., Moss, J., and Levine, R.L. (2000). Oxidation of either methionine 351 or methionine 358 in alpha 1-antitrypsin causes loss of anti-neutrophil elastase activity. J. Biol. Chem. *275*, 27258–27265.

Tan, Y.-J., Fielding, B.C., Goh, P.-Y., Shen, S., Tan, T.H.P., Lim, S.G., and Hong, W. (2004). Overexpression of 7a, a protein specifically encoded by the severe acute respiratory syndrome coronavirus, induces apoptosis via a caspase-dependent pathway. J. Virol. *78*, 14043–14047.

Tan, S.-X., Ng, Y., Burchfield, J.G., Ramm, G., Lambright, D.G., Stöckli, J., and James, D.E. (2012). The Rab GTPase-activating protein TBC1D4/AS160 contains an atypical phosphotyrosine-binding domain that interacts with plasma membrane phospholipids to facilitate GLUT4 trafficking in adipocytes. Mol. Cell. Biol. *32*, 4946–4959.

Tanenbaum, M.E., Galjart, N., van Vugt, M.A.T.M., and Medema, R.H. (2006). CLIP-170 facilitates the formation of kinetochore-microtubule attachments. EMBO J. *25*, 45–57.

Tantos, A., Szrnka, K., Szabo, B., Bokor, M., Kamasa, P., Matus, P., Bekesi, A., Tompa, K., Han, K.-H., and Tompa, P. (2013). Structural disorder and local order of hNopp140. Biochim. Biophys. Acta *1834*, 342–350.

Tarakhovsky, A., and Prinjha, R.K. (2018). Drawing on disorder: How viruses use histone mimicry to their advantage. J. Exp. Med. *215*, 1777–1787.

Tavares, M.R., Pavan, I.C.B., Amaral, C.L., Meneguello, L., Luchessi, A.D., and Simabuco, F.M. (2015). The S6K protein family in health and disease. Life Sci. *131*, 1–10.

Taylor, M.P., Koyuncu, O.O., and Enquist, L.W. (2011). Subversion of the actin cytoskeleton during viral infection. Nat. Rev. Microbiol. *9*, 427–439.

Tee, A.R., Fingar, D.C., Manning, B.D., Kwiatkowski, D.J., Cantley, L.C., and Blenis, J. (2002). Tuberous sclerosis complex-1 and -2 gene products function together to inhibit mammalian target of rapamycin (mTOR)-mediated downstream signaling. Proc. Natl. Acad. Sci. USA *99*, 13571–13576.

Thaker, S.K., Ch'ng, J., and Christofk, H.R. (2019). Viral hijacking of cellular metabolism. BMC Biol. *17*, 59.

Thejer, B.M., Adhikary, P.P., Kaur, A., Teakel, S.L., Van Oosterum, A., Seth, I., Pajic, M., Hannan, K.M., Pavy, M., Poh, P., et al. (2020). PGRMC1 phosphorylation affects cell shape, motility, glycolysis, mitochondrial form and function, and tumor growth. BMC Mol. Cell Biol. *21*, 24.

Tiedje, C., Lubas, M., Tehrani, M., Menon, M.B., Ronkina, N., Rousseau, S., Cohen, P., Kotlyarov, A., and Gaestel, M. (2015). p38MAPK/MK2-mediated phosphorylation of RBM7 regulates the human nuclear exosome targeting complex. RNA *21*, 262–278.

Tokuyama, Y., Horn, H.F., Kawamura, K., Tarapore, P., and Fukasawa, K. (2001). Specific phosphorylation of nucleophosmin on Thr(199) by cyclin-dependent kinase 2-cyclin E and its role in centrosome duplication. J. Biol. Chem. *276*, 21529–21537.

Toughiri, R., Li, X., Du, Q., and Bieberich, C.J. (2013). Phosphorylation of NuMA by Aurora-A kinase in PC-3 prostate cancer cells affects proliferation, survival, and interphase NuMA localization. J. Cell. Biochem. *114*, 823–830.

Trencia, A., Perfetti, A., Cassese, A., Vigliotta, G., Miele, C., Oriente, F., Santopietro, S., Giacco, F., Condorelli, G., Formisano, P., and Beguinot, F. (2003). Protein kinase B/Akt binds and phosphorylates PED/PEA-15, stabilizing its antiapoptotic action. Mol. Cell. Biol. *23*, 4511–4521.

Trigg, B.J., and Ferguson, B.J. (2015). Functions of DNA damage machinery in the innate immune response to DNA virus infection. Curr. Opin. Virol. *15*, 56–62.

Tsai, S.-C., and Seto, E. (2002). Regulation of histone deacetylase 2 by protein kinase CK2. J. Biol. Chem. *277*, 31826–31833.

Tsai, L.-H., Lees, E., Faha, B., Harlow, E., and Riabowol, K. (1993). The cdk2 kinase is required for the G1-to-S transition in mammalian cells. Oncogene *8*, 1593–1602.

Tsoi, H., Li, L., Chen, Z.S., Lau, K.-F., Tsui, S.K.W., and Chan, H.Y.E. (2014). The SARS-coronavirus membrane protein induces apoptosis via interfering with PDK1-PKB/Akt signalling. Biochem. J. *464*, 439–447.

Tsvetkov, L., and Stern, D.F. (2005). Phosphorylation of Plk1 at S137 and T210 is inhibited in response to DNA damage. Cell Cycle *4*, 166–171.

Ui, A., Nagaura, Y., and Yasui, A. (2015). Transcriptional elongation factor ENL phosphorylated by ATM recruits polycomb and switches off transcription for DSB repair. Mol. Cell *58*, 468–482.

Ujike, M., and Taguchi, F. (2015). Incorporation of spike and membrane glycoproteins into coronavirus virions. Viruses *7*, 1700–1725.

Valvezan, A.J., and Klein, P.S. (2012). GSK-3 and Wnt Signaling in Neurogenesis and Bipolar Disorder. Front. Mol. Neurosci. *5*, 1.

Vind, B.F., Pehmøller, C., Treebak, J.T., Birk, J.B., Hey-Mogensen, M., Beck-Nielsen, H., Zierath, J.R., Wojtaszewski, J.F.P., and Højlund, K. (2011). Impaired insulin-induced site-specific phosphorylation of TBC1 domain family, member 4 (TBC1D4) in skeletal muscle of type 2 diabetes patients is restored by endurance exercise-training. Diabetologia *54*, 157–167.

Vishwanatha, J.K., and Kumble, S. (1993). Involvement of annexin II in DNA replication: evidence from cell-free extracts of Xenopus eggs. J. Cell Sci. *105*, 533–540.

Wada, T., Nakagawa, K., Watanabe, T., Nishitai, G., Seo, J., Kishimoto, H., Kitagawa, D., Sasaki, T., Penninger, J.M., Nishina, H., and Katada, T. (2001). Impaired synergistic activation of stress-activated protein kinase SAPK/JNK in mouse embryonic stem cells lacking SEK1/MKK4: different contribution of SEK2/MKK7 isoforms to the synergistic activation. J. Biol. Chem. *276*, 30892–30897.

Walsh, D., and Mohr, I. (2011). Viral subversion of the host protein synthesis machinery. Nat. Rev. Microbiol. *9*, 860–875.

Walter, B.L., Parsley, T.B., Ehrenfeld, E., and Semler, B.L. (2002). Distinct poly(rC) binding protein KH domain determinants for poliovirus translation initiation and viral RNA replication. J. Virol. *76*, 12008–12022.

Walter, D., Hoffmann, S., Komseli, E.-S., Rappsilber, J., Gorgoulis, V., and Sørensen, C.S. (2016). SCF(Cyclin F)-dependent degradation of CDC6 suppresses DNA re-replication. Nat. Commun. *7*, 10530.

Wang, Y., and Prives, C. (1995). Increased and altered DNA binding of human p53 by S and G2/M but not G1 cyclin-dependent kinases. Nature *376*, 88–91.

Wang, Y., and Zhang, X. (1999). The nucleocapsid protein of coronavirus mouse hepatitis virus interacts with the cellular heterogeneous nuclear ribonucleoprotein A1 in vitro and in vivo. Virology 265, 96–109.

Wang, A.H., Kruhlak, M.J., Wu, J., Bertos, N.R., Vezmar, M., Posner, B.I., Bazett-Jones, D.P., and Yang, X.J. (2000). Regulation of histone deacetylase 4 by binding of 14-3-3 proteins. Mol. Cell. Biol. 20, 6904–6912.

Wang, W., Ye, L., Ye, L., Li, B., Gao, B., Zeng, Y., Kong, L., Fang, X., Zheng, H., Wu, Z., and She, Y. (2007). Up-regulation of IL-6 and TNF-alpha induced by SARS-coronavirus spike protein in murine macrophages via NF-kappaB pathway. Virus Res. 128, 1–8.

Wang, L., Harris, T.E., and Lawrence, J.C., Jr. (2008). Regulation of proline-rich Akt substrate of 40 kDa (PRAS40) function by mammalian target of rapamycin complex 1 (mTORC1)-mediated phosphorylation. J. Biol. Chem. 283, 15619–15627.

Wang, T., Cleary, R.A., Wang, R., and Tang, D.D. (2013). Role of the adapter protein Abi1 in actin-associated signaling and smooth muscle contraction. J. Biol. Chem. 288, 20713–20722.

Wang, Z., Lu, W., Zhang, Y., Zou, F., Jin, Z., and Zhao, T. (2020). The Hippo Pathway and Viral Infections. Front. Microbiol. 10, 3033.

Ward, Y., Spinelli, B., Quon, M.J., Chen, H., Ikeda, S.R., and Kelly, K. (2004). Phosphorylation of critical serine residues in Gem separates cytoskeletal reorganization from down-regulation of calcium channel activity. Mol. Cell. Biol. 24, 651–661.

Wen, Z., Zhong, Z., and Darnell, J.E., Jr. (1995). Maximal activation of transcription by Stat1 and Stat3 requires both tyrosine and serine phosphorylation. Cell 82, 241–250.

Wen, A.Y., Sakamoto, K.M., and Miller, L.S. (2010). The role of the transcription factor CREB in immune function. J. Immunol. 185, 6413–6419.

Wertz, I.E., Newton, K., Seshasayee, D., Kusam, S., Lam, C., Zhang, J., Popovych, N., Helgason, E., Schoeffler, A., Jeet, S., et al. (2015). Phosphorylation and linear ubiquitin direct A20 inhibition of inflammation. Nature 528, 370–375.

Willems, A.R., Lanker, S., Patton, E.E., Craig, K.L., Nason, T.F., Mathias, N., Kobayashi, R., Wittenberg, C., and Tyers, M. (1996). Cdc53 targets phosphorylated G1 cyclins for degradation by the ubiquitin proteolytic pathway. Cell 86, 453–463.

Williams, R.S., Shohet, R.V., and Stillman, B. (1997). A human protein related to yeast Cdc6p. Proc. Natl. Acad. Sci. USA 94, 142–147.

Wohlbold, L., Merrick, K.A., De, S., Amat, R., Kim, J.H., Larochelle, S., Allen, J.J., Zhang, C., Shokat, K.M., Petrini, J.H.J., and Fisher, R.P. (2012). Chemical genetics reveals a specific requirement for Cdk2 activity in the DNA damage response and identifies Nbs1 as a Cdk2 substrate in human cells. PLoS Genet. 8, e1002935.

Wolin, S.L., and Cedervall, T. (2002). The La protein. Annu. Rev. Biochem. 71, 375–403.

Wong, C.K., Lam, C.W.K., Wu, A.K.L., Ip, W.K., Lee, N.L.S., Chan, I.H.S., Lit, L.C.W., Hui, D.S.C., Chan, M.H.M., Chung, S.S.C., and Sung, J.J. (2004). Plasma inflammatory cytokines and chemokines in severe acute respiratory syndrome. Clin. Exp. Immunol. 136, 95–103.

Wortzel, I., and Seger, R. (2011). The ERK Cascade: Distinct Functions within Various Subcellular Organelles. Genes Cancer 2, 195–209.

Wu, C.-H., Yeh, S.-H., Tsay, Y.-G., Shieh, Y.-H., Kao, C.-L., Chen, Y.-S., Wang, S.-H., Kuo, T.-J., Chen, D.-S., and Chen, P.-J. (2009). Glycogen synthase kinase-3 regulates the phosphorylation of severe acute respiratory syndrome coronavirus nucleocapsid protein and viral replication. J. Biol. Chem. 284, 5229–5239.

Wu, X., Renuse, S., Sahasrabuddhe, N.A., Zahari, M.S., Chaerkady, R., Kim, M.-S., Nirujogi, R.S., Mohseni, M., Kumar, P., Raju, R., et al. (2014). Activation of diverse signalling pathways by oncogenic PIK3CA mutations. Nat. Commun. 5, 4961.

Wu, H., Deng, W.-W., Yang, L.-L., Zhang, W.-F., and Sun, Z.-J. (2018). Expression and phosphorylation of Stathmin 1 indicate poor survival in head and neck squamous cell carcinoma and associate with immune suppression. Biomarkers Med. 12, 759–769.

Wurm, T., Chen, H., Hodgson, T., Britton, P., Brooks, G., and Hiscox, J.A. (2001). Localization to the nucleolus is a common feature of coronavirus nucleoproteins, and the protein may disrupt host cell division. J. Virol. 75, 9345–9356.

Xu, L.H., Huang, M., Fang, S.G., and Liu, D.X. (2011). Coronavirus infection induces DNA replication stress partly through interaction of its nonstructural protein 13 with the p125 subunit of DNA polymerase δ. J. Biol. Chem. 286, 39546–39559.

Yang, P., Guo, L., Duan, Z.J., Tepper, C.G., Xue, L., Chen, X., Kung, H.-J., Gao, A.C., Zou, J.X., and Chen, H.-W. (2012a). Histone methyltransferase NSD2/MMSET mediates constitutive NF-κB signaling for cancer cell proliferation, survival, and tumor growth via a feed-forward loop. Mol. Cell. Biol. 32, 3121–3131.

Yang, W., Zheng, Y., Xia, Y., Ji, H., Chen, X., Guo, F., Lyssiotis, C.A., Aldape, K., Cantley, L.C., and Lu, Z. (2012b). ERK1/2-dependent phosphorylation and nuclear translocation of PKM2 promotes the Warburg effect. Nat. Cell Biol. 14, 1295–1304.

Yang, W., Xia, Y., Hawke, D., Li, X., Liang, J., Xing, D., Aldape, K., Hunter, T., Yung, W.K.A., and Lu, Z. (2014). PKM2 Phosphorylates Histone H3 and Promotes Gene Transcription and Tumorigenesis. Cell 158, 1210.

Yao, K., Peng, C., Zhang, Y., Zykova, T.A., Lee, M.-H., Lee, S.-Y., Rao, E., Chen, H., Ryu, J., Wang, L., et al. (2017). RSK2 phosphorylates T-bet to attenuate colon cancer metastasis and growth. Proc. Natl. Acad. Sci. USA 114, 12791–12796.

Ye, Z., Wong, C.K., Li, P., and Xie, Y. (2008). A SARS-CoV protein, ORF-6, induces caspase-3 mediated, ER stress and JNK-dependent apoptosis. Biochim. Biophys. Acta 1780, 1383–1387.

Yee, A.S., Paulson, E.K., McDevitt, M.A., Rieger-Christ, K., Summerhayes, I., Berasi, S.P., Kim, J., Huang, C.-Y., and Zhang, X. (2004). The HBP1 transcriptional repressor and the p38 MAP kinase: unlikely partners in G1 regulation and tumor suppression. Gene 336, 1–13.

Yim, H., Park, J.-W., Woo, S.U., Kim, S.-T., Liu, L., Lee, C.-H., and Lee, S.K. (2013). Phosphorylation of Cdc6 at serine 74, but not at serine 106, drives translocation of Cdc6 to the cytoplasm. J. Cell. Physiol. 228, 1221–1228.

Yoo, S.-M., Lee, C.-J., An, H.-J., Lee, J.Y., Lee, H.S., Kang, H.C., Cho, S.-J., Kim, S.-M., Park, J., Kim, D.J., and Cho, Y.Y. (2019). RSK2-Mediated ELK3 Activation Enhances Cell Transformation and Breast Cancer Cell Growth by Regulation of c-fos Promoter Activity. Int. J. Mol. Sci. 20, 1994.

Yu, W., Ding, X., Chen, F., Liu, M., Shen, S., Gu, X., and Yu, L. (2009). The phosphorylation of SEPT2 on Ser218 by casein kinase 2 is important to hepatoma carcinoma cell proliferation. Mol. Cell. Biochem. 325, 61–67.

Yu, Y., Yoon, S.-O., Poulogiannis, G., Yang, Q., Ma, X.M., Villén, J., Kubica, N., Hoffman, G.R., Cantley, L.C., Gygi, S.P., and Blenis, J. (2011). Phosphoproteomic analysis identifies Grb10 as an mTORC1 substrate that negatively regulates insulin signaling. Science 332, 1322–1326.

Yu, G., Wang, L.-G., Han, Y., and He, Q.-Y. (2012). clusterProfiler: an R package for comparing biological themes among gene clusters. OMICS 16, 284–287.

Yui, D., Yoneda, T., Oono, K., Katayama, T., Imaizumi, K., and Tohyama, M. (2001). Interchangeable binding of Bcl10 to TRAF2 and cIAPs regulates apoptosis signaling. Oncogene 20, 4317–4323.

Zhang, Y., Sun, Z.W., Iratni, R., Erdjument-Bromage, H., Tempst, P., Hampsey, M., and Reinberg, D. (1998). SAP30, a novel protein conserved between human and yeast, is a component of a histone deacetylase complex. Mol. Cell 1, 1021–1031.

Zhang, H.H., Huang, J., Düvel, K., Boback, B., Wu, S., Squillace, R.M., Wu, C.-L., and Manning, B.D. (2009). Insulin stimulates adipogenesis through the Akt-TSC2-mTORC1 pathway. PLoS ONE 4, e6189.

Zhang, H., Diab, A., Fan, H., Mani, S.K.K., Hullinger, R., Merle, P., and Andrisani, O. (2015). PLK1 and HOTAIR Accelerate Proteasomal Degradation of SUZ12 and ZNF198 during Hepatitis B Virus-Induced Liver Carcinogenesis. Cancer Res. 75, 2363–2374.

Zhang, H., Wang, A., Tan, Y., Wang, S., Ma, Q., Chen, X., and He, Z. (2019a). NCBP1 promotes the development of lung adenocarcinoma through up-regulation of CUL4B. J. Cell. Mol. Med. 23, 6965–6977.

Zhang, Q., Sharma, N.R., Zheng, Z.-M., and Chen, M. (2019b). Viral Regulation of RNA Granules in Infected Cells. Virol. Sin. 34, 175–191.

Zhang, B., Zhou, X., Qiu, Y., Feng, F., Feng, J., Jia, Y., Zhu, H., Hu, K., Liu, J., Liu, Z., et al. (2020). Clinical characteristics of 82 death cases with COVID-19. medRxiv. https://doi.org/10.1101/2020.02.26.20028191.

Zhao, J., He, S., Minassian, A., Li, J., and Feng, P. (2015). Recent advances on viral manipulation of NF-κB signaling pathway. Curr. Opin. Virol. 15, 103–111.

Zhou, Q., Wang, H., Schwartz, D.M., Stoffels, M., Park, Y.H., Zhang, Y., Yang, D., Demirkaya, E., Takeuchi, M., Tsai, W.L., et al. (2016). Loss-of-function mutations in TNFAIP3 leading to A20 haploinsufficiency cause an early-onset autoinflammatory disease. Nat. Genet. 48, 67–73.

Zhou, P., Yang, X.-L., Wang, X.-G., Hu, B., Zhang, L., Zhang, W., Si, H.-R., Zhu, Y., Li, B., Huang, C.-L., et al. (2020). A pneumonia outbreak associated with a new coronavirus of probable bat origin. Nature 579, 270–273.

Zhu, Y., Doray, B., Poussu, A., Lehto, V.P., and Kornfeld, S. (2001). Binding of GGA2 to the lysosomal enzyme sorting motif of the mannose 6-phosphate receptor. Science 292, 1716–1718.

Zhu, G., Qiu, W., Li, Y., Zhao, C., He, F., Zhou, M., Wang, L., Zhao, D., Lu, Y., Zhang, J., et al. (2017). Sublytic C5b-9 Induces Glomerular Mesangial Cell Apoptosis through the Cascade Pathway of MEKK2-p38 MAPK-IRF-1-TRADD-Caspase 8 in Rat Thy-1 Nephritis. J. Immunol. 198, 1104–1118.

Zou, J.X., Revenko, A.S., Li, L.B., Gemo, A.T., and Chen, H.-W. (2007). ANCCA, an estrogen-regulated AAA+ ATPase coactivator for ERalpha, is required for coregulator occupancy and chromatin modification. Proc. Natl. Acad. Sci. USA 104, 18067–18072.

Zuo, P., and Manley, J.L. (1993). Functional domains of the human splicing factor ASF/SF2. EMBO J. 12, 4727–4737.

STAR★METHODS

KEY RESOURCES TABLE

REAGENT or RESOURCE	SOURCE	IDENTIFIER
Antibodies		
Phospho-p38 MAPK (Thr180/Tyr182)	Cell Signaling	Cat#9211S
α-Rabbit IgG HRP Conjugate	Biorad	Cat#1706515
α-Mouse IgG HRP Conjugate	Biorad	Cat#1706516
SARS-CoV-2 N (recombinant mouse monoclonal)	Donated from the laboratory of Thomas Moran (Mount Sinai)	N/A
GAPDH	Cell Signaling	Cat#2118S
Phospho-MAPKAPK2 (T334)	Cell Signaling	Cat#3007T
Phospho-CREB/ATF-1 (S133)	Cell Signaling	Cat#9198S
CK2α	Abcam	Cat#ab70774
SARS-CoV membrane (M)	Rockland	Cat#100-401-A55
SARS-CoV nucleocapsid (N)	Rockland	Cat#200-401-A50
AF568-labeled goat-anti-rabbit	InvitrogenCat#	Cat#A11011
AF647-labeled goat-anti-mouse	Invitrogen	Cat#A21235
AF488-labeled Phalloidin	Hypermol	Cat#8813-01
viral NP protein anti-sera	produced in the Garcia-Sastre lab	N/A
Bacterial and Virus Strains		
SARS-CoV-2, isolate BetaCoV/France/IDF0372/2020	European Virus Archive goes Global (EVAg)	IDF0372/2020
SARS-CoV-2, isolate USA-WA1/2020	BEI Resources	Cat#NR-52281
SARS-CoV-2, Isolate Muc-IMB-1/2020	Bundeswehr Institute of Microbiology, Munich, Germany	N/A
Chemicals, Peptides, and Recombinant Proteins		
cOmplete protease inhibitor cocktail tablets mini, EDTA-free	Roche	Cat#11846170001
PhosStop phosphatase inhibitor cocktail tablets	Roche	Cat#4906837001
Sep-Pak C18 cartridge	Waters	Cat#WAT054955
Sequencing-grade modified trypsin	Promega	Cat#V5111
Fetal bovine serum (FBS)	Thermo Fisher Scientific	Cat#10082
DMEM	Thermo Fisher Scientific	Cat#MT10013CV
Water, HPLC grade	Sigma-Aldrich	Cat#270733-4 L; CAS#7732-18-5
Ni-NTA Superflow beads	QIAGEN	Cat#30210
Igepal	Sigma-Aldrich	Cat#I3021; CAS#9002-93-1
Minimal Essential Media (MEM)	Corning	Cat#10-009-CV
Opti-MEM	Thermo Fisher Scientific	Cat#31985062
Paraformaldehyde, 4% solution in PBS (PFA)	Thermo Scientific	Cat#MFCD00133991
Formalin	Fisher Scientific	Cat#SF100-20; CAS#50-00-0, 67-56-1, 7558-79-4, 10049-21-5, 7732-18-5
4′,6-diamidino-2-phenylindole (DAPI)	Thermo Scientific	Cat#62247
ReprosilPur 1.9 μm particles	ESI SOURCE SOLUTIONS	Cat#R119
Crystal Violet Solution	Sigma Aldrich	Cat#HT90132-1L
Thermanox coverslips	Ted Pella	Cat#26028
Silicon Chips	Ted Pella	Cat#16007

(Continued on next page)

Continued

REAGENT or RESOURCE	SOURCE	IDENTIFIER
Aluminum specimen mounts	Ted Pella	Cat#16111
Double-sided carbon tape	Ted Pella	Cat#16084-1
Karnovsky's EM fixative	Electron Microscopy Sciences	Cat#15720
Sodium Cacodylate	Sigma	Cat#C4945-10G; CAS#6131-99-3
Osmium Tetroxide	Electron Microscopy Sciences	Cat#19190; CAS#20816-12-0
Potassium Ferrocyanide	Sigma	Cat#P-3289; CAS#14459-95-1
Uranyl Acetate	Ted Pella	Cat#19481; CAS#6159-44-0
Spurr's resin	Ted Pella	Cat#18300-4221
Iridium target	Electron Microscopy Sciences	Cat#3431
PolyJet	SignaGen	Cat#SL100688
SuperScript IV Reverse Transcriptase	Invitrogen	Cat#18090010
ARRY-371797 (ARRY-797)	MedKoo Biosciences	Cat#555466; CAS#1036404-17-7
Dilmapimod (SB-681323)	MedChemExpress	Cat#HY-10404; CAS#444606-18-2
Doramapimod (BIRB-796)	SelleckChem	Cat#S1574; CAS#285983-48-4
Losmapimod	SelleckChem	Cat#S7215; CAS#585543-15-3
MAPK13-IN-1	MedChemExpress	Cat#HY-18850; CAS#229002-10-2
Neflamapimod (VX-745)	SelleckChem	Cat#S1458; CAS#209410-46-8
P38 MAPK Inhibitor (4)	Cayman Chemical	Cat#22219; CAS#1638-41-1
PF-3644022	Tocris Bioscience	Cat#4483; CAS#142557-61-7
PH-797804	SelleckChem	Cat#S2726; CAS#586379-66-0
Ralimetinib (LY2228820)	SelleckChem	Cat#S1494; CAS#862507-23-1
SB203580	SelleckChem	Cat#S1076; CAS#152121-47-6
TAK-715	SelleckChem	Cat#S2928; CAS#303162-79-0
Talmapimod (SCIO-469)	MedChemExpress	Cat#HY-10406; CAS#309913-83-5
VX-702	SelleckChem	Cat#S6005; CAS#745833-23-2
4EGI-1	SelleckChem	Cat#S7369; CAS#315706-13-9
A-484954	Tocris Bioscience	Cat#4279; CAS#1276121-88-0
Abemaciclib mesylate	SelleckChem	Cat#S7158; CAS#1231930-82-7
Alisertib	SelleckChem	Cat#S1133; CAS#1028486-01-2
Apilimod	SelleckChem	Cat#S6414; CAS#541550-19-0
AT-13148	SelleckChem	Cat#S7563; CAS#1056901-62-2
AZD-1208	SelleckChem	Cat#S7104; CAS#1204144-28-4
AZD-5363 (Capivasertib)	SelleckChem	Cat#S8019; CAS#1143532-39-1
AZD-7648	SelleckChem	Cat#S8843; CAS#2230820-11-6
Bafetinib	SelleckChem	Cat#S1369; CAS#859212-16-1
BMS-582949	SelleckChem	Cat#S8124; CAS#623152-17-0
Bortezomib (PS-341)	SelleckChem	Cat#S1013; CAS#179324-69-7
CHIR-98014	SelleckChem	Cat#S2745; CAS#252935-94-7
Dabrafenib (GSK2118436)	SelleckChem	Cat#S2807; CAS#1195765-45-7
Dasatinib	SelleckChem	Cat#S1021; CAS#302962-49-8
Dinaciclib	SelleckChem	Cat#S2768; CAS#779353-01-4
Dorsomorphin 2HCl	SelleckChem	Cat#S7306; CAS#1219168-18-9
EHT 1864 2HCl	SelleckChem	Cat#S7482; CAS#754240-09-0
Enzastaurin	SelleckChem	Cat#S1055; CAS#170364-57-5
Fludarabine	SelleckChem	Cat#S1491; CAS#S1491
Fosbretabulin (Combretastatin A4 Phosphate (CA4P)) Disodium	SelleckChem	Cat#S7204; CAS#168555-66-6
Ganetespib	SelleckChem	Cat#S1159; CAS#888216-25-9

Continued

REAGENT or RESOURCE	SOURCE	IDENTIFIER
Gilteritinib	SelleckChem	Cat#S7754; CAS#1254053-43-4
Idarubicin HCl	SelleckChem	Cat#S1228; CAS#57852-57-0
Ipatasertib	SelleckChem	Cat#S2808; CAS#1001264-89-6
Ispinesib (SB-715992)	SelleckChem	Cat#S1452; CAS#336113-53-2
Ixazomib (MLN2238)	SelleckChem	Cat#S2180; CAS#1072833-77-2
K-252a	Cayman Chemical	Cat#11338; CAS#99533-80-9
KenPaullone	SelleckChem	Cat#S7917; CAS#142273-20-9
KW-2449	SelleckChem	Cat#S2158; CAS#1000669-72-6
LJI308	SelleckChem	Cat#S7871; CAS#1627709-94-7
LMK-235	SelleckChem	Cat#S7569; CAS#1418033-25-6
LY2584702 Tosylate	SelleckChem	Cat#S7704; CAS#1082949-68-5
MBQ-167	SelleckChem	Cat#S8749; CAS#2097938-73-1
Mdivi-1	SelleckChem	Cat#S7162; CAS#338967-87-6
Midostaurin	SelleckChem	Cat#S8064; CAS#120685-11-2
MK-2206 2HCl	SelleckChem	Cat#S1078; CAS#1032350-13-2
ML141	SelleckChem	Cat#S7686; CAS#71203-35-5
NSC319276	SelleckChem	Cat#S7149; CAS#71555-25-4
NVP-BEP800	SelleckChem	Cat#S1498; CAS#847559-80-2
Palbociclib (PD-0332991) HCl	SelleckChem	Cat#S1116; CAS#827022-32-2
PF-03814735	SelleckChem	Cat#S2725; CAS#942487-16-3
PF-3758309	SelleckChem	Cat#S7094; CAS#898044-15-0
PHA-793887	SelleckChem	Cat#S1487; CAS#718630-59-2
Pictilisib	SelleckChem	Cat#S1065; CAS#957054-30-7
PKR Inhibitor	Cayman Chemical	Cat#15323; CAS#608512-97-6
QNZ (EVP4593)	SelleckChem	Cat#S4902; CAS#545380-34-5
R-406	SelleckChem	Cat#S2194; CAS#841290-81-1
R-547	SelleckChem	Cat#S2688; CAS#741713-40-6
Rapamycin	SelleckChem	Cat#S1039; CAS#53123-88-9
Ravoxertinib	SelleckChem	Cat#S7554; CAS#1453848-26-4
Remdesivir	BioVision	Cat#B2997; CAS#1809249-37-3
Ripasudil (K-115) hydrochloride dihydrate	SelleckChem	Cat#S7995; CAS#887375-67-9
Romidepsin (FK228, Depsipeptide)	SelleckChem	Cat#S3020; CAS#128517-07-7
Ruboxistaurin HCl(LY333531)	SelleckChem	Cat#S7663; CAS#169939-93-9
Sapanisertib	SelleckChem	Cat#S2811; CAS#1224844-38-5
SAR-407899	Cayman Chemical	Cat#21717; CAS#923359-38-0
SB743921 HCl	SelleckChem	Cat#S2182; CAS#940929-33-9
SGI-1776 free base	SelleckChem	Cat#S2198; CAS#1025065-69-3
Silmitasertib	SelleckChem	Cat#S2248; CAS#1009820-21-6
Sorafenib Tosylate	SelleckChem	Cat#S1040; CAS#475207-59-1
Sotrastaurin	SelleckChem	Cat#S2791; CAS#425637-18-9
Stattic	SelleckChem	Cat#S7024; CAS#19983-44-9
Staurosporine	SelleckChem	Cat#S1421; CAS#62996-74-1
Tanzisertib	SelleckChem	Cat#S8490; CAS#899805-25-5(freebase)
Tasquinimod	SelleckChem	Cat#S7617; CAS#254964-60-8
THZ1 2HCl	SelleckChem	Cat#S7549; CAS#1604810-83-4(freebase)
Tpl2 Kinase Inhibitor 1	Cayman Chemical	Cat#19710; CAS#871307-18-5
U73122	SelleckChem	Cat#S8011; CAS#112648-68-7
Volasertib	SelleckChem	Cat#S2235; CAS#755038-65-4

(Continued on next page)

Continued

REAGENT or RESOURCE	SOURCE	IDENTIFIER
XL413 (BMS-863233)	SelleckChem	Cat#S7547; CAS#1169562-71-3
Y-39983 HCl	SelleckChem	Cat#S7935; CAS#173897-44-4
CCL2/MCP-1, Capture Antibody	R&D Systems	Cat#MAB679
CCL5/RANTES, Capture Antibody	R&D Systems	Cat#MAB678
CCL11/Eotaxin, Capture Antibody	R&D Systems	Cat#MAB320
GM-CSF, Capture Antibody	R&D Systems	Cat#MAB615
IL-1RA, Capture Antibody	Peprotech	Cat#500-P209
CCL13/MCP-4, Capture Antibody	R&D Systems	Cat#MAB327
IL-4, Capture Antibody	R&D Systems	Cat#MAB604
IL-10, Capture Antibody	Peprotech	Cat#500-P20
IL-15, Capture Antibody	R&D Systems	Cat#MAB647
IL-1beta, Capture Antibody	R&D Systems	Cat#MAB601
CCL8/MCP-2, Capture Antibody	Peprotech	Cat#500-P35
CXCL9/MIG, Capture Antibody	Peprotech	Cat#500-P50
CCL3/MIP-1alpha, Capture Antibody	R&D Systems	Cat#MAB670
CXCL2/GRO-Beta, Capture Antibody	Peprotech	Cat#500-P104
TGF-Beta1, Capture Antibody	R&D Systems	Cat#MAB240
CXCL16, Capture Antibody	Peprotech	Cat#500-P200
CXCL8/IL-8, Capture Antibody	R&D Systems	Cat#MAB208
MMP-9, Capture Antibody	R&D Systems	Cat#MAB936
CXCL1/GRO-alpha, Capture Antibody	Peprotech	Cat#500-P92
IL-7, Capture Antibody	R&D Systems	Cat#MAB207
CCL4/MIP-1beta, Capture Antibody	R&D Systems	Cat#MAB271
IL-1alpha, Capture Antibody	R&D Systems	Cat#MAB200
IL-12 (p70), Capture Antibody	Peprotech	Cat#500-P154G
IL-16, Capture Antibody	R&D Systems	Cat#MAB316
CCL20/MIP-3a, Capture Antibody	R&D Systems	Cat#MAB360
TNF-alpha, Capture Antibody	R&D Systems	Cat#MAB610
Trappin-2/Elafin, Capture Antibody	R&D Systems	Cat#AF1747
IL-17A, Capture Antibody	R&D Systems	Cat#MAB317
CXCL10/IP-10, Capture Antibody	R&D Systems	Cat#MAB266
S100A8, Capture Antibody	R&D Systems	Cat#DS8900
IL-22, Capture Antibody	Peprotech	Cat#500-P211
CXCL5/ENA-78, Capture Antibody	R&D Systems	Cat#MAB654
IL-6, Capture Antibody	R&D Systems	Cat#MAB206
CCL7/MCP-3, Capture Antibody	R&D Systems	Cat#MAB282
CCL2/MCP-1, Protein std	R&D Systems	Cat#279-MC
CCL5/RANTES, Protein std	R&D Systems	Cat#278-RN
CCL11/Eotaxin, Protein std	Peprotech	Cat#300-21
GM-CSF, Protein std	R&D Systems	Cat#215-GM
IL-1RA, Protein std	Peprotech	Cat#200-01RA
CCL13/MCP-4, Protein std	R&D Systems	Cat#327-P4
IL-4, Protein std	R&D Systems	Cat#204-IL
IL-10, Protein std	Peprotech	Cat#200-10
IL-15, Protein std	R&D Systems	Cat#247-ILB
IL-1beta, Protein std	R&D Systems	Cat#201-LB
CCL8/MCP-2, Protein std	Peprotech	Cat#300-15
CXCL9/MIG, Protein std	R&D Systems	Cat#392-MG

Continued

REAGENT or RESOURCE	SOURCE	IDENTIFIER
CCL3/MIP-1alpha, Protein std	R&D Systems	Cat#270-LD
CXCL2/GRO-Beta, Protein std	Peprotech	Cat#300-39
TGF-Beta1, Protein std	Peprotech	Cat#100-21
CXCL16, Protein std	Peprotech	Cat#300-55
CXCL8/IL-8, Protein std	R&D Systems	Cat#208-IL
MMP-9, Protein std	R&D Systems	Cat#911-MP
CXCL1/GRO-alpha, Protein std	Peprotech	Cat#300-11
IL-7, Protein std	R&D Systems	Cat#207-IL
CCL4/MIP-1beta, Protein std	R&D Systems	Cat#271-BME
IL-1alpha, Protein std	Peprotech	Cat#200-01A
IL-12(p70), Protein std	R&D Systems	Cat#219-IL
IL-16, Protein std	Peprotech	Cat#200-16
CCL20/MIP-3a, Protein std	Peprotech	Cat#300-29A
TNF-alpha, Protein std	R&D Systems	Cat#210-TA
Trappin-2/Elafin, Protein std	R&D Systems	Cat#1747-PI
IL-17A, Protein std	Peprotech	Cat#200-17
CXCL10/IP-10, Protein std	R&D Systems	Cat#266-IP
S100A8, Protein std	R&D Systems	Cat#DS8900
IL-22, Protein std	Peprotech	Cat#200-22
CXCL5/ENA-78, Protein std	R&D Systems	Cat#254-XB
IL-6, Protein std	R&D Systems	Cat#206-IL
CCL7/MCP-3, Protein std	R&D Systems	Cat#282-P3
CCL2/MCP-1, Detection Antibody	R&D Systems	Cat#BAF279
CCL5/RANTES, Detection Antibody	R&D Systems	Cat#BAF278
CCL11/Eotaxin, Detection Antibody	R&D Systems	Cat#BAF320
GM-CSF, Detection Antibody	R&D Systems	Cat#BAM 215
IL-1RA, Detection Antibody	Peprotech	Cat#500-P209BT
CCL13/MCP-4, Detection Antibody	R&D Systems	Cat#BAF327
IL-4, Detection Antibody	R&D Systems	Cat#BAF204
IL-10, Detection Antibody	Peprotech	Cat#500-P20BT
IL-15, Detection Antibody	R&D Systems	Cat#BAM 247
IL-1beta, Detection Antibody	R&D Systems	Cat#BAF201
CCL8/MCP-2, Detection Antibody	Peprotech	Cat#500-P35BT
CXCL9/MIG, Detection Antibody	Peprotech	Cat#500-P50BT
CCL3/MIP-1alpha, Detection Antibody	R&D Systems	Cat#BAF270
CXCL2/GRO-Beta, Detection Antibody	Peprotech	Cat#500P104BT
TGF-Beta1, Detection Antibody	R&D Systems	Cat#BAM 2462
CXCL16, Detection Antibody	Peprotech	Cat#500-P200BT
CXCL8/IL-8, Detection Antibody	R&D Systems	Cat#BAF208
MMP-9, Detection Antibody	R&D Systems	Cat#BAF911
CXCL1/GRO-alpha, Detection Antibody	Peprotech	Cat#500P92BT
IL-7, Detection Antibody	R&D Systems	Cat#BAF207
CCL4/MIP-1beta, Detection Antibody	R&D Systems	Cat#BAF271
IL-1alpha, Detection Antibody	R&D Systems	Cat#BAF200
IL-12(p70), Detection Antibody	Peprotech	Cat#500-P154GBT
IL-16, Detection Antibody	R&D Systems	Cat#BAF316
CCL20/MIP-3a, Detection Antibody	R&D Systems	Cat#BAF360
TNF-alpha, Detection Antibody	R&D Systems	Cat#BAF210

Continued

REAGENT or RESOURCE	SOURCE	IDENTIFIER
Trappin-2/Elafin, Detection Antibody	R&D Systems	Cat#BAF1747
IL-17A, Detection Antibody	R&D Systems	Cat#BAF317
CXCL10/IP-10, Detection Antibody	Peprotech	Cat#500-P93BT
S100A8, Detection Antibody	R&D Systems	Cat#DS8900
IL-22, Detection Antibody	Peprotech	Cat#500-P211BT
CXCL5/ENA-78, Detection Antibody	R&D Systems	Cat#BAF254
IL-6, Detection Antibody	R&D Systems	Cat#BAF206
CCL7/MCP-3, Detection Antibody	R&D Systems	Cat#BAF282
Critical Commercial Assays		
MTT assay	Roche	Cat#11465007001
Luna Universal One-Step RT-qPCR Kit	New England Biolabs	Cat#E3005L
CellTiter-Glo Luminescent Cell Viability Assay	Promega	Cat#G7570
Direct-zol RNA Miniprep Plus kit	Zymo Research	Cat#R2072
KAPA SYBR FAST qPCR Master Mix	Roche	Cat#07959389001
Bio-Rad II Protein Assay Kit	Bio-Rad	Cat#5000002
Deposited Data		
Phosphoproteomics data of SARS-CoV-2 infected Vero E6 cells	This paper	PRIDE Project ID: PXD019113
Supplemental Tables in Mendeley Data	This paper	https://dx.doi.org/10.17632/dpkbh2g9hy.1
CORUM v3.0	Giurgiu et al., 2019	http://mips.helmholtz-muenchen.de/corum/
RNA-seq dataset for transcription factor activities	Blanco-Melo et al., 2020	GSE147507
Phosphoproteomics datasets of biological conditions	Ochoa et al., 2016	https://www.embopress.org/doi/full/10.15252/msb.20167295
Functional scores for phosphorylation sites	Ochoa et al., 2020	https://idp.nature.com/authorize?response_type=cookie&client_id=grover&redirect_uri=https%3A%2F%2Fwww.nature.com%2Farticles%2Fs41587-019-0344-3
Gene identifier mapping database from BioMart	Ensembl	http://uswest.ensembl.org/biomart/martview/5ccd994c794265409f21c6194730ce5b
Molecular Signatures Database for gene set enrichment analysis	Subramanian et al., 2005	https://www.gsea-msigdb.org/gsea/msigdb/index.jsp
Kinase-substrate relationships	Bachman et al., 2019	https://www.biorxiv.org/content/10.1101/822668v3.full
Chlorocebus proteome sequences for peptide searches	Uniprot	https://www.uniprot.org/proteomes/UP000029965
Sars-CoV-2 genomic sequences (hCoV-19/France/IDF0372/2020)	GISAID	Accession number EPI_ISL_406596
Experimental Models: Cell Lines		
ACE2-A549 human lung carcinoma	Donated from the laboratory of Brad Rosenberg	N/A
Caco-2	ATCC	Cat#HTB-37
VERO C1008 [Vero 76, clone E6, Vero E6] (Vero E6)	ATCC	Cat#CRL-1586
HEK293T/17 cells	ATCC	Cat#CRL-11268

(Continued on next page)

Continued

REAGENT or RESOURCE	SOURCE	IDENTIFIER
Oligonucleotides		
ON-TARGETplus Human MAPK12 (6300) siRNA - SMARTpool, 5 nmol	Horizon Discovery/Dharmacon	Cat#L-003590-00-0005
ON-TARGETplus Human MAPK13 (5603) siRNA - SMARTpool, 5 nmol	Horizon Discovery/Dharmacon	Cat#L-003591-00-0005
ON-TARGETplus Human MAP2K3 (5606) siRNA - SMARTpool, 5 nmol	Horizon Discovery/Dharmacon	Cat#L-003509-00-0005
ON-TARGETplus Human ACE2 (59272) siRNA - SMARTpool	Horizon Discovery/Dharmacon	Cat#L-005755-00-0005
N gene region (reverse) 5′-CGAAGGTGTGACTTCCATG-3′	Eurofins	N/A
N gene region (forward) 5′-TAATCAGACAAGGAACTGATTA-3′	Eurofins	N/A
Recombinant DNA		
pLVX-TetOne-Puro empty vector	Takara	Cat#631847
pLVX-TetOne-Puro-SARS-CoV-2-N-2xStrep	This paper	N/A
pMD2.G, Addgene	Gift from Didier Trono	Addgene Plasmid #12259
Gag-Pol-Tat-Rev packaging construct	Gift from Judd Hultquist	pJH045
Software and Algorithms		
artMS	Bioconductor	https://www.bioconductor.org/packages/release/bioc/html/artMS.html
MSstats	Bioconductor	https://www.bioconductor.org/packages/release/bioc/html/artMS.html
The R Project for Statistical Computing	R Core Team, 2019	http://www.r-project.org/index.html
Spectronaut	Biognosys	https://biognosys.com/shop/spectronaut
ZEN (Blue edition)	Carl Zeiss Microscopy	https://www.zeiss.com/zen
SPPIDER v2	Porollo and Meller, 2007	http://sppider.cchmc.org/
DoRothEA	Garcia-Alonso et al., 2019	https://saezlab.github.io/dorothea/
VIPER	Alvarez et al., 2016	https://www.bioconductor.org/packages/release/bioc/html/viper.html
Biostrings	Bioconductor	https://bioconductor.org/packages/release/bioc/html/Biostrings.html
clusterProfiler	Bioconductor	https://bioconductor.org/packages/release/bioc/html/clusterProfiler.html
DESeq2 package	Love et al., 2014	http://bioconductor.org/packages/release/bioc/html/DESeq2.html
Imaris 64x 9.5.1	Oxford Instruments	https://imaris.oxinst.com/
MetaMorph (Version 7.8)	Molecular Devices	https://www.moleculardevices.com/
Other		
Orbitrap Exploris 480 MS with internal calibration option	Thermo Fisher Scientific	Cat#BRE725533
ZEISS LSM 800 Confocal Laser Scanning Microscope	Carl Zeiss Microscopy	Model#ZEISS LSM 800
QuantStudio 6 Real-Time PCR System	Applied Biosystems	Cat#4485697
FACSymphony	BD Life Sciences	N/A
Infinity 2000 Plate Reader	Tecan	N/A
Luminex MAGPIX platform	Luminex Corp	N/A
LightCycler 480 Instrument II	Roche	N/A
Bal-Tec Drier	Balzers, Liechtenstein	Cat#CPD 030

(Continued on next page)

Continued

REAGENT or RESOURCE	SOURCE	IDENTIFIER
Quorum sputter coater	Electron Microscopy Sciences, Hatfield, PA	Cat#EMS300T D
Hitachi field emission scanning electron microscope	Hitachi, Tokyo, Japan	Model#SU-8000
Leica UC7 ultramicrotome	Leica Microsystems	N/A
FEI BT Tecnai transmission electron microscope	Thermofisher/FEI	N/A
Gatan Rio camera	Gatan	N/A
Celigo imaging cytometer	Nexcelcom	N/A

RESOURCE AVAILABILITY

Lead Contact
Further information and requests for resources and reagents should be directed to and will be fulfilled by Nevan J. Krogan (Nevan.Krogan@ucsf.edu).

Materials Availability
Plasmid pLVX-TetOne-Puro-SARS-CoV-2-N-2xStrep is available upon request from the Lead Contact.

Data and Code Availability
The mass spectrometry proteomics data have been deposited to the ProteomeXchange Consortium via the PRIDE partner repository with the dataset identifier PXD019113 (Perez-Riverol et al., 2019). An interactive version of phosphorylation data can be found at https://kroganlab.ucsf.edu/network-maps. Supplementary tables have been deposited to Mendeley Data: https://dx.doi.org/10.17632/dpkbh2g9hy.1.

EXPERIMENTAL MODEL AND SUBJECT DETAILS

Cells
African green monkey kidney epithelial Vero E6 (Vero 76, clone E6, Vero E6, ATCC® CRL-1586) authenticated by ATCC and tested negative for mycoplasma contamination prior to commencement were maintained in a humidified atmosphere at 37°C with 5% CO_2, in Dulbecco's modified Eagle's medium (DMEM) containing 10% (v/v) fetal bovine serum (FBS, Invitrogen). ACE2-expressing A549 cells, a human lung epithelial cell line, were a kind gift from Brad Rosenberg. A549-ACE2 cells were cultured in DMEM supplemented with 10% FBS and maintained at 37°C with 5% CO_2. Caco-2 (ATCC® HTB-37) human colon epithelial cells were maintained in a humidified atmosphere at 37°C with 5% CO_2 in DMEM-containing 20% (v/v) FBS.

Viruses (Institut Pasteur, Paris)
The SARS-CoV-2 isolate BetaCoV/France/IDF0372/2020 was supplied by the National Reference Centre for Respiratory Viruses hosted by Institut Pasteur (Paris, France) and headed by Pr. Sylvie van der Werf. The isolate originated from a human sample provided by Dr. X. Lescure and Pr. Y. Yazdanpanah from the Bichat Hospital, Paris, France. The isolate was supplied through the European Virus Archive goes Global (EVAg) platform. Viral stocks were prepared by propagation in Vero E6 cells in DMEM supplemented with 2% FBS. Viral titers were determined by plaque assay in Minimum Essential Media (MEM) supplemented with 2% (v/v) FBS (Invitrogen) and 0.05% agarose. All experiments involving live SARS-CoV-2 were performed in compliance with Institut Pasteur Paris's guidelines for Biosafety Level 3 (BSL-3) containment procedures in approved laboratories. All experiments were performed in at least three biologically independent samples.

Viruses (Mount Sinai, New York)
For infection experiments in ACE2-A549 cells, SARS-CoV-2, isolate USA-WA1/2020 (NR-52281), which shares 99.983% sequence identity with the BetaCoV/France/IDF0372/2020 isolate, was deposited by the Center for Disease Control and Prevention and obtained through BEI Resources, NIAID, NIH. SARS-CoV-2 was propagated in Vero E6 cells in DMEM supplemented with 2% FBS, 4.5 g/L D-glucose, 4 mM L-glutamine, 10 mM Non-Essential Amino Acids, 1 mM Sodium Pyruvate and 10 mM HEPES as described previously (Blanco-Melo et al., 2020). All work involving live SARS-CoV-2 was performed in the CDC/USDA-approved BSL-3 facility of the Global Health and Emerging Pathogens Institute at the Icahn School of Medicine at Mount Sinai in accordance with institutional biosafety requirements.

Viruses (University of Freiburg, Germany)

For infection experiments in Caco-2 cells, SARS-CoV-2 isolate Muc-IMB-1/2020, kindly provided by the Bundeswehr Institute of Microbiology, Munich, Germany, was used. SARS-CoV-2 was propagated in Vero E6 cells in DMEM supplemented with 2% FBS. All work involving live SARS-CoV-2 was performed in the BSL-3 facility of the Institute of Virology, University Hospital Freiburg, and was approved according to the German Act of Genetic Engineering by the local authority (Regierungspraesidium Tuebingen, permit UNI.FRK.05.16/05).

METHODS DETAILS

Vero E6 cell infection for proteomic analysis

Vero E6 cells were seeded using $2x10^6$ cells in T25 flasks. The following day cells were either mock infected or infected with SARS-CoV-2 at a MOI of 1 in serum-free DMEM at 37°C for 1 hour. After absorption the 0 hour samples were lysed immediately, while the media for other samples was replaced with 2% FBS / DMEM (Invitrogen) and incubated at 37°C for times indicated before lysis.

Cell lysis and digestion

Cells were lysed using 1% IGEPAL (Sigma) in PBS (Invitrogen) for 20 minutes at room temperature (RT) to inactivate the virus. These specific lysis conditions were used as this was the approved virus inactivation protocol. Proteins contained in the cell lysate were then immediately precipitated using 90% methanol (v/v) (Sigma) by centrifugation at 20,000x g for 10 minutes. The protein pellets were frozen at −80°C. Precipitated proteins were resuspended in lysis buffer (8 M urea, 100 mM ammonium bicarbonate (ABC), 150 mM NaCl, protease inhibitor (mini-cOmplete, Roche) and phosphatase inhibitors (phosSTOP, Roche). Tris-(2-carboxyethyl) phosphine (TCEP) was added to a final concentration of 4 mM. DNA was sheared via probe sonication, on ice, at 20% amplitude for 20 s., followed by 10 s of rest. This process was performed a total of three times. Following sonication, protein concentration was determined using Bradford assay. Iodoacetamide (IAA) was added to each sample to a final concentration of 10 mM, and samples were incubated in the dark at room temperature (RT) for 30 minutes. Excess IAA was quenched by the addition of dithiothreitol (DTT) to 10 mM, followed by incubation in the dark at RT for 30 minutes. Samples were then diluted with 0.1 M ABC (pH = 8.0) to a final urea concentration of 2 M. Trypsin (Promega) was added at a 1:100 (enzyme:protein w:w) ratio and digested overnight at 37°C with rotation. Following digestion, 10% trifluoroacetic acid (TFA) was added to each sample to a final pH ~2. Samples were desalted under vacuum using Sep Pak tC18 cartridges (Waters). Each cartridge was activated with 1 mL 80% acetonitrile (ACN)/0.1% TFA, then equilibrated with 3 × 1 mL of 0.1% TFA. Following sample loading, cartridges were washed with 4 × 1 mL of 0.1% TFA, and samples were eluted with 4 × 0.5 mL 50% ACN/0.25% formic acid (FA). 20 μg of each sample was kept for protein abundance measurements, and the remainder was used for phosphopeptide enrichment. Samples were dried by vacuum centrifugation.

Phosphopeptide enrichment

For each sample batch, 400 μL (30 μL per sample) of 50% Superflow bead slurry (QIAGEN) was added to a 2 mL bio-spin column. Beads were incubated with 4 × 500 μL of 100 mM EDTA for 30 s, washed with 2 × 500 μL H$_2$O, incubated 4 × 500 μL with 15 mM FeCl$_3$ for 1 minute, washed 3 × 500 μL H$_2$O, and washed once with 500 μL of 0.5% FA to remove residual Fe. Beads were resuspended in 600 μL of H$_2$O and 60 μL were aliquoted into a C18 NEST column that had been equilibrated with 150 μL of 80% ACN, 0.1% TFA. 1 mg of digested peptides were resuspended in 75% ACN/0.15% TFA and incubated with beads for 2 minutes, mixed by pipetting and incubated again for 2 minutes. Beads were washed 4 × 200 μL with 80% ACN, 0.1% TFA, then washed 3 × 200 uL with 0.5% FA, incubated 2 × 200 μL with 500 mM potassium phosphate buffer pH 7 and incubated 2 × 200 μL with 0.5% FA for 15 seconds. Phosphopeptides were eluted by centrifugation at 3000 RPM for 30 seconds with 2 × 75 uL of 50% ACN, 0.1% FA.

Mass spectrometry data acquisition

Digested samples were analyzed on an Orbitrap Exploris 480 mass spectrometry system (Thermo Fisher Scientific) equipped with an Easy nLC 1200 ultra-high pressure liquid chromatography system (Thermo Fisher Scientific) interfaced via a Nanospray Flex nano-electrospray source. For all analyses, samples were injected on a C18 reverse phase column (25 cm x 75 μm packed with ReprosilPur 1.9 μm particles). Mobile phase A consisted of 0.1% FA, and mobile phase B consisted of 0.1% FA/80% ACN. Peptides were separated by an organic gradient from 5% to 30% mobile phase B over 112 minutes followed by an increase to 58% B over 12 minutes, then held at 90% B for 16 minutes at a flow rate of 350 nL/minute. Analytical columns were equilibrated with 6 μL of mobile phase A. To build a spectral library, one sample from each set of biological replicates was acquired in a data dependent manner. Data dependent analysis (DDA) was performed by acquiring a full scan over a m/z range of 400-1000 in the Orbitrap at 60,000 resolving power (@200 m/z) with a normalized AGC target of 300%, an RF lens setting of 40%, and a maximum ion injection time of 60 ms. Dynamic exclusion was set to 60 seconds, with a 10 ppm exclusion width setting. Peptides with charge states 2-6 were selected for MS/MS interrogation using higher energy collisional dissociation (HCD), with 20 MS/MS scans per cycle. For phosphopeptide enriched samples, MS/MS scans were analyzed in the Orbitrap using isolation width of 1.3 m/z, normalized HCD collision energy of 30%, normalized AGC of 200% at a resolving power of 30,000 with a 54 ms maximum ion injection time. Similar settings were used for data dependent analysis of samples used to determine protein abundance, with an MS/MS resolving power of 15,000 and a 22 ms maximum ion injection time. Data-independent analysis (DIA) was performed on all samples. An MS scan at 60,000 resolving power over a scan

range of 390-1010 m/z, a normalized AGC target of 300%, an RF lens setting of 40%, and a maximum injection time of 60 ms was acquired, followed by DIA scans using 8 m/z isolation windows over 400-1000 m/z at a normalized HCD collision energy of 27%. Loop control was set to All. For phosphopeptide enriched samples, data were collected using a resolving power of 30,000 and a maximum ion injection time of 54 ms. Protein abundance samples were collected using a resolving power of 15,000 and a maximum ion injection time of 22 ms.

Spectral library generation and raw data processing

Raw mass spectrometry data from each DDA dataset were used to build separate libraries for DIA searches using the Pulsar search engine integrated into Spectronaut version 13.12.200217.43655 (Bruderer et al., 2015) by searching against a database of Uniprot *Chlorocebus* sequences (19,136 proteins, downloaded April 3, 2020) and 29 SARS-CoV-2 protein sequences translated from genomic sequence downloaded from GISAID (accession EPI_ISL_406596, downloaded April 7, 2020) with two mutations (G22661T Spike V367F and G26144T ORF3a G251V) detected by RNASeq analysis of virus stocks. For protein abundance samples, data were searched using the default BGS settings, variable modification of methionine oxidation, static modification of carbamido-methyl cysteine, and filtering to a final 1% false discovery rate (FDR) at the peptide, peptide spectrum match (PSM), and protein level (Elias and Gygi 2007). For phosphopeptide enriched samples, BGS settings were modified to include phosphorylation of S, T, and Y as a variable modification. The generated search libraries were used to search the DIA data. For protein abundance samples, default BGS settings were used, with no data normalization performed. For phosphopeptide enriched samples, the Significant PTM default settings were used, with no data normalization performed, and the DIA-specific PTM site localization score in Spectronaut was applied.

Immunofluorescence microscopy

Caco-2 cells seeded on glass coverslips were infected with SARS-CoV-2 Isolate Muc-IMB-1/2020, second passage on Vero E6 cells (2×10^6 PFU/mL) at an MOI of 0.1 or 0.01. At 24 hours post-infection cells were washed with PBS and fixed in 4% paraformaldehyde in PBS for 20 minutes at RT, followed by permeabilization with 0.3% Triton X-100 in PBS for 10 minutes at RT and blocking in 5% fetal calf serum in PBS for 1 hour at RT. Incubation with primary antibodies against CK2α (Abcam, ab70774, 1:500), SARS-CoV membrane (M) protein (Rockland, #100-401-A55, 1:500) and SARS-CoV nucleocapsid (N) protein (Rockland, #200-401-A50, 1:1000) was performed for 1 hour at RT. After washing with PBS, cells were incubated with AF568-labeled goat-anti-rabbit (Invitrogen, #A11011) and AF647-labeled goat-anti-mouse (Invitrogen, #A21235) secondary antibodies (1:200) as well as AF488-labeled Phalloidin (Hypermol, #8813-01, 1:250) for 2 hours at RT. Fluorescence images were generated using a LSM800 confocal laser-scanning microscope (Zeiss) equipped with a 63X, 1.4 NA oil objective and Airyscan detector and the Zen blue software (Zeiss) and processed with Zen blue software and ImageJ/Fiji. For 3D-reconstruction, cells were fixed and stained as indicated and imaged as z stack with 0.15 μm sections. Z stack was processed using Imaris software 64x 9.5.1 and displayed as MIP. To quantify colocalization between casein kinase II and N protein colocalization events in filopodia of SARS-CoV-2 infected Caco-2 cells were counted. 42 ± 19 % of the N protein particles detected in filopodia colocalize with CK2. Length of filopodia was measured using Metamorph (Version 7.8). Distance was measured starting at cortical actin to the tip of Filopodia.

Electron microscopy

Vero E6 cells were seeded overnight and then infected for 24 hours with SARS-CoV-2 isolate nCoV-WA1-2020 on silicon chips for scanning electron microscopy or Thermanox for transmission electron microscopy. For *scanning electron microscopy (SEM)*, cells were fixed with Karnovsky's formulation of 2% paraformaldehyde/2.5% glutaraldehyde in 0.1 M Sorenson's phosphate buffer, and then post-fixed with 1.0% osmium tetroxide/0.8% potassium ferrocyanide in 0.1 M sodium cacodylate buffer washed with 0.1 M sodium cacodylate buffer then stained with 1% tannic acid in dH_2O. After additional buffer washes, the samples were further osmicated with 2% osmium tetroxide in 0.1M sodium cacodylate, then washed with dH_2O. Specimens were dehydrated with a graded ethanol series from 50%, 75%, 100% x 3 for 5 minutes each, critical point dried under CO_2 in a Bal-Tec model CPD 030 Drier (Balzers, Liechtenstein), mounted with double sided carbon tape on aluminum specimen mounts (Ted Pella), and sputter coated with 35 Å of iridium in a Quorum EMS300T D sputter coater (Electron Microscopy Sciences, Hatfield, PA) prior to viewing at 5 kV in a Hitachi SU-8000 field emission scanning electron microscope (Hitachi, Tokyo, Japan). For *transmission electron microscopy (TEM)*, specimens were fixed as described above for scanning electron microscopy and additionally stained overnight with 1% uranyl acetate at 4°C after the second osmium staining and then dehydrated with the same graded ethanol series, and embedded in Spurr's resin. Thin sections were cut with a Leica UC7 ultramicrotome (Buffalo Grove, IL) prior to viewing at 120 kV on a FEI BT Tecnai transmission electron microscope (Thermofisher/FEI, Hillsboro, OR). Digital images were acquired with a Gatan Rio camera (Gatan, Pleasanton, CA).

N overexpression in Vero E6 cells

The N-protein cassette was subcloned from pLVX-EF1a-SARS-CoV-2-N-2xStrep-IRES-Puro (Gordon et al., 2020) into pLVX-TetOne-Puro (Takara) using the restriction enzymes EcoRI and BamHI to create pLVX-TetOne-Puro-SARS-CoV-2-N-2xStrep. Sequence integrity was confirmed by Sanger sequencing (GeneWiz). To produce lentiviruses, HEK293T cells (50% confluent in a T175 flask) were transfected with 5 μg of each of the pLVX-TetOne-Puro lentiviral plasmids, 3.33 μg Gag-Pol packaging construct,

and 1.66 μg VSV-G envelope (pMD2.G, Addgene) using PolyJet (SignaGen). Culture supernatant was precipitated with a final concentration of 8.5% PEG-6000 and 0.3M sodium chloride (NaCl), incubated at 4°C for 2-4 hours. Virions were pelleted at 3500 rpm for 20 minutes in a spin bucket rotor, suspended in 0.5 mL 1xPBS, and aliquoted for storage at 80°C. Vero E6 cells were seeded in T75 flasks at 50% confluence and transduced with 200 μL precipitated lentivirus derived from pLVX-TetOne-Puro-SARS-CoV-2-N-2xStrep or pLVX-TetOne-Puro empty vector. 48 hours post transduction, 10 μg/mL Puromycin was added to cultures to select transduced cells. Polyclonal stable cell lines were seeded into 15 cm dishes in triplicate and treated with 1 μg/mL doxycycline for 48 hours. Cells were washed in ice cold PBS and harvested by scraping in cold PBS. Cell pellets were lysed directly (8 M urea, 100 mM ammonium bicarbonate (ABC), 150 mM NaCl, protease inhibitor (mini-cOmplete, Roche) and phosphatase inhibitors (phosSTOP, Roche), and protein digestion and phosphopeptide enrichment was performed as described above for SARS-CoV-2 infected Vero E6 cells. During the analysis, one of three replicates of the N-overexpressed samples was found to be an outlier based on principal component analysis (as in Figures S1A and S1B) and was removed. N-overexpression (n = 2) was compared to empty vector (EV) controls (n = 3) during analysis (full data available in Table S1). Kinase activity predictions were also performed the same as for viral infection phosphoproteomics (full data available in Table S4).

Cell cycle analysis

$1x10^5$ Vero E6 cells were seeded per sample. The following day cells were either mock infected or infected with SARS-CoV-2 (isolate BetaCoV/France/IDF0372/2020) at an MOI of 1. The samples were incubated for 24 hours before detaching cells using Trypsin 0.05% (Thermo). Cells were pelleted at 500x g for 2 minutes, followed by fixation using 4% Formalin (Thermo) for 30 minutes. Cells were washed 2x with PBS (Thermo) before permeabilizing using 0.1% Triton X-100 (Thermo) for 20 minutes. Finally, cells were pelleted again and incubated with 1 mg/mL 4′,6-diamidino-2-phenylindole (DAPI; Thermo) in PBS for 30 minutes before analyzing cell cycle using fluorescence by flow cytometry using the BD FACSymphony with a violet laser (405 nm) and 450/50 nm filter. Gating was performed by first selecting singlets by gating highly correlated cells in an SSC-A versus SSC-H plot. Next, typical cellular morphology was gated using a FSC-A versus SSC-A plot. These singles were then used to draw histograms which were gated for G0/G1, S, and G2/M phases.

SARS-CoV-2 infections in ACE2-A549 cells and lysis for cytokine analysis

Approximately 5×10^5 A549-ACE2 cells were pre-treated with either DMSO or SB203580 (0.01, 0.1, 1, 10 μM final concentration). After 1 hour of pre-treatment, cells were infected with SARS-CoV-2 (isolate USA-WA1/2020) at an MOI of 0.1 while maintaining inhibitor concentrations in the media for 30 hours post infection. The supernatants from infected cells were analyzed by multiplexed ELISA for the presence of secreted cytokines and chemokines. For RNA analysis, cells were lysed in TRIzol and total RNA was extracted and DNase treated using the Direct-zol RNA Miniprep Plus kit (Zymo Research) according to the manufacturer's instructions. For protein analysis, whole cell lysates were obtained by lysis in RIPA buffer and analyzed by SDS-PAGE and western blot.

Cytokine RT-qPCR analysis

Gene expression of selected cytokines as well as SARS-CoV-2 replication was quantified by RT-qPCR. Reverse transcription of extracted total RNA samples was performed using oligo (dT) primers and SuperScript IV Reverse Transcriptase according to the manufacturer's instructions. Quantitative real-time PCR analysis of cDNA samples was performed using KAPA SYBR FAST qPCR Master Mix (2X) Universal on a LightCycler 480 Instrument II (Roche). For viral quantification, primers specifically targeting the subgenomic viral N RNA were used. ΔCT values were determined relative to the ACTB and ΔΔCT values were normalized to the average of mock infected samples (for host genes) or to infected DMSO treated samples (for viral replication). Error bars indicate the standard deviation of the mean from three independent biological replicates.

Multiplexed cytokine ELISA

Supernatants from infected cells were evaluated for 34 cytokines/chemokines by multiplex ELISA for the following analytes: CCL2/MCP-1, CCL3/MIP-1α, CCL4/MIP-1β, CCL5/RANTES, CCL7/MCP-3, CCL8/MCP-2, CCL11/Eotaxin, CCL13/MCP-4, CCL20/MIP-3α, CXCL1/GROα, CXCL2/GROβ, CXCL5/ENA-78, CXCL8/IL-8, CXCL9/MIG, CXCL10/IP-10, CXCL16, IL-1α, IL-1β, IL-1RA, IL-4, IL-6, IL-7, IL-10, IL-12p70, IL-15, IL-16, IL-17A, IL-22, GM-CSF, MMP-9, S100A8, TNFα, TGFβ, and Trappin-2/Elafin. All antibodies and cytokine standards were purchased as antibody pairs from R&D Systems (Minneapolis, MN) or Peprotech (Rocky Hill, NJ). Individual magnetic Luminex bead sets (Luminex Corp, CA) were coupled to cytokine-specific capture antibodies according to the manufacturer's recommendations. Samples were analyzed on a Luminex MAGPIX platform and quantified using a standard curve. For each bead region, > 50 beads were collected per analyte. The median fluorescence intensity of these beads was recorded for each bead and was used for analysis using a custom R script and a 5P regression algorithm.

SARS-CoV-2 viral quantification via antibody staining in presence of inhibitors

(Mount Sinai, New York). Two thousand (2,000) Vero E6 cells were seeded into 96-well plates and incubated for 24 hours. Two hours before infection, the medium was replaced with 100 μL of DMEM (2% FBS) containing the compound of interest at concentrations 50% greater than those indicated, including a DMSO control. Plates were then transferred into the BSL-3 facility and 100 PFU of SARS-CoV-2 (MOI 0.025) was added in 50 μL of DMEM (2% FBS), bringing the final compound concentration to those indicated.

Plates were then incubated for 48 hours at 37°C. After infection, supernatants were removed and cells were fixed with 4% formaldehyde for 24 hours prior to being removed from the BSL-3 facility. The cells were then immunostained for the viral NP protein (antisera produced in the Garcia-Sastre lab; 1:10,000) with a DAPI counterstain. Infected cells (488 nM) and total cells (DAPI) were quantified using the Celigo (Nexcelcom) imaging cytometer. Infectivity was measured by the accumulation of viral NP protein in the nucleus of the Vero E6 cells (fluorescence accumulation). Percent infection was quantified as ((Infected cells/Total cells) - Background) *100 and the DMSO control was then set to 100% infection for analysis. The IC_{50} for each experiment was determined using the Prism software (GraphPad). For select inhibitors, infected supernatants were assayed for infectious viral titer using the Median Tissue Culture Infectious Dose $TCID_{50}$ method. For this, infectious supernatants were collected at 48 hours post infection and frozen at $-80°C$ until later use. Infectious titers were quantified by limiting dilution titration on Vero E6 cells. Briefly, Vero E6 cells were seeded in 96-well plates at 20,000 cells/well. The next day, SARS-CoV-2-containing supernatant was applied at serial 10-fold dilutions ranging from 10^{-1} to 10^{-6} and, after 5 days, viral CPE was detected by staining cell monolayers with crystal violet. $TCID_{50}$/mL was calculated using the method of Reed and Muench.

Cytotoxicity cell viability assays

(Mount Sinai, New York). Cytotoxicity was also performed using the MTT assay (Roche), according to the manufacturer's instructions. Cytotoxicity was performed in uninfected Vero E6 cells with same compound dilutions and concurrent with viral replication assay. All assays were performed in biologically independent triplicates.

siRNA-based knockdown of host kinases

(Institut Pasteur, Paris). Host kinases were knocked-down in A549 cells stably expressing ACE2 cells using OnTargetPlus siRNA SMARTpools (Horizon Discovery). Briefly, A549-ACE2 cells seeded at $2x10^4$ cells/well in 96-well plates 18 hours prior to the experiment. The next day, each well was transfected with 6 pmoles of siRNA SMARTpool, using Lipofectamine RNAiMAX (Thermo Fisher Scientific) according to the manufacturer's instructions. Twenty-four (24) hours post transfection, the cell culture supernatant was removed and replaced with virus inoculum (MOI of 0.1 PFU/cell). Following a 1 hour adsorption at 37°C, the virus inoculum was removed and replaced with fresh Opti-MEM media (Thermo Fisher Scientific) containing 2% FBS (v/v). Seventy-two (72) hours post-infection (p.i.), the cell culture supernatant was heat-inactivated at 95°C for 5 minutes, and detection of viral genomes performed by RT-qPCR.

SARS-CoV-2 viral quantification via RT-qPCR in presence of inhibitors

(Institut Pasteur, Paris). Detection of viral genomes was performed by RT-qPCR, directly from the inactivated supernatant (Lista et al., 2020). SARS-CoV-2 specific primers targeting the N gene region: 5′-TAATCAGACAAGGAACTGATTA-3′ (Forward) and 5′-CGAAGGTGTGACTTCCATG-3′ (Reverse) (Chu et al., 2020) were used with the Luna Universal One-Step RT-qPCR Kit (NEB) in an *Applied Biosystems* QuantStudio 7 thermocycler, with the following cycling conditions: 55°C for 10 minutes, 95°C for 1 minute, and 40 cycles of 95°C for 10 s, followed by 60°C for 1 minute. The number of viral genomes is expressed as PFU equivalents/mL, and was calculated by performing a standard curve with RNA derived from a viral stock with a known viral titer.

SARS-CoV-2 titration by plaque assay

(Institut Pasteur, Paris). Vero E6 cells were seeded in 24-well plates at a concentration of $7.5x10^4$ cells/well. The following day, serial dilutions were performed in serum-free MEM media. After 1 hour absorption at 37°C, 2x overlay media was added to the inoculum to give a final concentration of 2% (v/v) FBS / MEM media and 0.05% (w/v) Agarose (all Thermo Fisher Scientific) to achieve a semi-solid overlay. Plaque assays were incubated at 37°C for 3 days. Samples were fixed using 4% Formalin (Sigma Aldrich) and plaques were visualized using crystal Violet solution (Sigma Aldrich).

siRNA Cell viability assays

(Institut Pasteur, Paris). Cell viability in siRNA knocked-down cells was measured using the CellTiter Glo luminescent cell viability assay (Promega) following the manufacturer's instructions, and luminescence measured in a Tecan Infinity 2000 plate reader. Percent viability was calculated relative to untreated cells (100% viability) and cells lysed with 20% ethanol (0% viability), included in each experiment.

QUANTIFICATION AND STATISTICAL ANALYSIS

Mass spectrometry data pre-processing

Quantitative analysis was performed in the R statistical programming language (version 3.6.1, 2019-07-05). Initial quality control analyses, including inter-run clusterings, correlations, principal components analysis, peptide and protein counts and intensities were completed with the R package artMS (version 1.5.3). Based on obvious outliers in intensities, correlations, and clusterings, 2 runs were discarded from the protein abundance data and 2 runs were discarded from the phosphopeptide data (Figure S1). Additionally, the phosphopeptide data were filtered based on feature (i.e., peptide ion) intensity, removing any single feature with intensity less than 2^{14}—this decision was made based on apparent lack of correlation between runs for feature intensities below this intensity.

Thus, for both phosphopeptides and protein abundance, we had 2 control time points and 6 infected time points, each with 3 biologically distinct replicates, except for infected at 0 and 2 hours in the phosphopeptide data and control at 0 hours and infected at 0 hours in the protein abundance data which only had 2 replicates each.

Statistical analysis of protein abundance changes between control and infected runs were computed using peptide ion fragment data output from Spectronaut and processed using a pipeline of three functions from the R package MSstats (version 3.19.5) (Choi et al., 2014): function MSstats::SpectronauttoMSstatsFormat with default settings other than setting "removeProtein_with1Feature = TRUE"; function MSstats::dataProcess with default settings other than setting "censoredInt = 0," "featureSubset = highQuality," "remove_uninformative_feature_outlier = TRUE," "clusters=7"; and function MSstats::groupComparison with all default settings.

Phosphopeptide intensity data were summarized at the peptide ion level along with confident localization of phosphorylation as described in the previous section. Quantification of phosphorylation based on peptide ions were processed using artMS as a wrapper around MSstats, via functions artMS::doSiteConversion and artMS::artmsQuantification with default settings. All peptides containing the same set of phosphorylated sites were grouped and quantified together into phosphorylation site groups. For both phosphopeptide and protein abundance MSstats pipelines, MSstats performs normalization by median equalization, imputation of missing values and median smoothing to combine intensities for multiple peptide ions or fragments into a single intensity for their protein or phosphorylation site group, and statistical tests of differences in intensity between infected and control time points.

Identifying significantly regulated proteins

When not explicitly indicated, we used defaults for MSstats for adjusted p values, even in cases of N = 2. By default, MSstats uses Student's t test for p value calculation and Benjamini-Hochberg method of FDR estimation to adjust p values. Phosphorylation fold change data were filtered for quality based on consistency of observations between treatment and controls by requiring the MSstats reported value missingPercentage < 0.60. This value is the proportion of features (i.e., peptide ions) that are missing across the treatment and control replicates for a specific fold change computation. MSstats phosphorylation results had to be further simplified to effects at single sites. The results of artMS/MSstats are fold changes of specific phosphorylation site groups detected within peptides, so one phosphorylation site can have multiple measurements if it occurs in different phosphorylation site groups (see Table S1 for examples). This complex dataset was reduced to a single fold change per site and time point by choosing (per time point) the fold change with the lowest p value, favoring those detected in both treatment and control, i.e., non-infinite $\log_2$ fold change values. This single-site dataset, further reduced to those with human orthology (Table S1), was used as the input for kinase activity analysis.

Significance filters of adjusted p value < 0.05 and absolute $\log_2$ fold change (infected/mock) > 1 were applied to both phosphorylation and abundance datasets. Additionally, for protein abundance data, if a protein was detected in only infected but not mock, or vice versa, we required detection in 3 replicates or by 3 peptide ion fragments in at least 2 replicates. These significance-filtered data were used for enrichment analyses and counts of significant effects (Figure 1).

Mapping C. sabaeus and *H. sapiens* proteins

Orthologous pairs of gene identifiers between *C.sabaeus* and *H.sapiens* were downloaded from Ensembl using the BioMart web interface (http://uswest.ensembl.org/biomart/martview/6c48d59058381e6b2b198a1f91ba5e50) on April 6, 2020. Ensembl gene identifiers were mapped to UniProt identifiers and protein sequences using a table of ID mappings and reference proteome sequences for *H.sapiens* downloaded from Uniprot on April 6, 2020. Orthologous pairs of sequences were aligned using the Needleman-Wunsch global alignment algorithm implemented in the R package Biostrings (v. 2.52) function pairwiseAlignment with default parameters. The resulting alignments were used to convert the sequence positions of detected phosphorylations in *C.sabaeus* to positions in *H.sapiens* protein sequences.

GO enrichment analysis

Sets of genes with significant up and down effects were tested for enrichment of Gene Ontology (GO Biological Process, Molecular Function and Cellular Component) terms. Sets of genes were either combined across time points (Figure 1I) or collected separately per time point (Figures S1F and S1G). The over-representation analysis (ORA) was performed using the enricher function of clusterProfiler package (version 3.12.0) in R with default parameters. The gene ontology terms were obtained from the c5 category of Molecular Signature Database (MSigDBv7.1) (Subramanian et al., 2005). Significant GO terms (adjusted p value < 0.01) were identified and further refined to select non-redundant terms. In order to select non-redundant gene sets, we first constructed a GO term tree based on distances (1-Jaccard Similarity Coefficients of shared genes in MSigDB) between the significant terms. The GO term tree was cut at a specific level (h = 0.99) to identify clusters of non-redundant gene sets. For results with multiple significant terms belonging to the same cluster, we selected the most significant term (i.e., lowest adjusted p value).

Clustering of phosphorylation changes

Phosphorylation sites with one-to-one mapping to human S, T or Y amino acids and showing significant change in phosphorylation (abs($\log_2$FC) > 1 and adjusted p value < 0.05) in one or more conditions were selected and clustered using hierarchical clustering (complete-linkage) with pearson correlation (1-r) as the distance measure. The cluster tree was cut into 5 clusters using a dynamic tree cutting method, cutreeHybrid function in dynamicTreeCut (Langfelder et al., 2008) package in R, with a minimum cluster size of 130 sites. Phosphorylated proteins in each cluster were tested for enrichment of Reactome pathways (Jassal et al., 2020). The over-

representation analysis (ORA) was based on the hypergeometric distribution and performed using the enricher function of cluster-Profiler package in R (Yu et al., 2012). The pathway terms were obtained from the c2 category (Reactome) of Molecular Signature Database (MSigDBv6.1).

Estimation of kinase activities in the time-course experiment
Kinase activities were estimated using known kinase-substrate relationships in literature (Bachman et al., 2019). The resource comprises of a comprehensive collection of phosphosite annotations of direct substrates of kinases obtained from six databases, PhosphoSitePlus, SIGNOR, HPRD, NCI-PID, Reactome, and the BEL Large Corpus, and using three text-mining tools, REACH, Sparser, and RLIMS-P. Kinase activities were inferred as a $-\log_{10}$(p value) of Z-test from the comparison of fold changes in phosphosite measurements of the known substrates against the overall distribution of fold changes across the sample. This statistical approach has been previously shown to perform well at estimating kinase activities (Hernandez-Armenta et al., 2017; Casado et al., 2013). We collected substrate annotations for 400 kinases with available data. Kinase activities for kinases with 3 or more measured substrates were considered leaving us with 97 kinases with activity estimates in at least one or more infection time points.

Comparison of phosphorylation profiles with other conditions
In addition to the time-course experiment, we also estimated kinase activities of cell line perturbation in a range of biological conditions using the K-test based approach, from a large resource of previously published phosphoproteomics datasets comprising of 435 biological conditions which include several drug treatments (chlorzoxazone, paclitaxel), inhibitors (EGFRi, AKTi) and cell cycle states (Ochoa et al., 2016). After selecting for kinase activities derived from 3 or more substrates, a total of 214 kinases had activity estimates for at least one biological condition including all 97 kinases which were estimated in the time-course experiment. Of the 435 conditions, 309 conditions with at least one kinase with significantly changing activity ($-\log_{10}$(p value) from Z-test > 2.5) were selected. Individual time points of the infection experiment were correlated with each selected biological condition based on Pearson correlation of their kinase activity profiles. Conditions with significant correlation (5% FDR) with one or more time points were identified. Several conditions corresponded to the same biological treatment (i.e., drug perturbation) in different concentrations. In such cases, the conditions are represented together with strongest correlation.

Phosphorylation of protein complexes
Annotations for protein complexes were obtained from CORUM v3.0 database (Giurgiu et al., 2019). Overall significance of changes of phosphosites of a protein complex was inferred from the $\log_2$ fold change of individual phosphosites of protein members of the complex using the same Z-test based approach described for estimation of kinase activities. Among the 3512 complexes, 1070 complexes with phosphorylation changes obtained from 4 or more phosphosites were considered. Of these, 67 complexes had significant phosphorylation change ($-\log_{10}$(p value) from Z-test > 2.5) in at least one time point. In order to select non-redundant complexes, we first constructed a complex term tree based on distances (1-Jaccard Similarity Coefficients of shared genes) between the significant complexes. The term tree was cut at a specific level (h = 0.99) to identify clusters of non-redundant complexes. The largest complex was selected from each cluster.

Transcription factor activity after SARS-CoV-2 infection
To evaluate the effect of SARS-CoV-2 infection at the Transcription Factor (TF) level, we applied DoRothEA (Garcia-Alonso et al., 2019) to RNA-seq datasets of different human lung cell lines from a recent study (GSE147507) (Blanco-Melo et al., 2020). DoRothEA is a comprehensive resource containing a curated collection of TF-target interactions. Each TF-target interaction is associated with a confidence level based on the number of supporting evidence. Here we selected the most reliable interactions (A, B, and C levels) and computed TF activities based on the normalized expression of their targets using the VIPER algorithm (Alvarez et al., 2016). For the TF activity enrichment analysis, VIPER was executed with the Wald statistic resulting from the differential expression analysis at the gene level between controls and SARS-CoV-2 infected cells using the DESeq2 package (Love et al. 2014). In VIPER, we set the eset.filter parameter to FALSE and consider five as the minimum number of targets allowed per regulon.

Pharmacological profiling dose response analysis
A hill function was fit to each dose response curve using the lsqcurvefit function in MATLAB (R2018a). IC$_{50}$ (virus) and CC$_{50}$ (cell viability) values were defined as the concentration at which the percent measure (virus or cell viability quantification) crossed the 50% mark. If the fit curve did not begin above 50% and cross to below 50% throughout the dose response, an IC$_{50}$ or CC$_{50}$ value was marked as greater than the maximum tested concentration. For TCID$_{50}$ and plaque assay results, which are not depicted in a percent scale, the IC$_{50}$ values were extracted directly from the parameterized hill equation (see Figure S5 and Table S8).
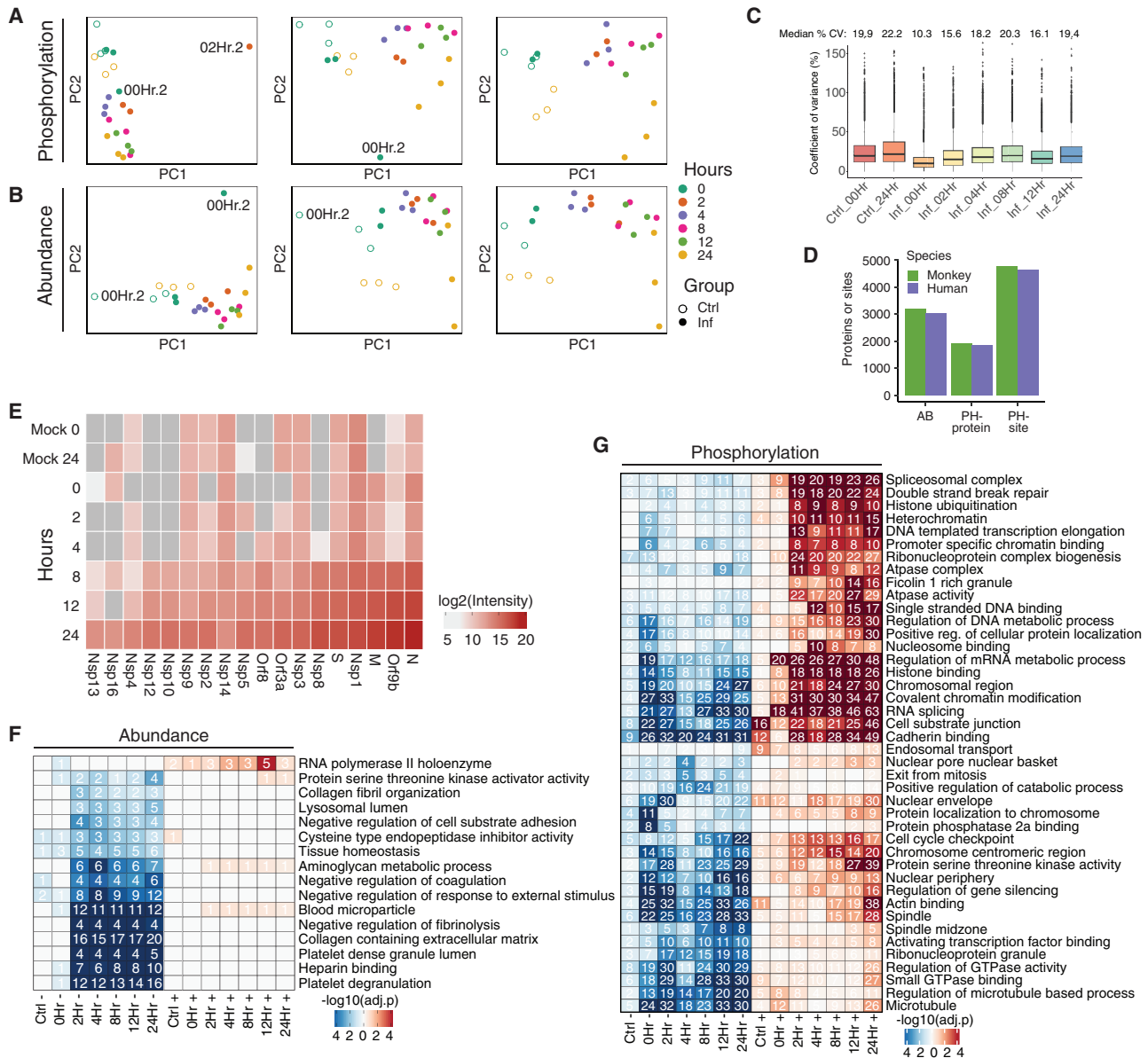
Supplemental Figures

Figure S1. Proteomics: Quality Control (QC), Orthology, Enrichments, and Viral Proteins, Related to Figure 1

(A) Principal component analysis computed on intensities summarized by MSstats at the level of phosphorylation site groups within (from left to right) all runs, with one outlier run removed, and with two outlier runs removed. Outlier runs are labeled 00Hr.2 and 02.Hr.2. (B) Principal components analysis computed on protein intensities as summarized by MSstats (from left to right) within all runs, with one outlier run removed, and with two outlier runs removed. Outlier runs are both labeled 00Hr.2; one is mock and the other is infected. (C) Coefficient of variance boxplot for each condition. Black lines depict the median and their values are indicated above each boxplot. (D) Mapping detected and quantifiable proteins and phosphorylation sites from the green monkey (Chlorocebus sabaeus) protein sequences to human genes. Proteins and sites were considered quantifiable if MSstats computed a non-infinite fold change for any time point or if an infinite $\log_2$ fold change passes criteria for inclusion in any time point. (E) Intensities of viral proteins as summarized over all peptide ion fragments by MSstats, averaged across replicates. The MSstats summarization is based on the median intensity of all fragments after data pre-processing (STAR Methods). (F) Gene Ontology enrichment analysis for proteins significantly regulated in terms of abundance upon infection, separated by time point and direction of phosphorylation regulation. All terms with significant over-representation (adjusted p value < 0.01) in the regulated gene set are kept, and redundant terms are removed (see STAR Methods). Numbers in cells indicate the number of genes that match the term for a given time point and direction. (G) Gene Ontology enrichment analysis for significantly phosphorylated proteins upon infection, separated by time point and direction of protein regulation. Details same as for (F).
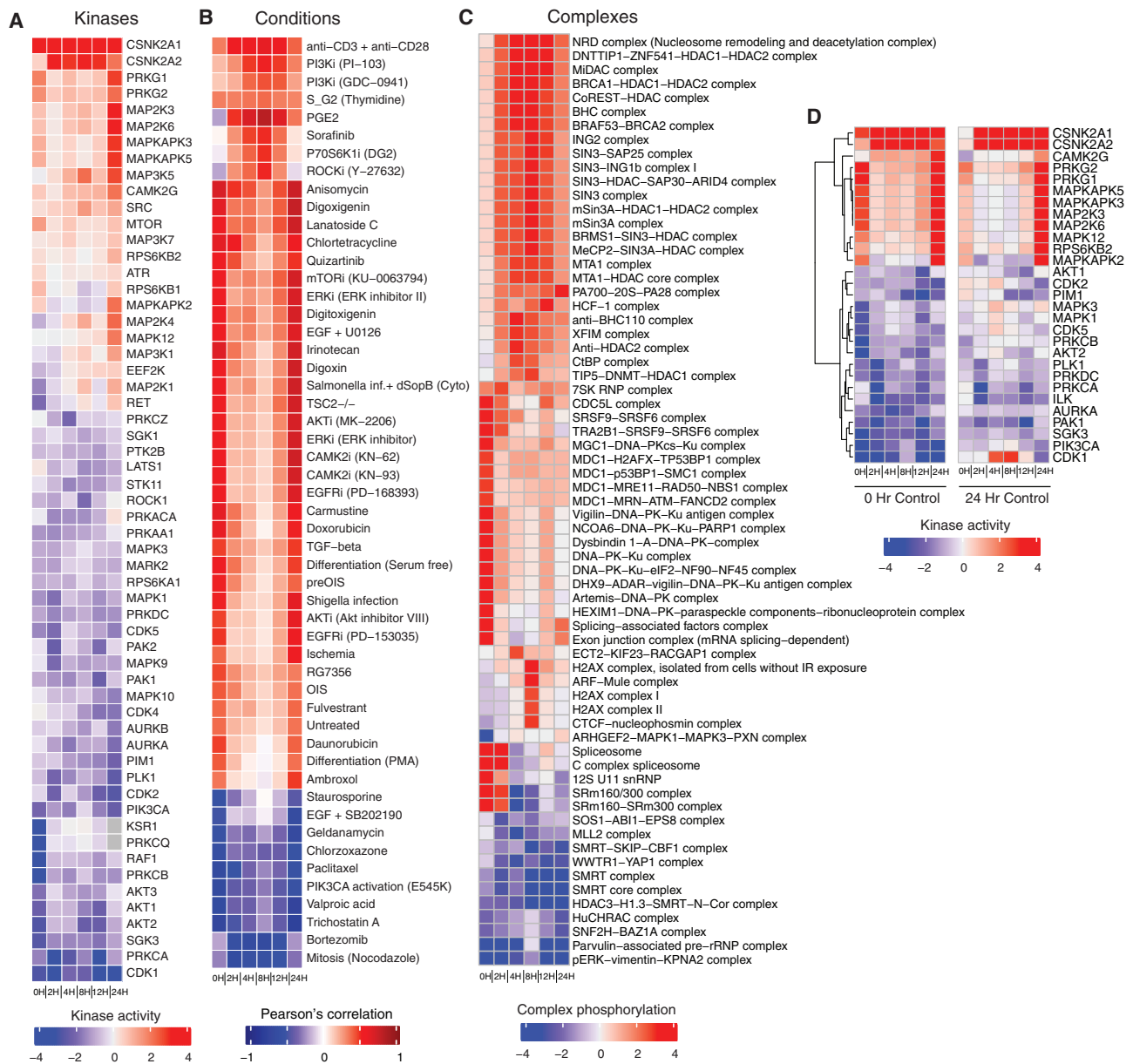
Figure S2. Full Kinase Activities, Correlated Conditions, and Regulated Complexes, Related to Figure 4

(A) Changes in predicted kinase activities across different time points post-infection. (B) Correlation of kinase activity profiles of each time point with other biological conditions. Kinase activities were estimated for a wide-range of biological conditions obtained from previously published phosphoproteomics datasets (Ochoa et al., 2016). (C) Changes in phosphorylation in protein complexes. Overall phosphorylation change (-log$_{10}$ (p value)) of a protein complex was derived from change in phosphorylation of sites in member proteins. (D) Kinase activity estimates when using either the 0- or 24-h mock controls for those top regulated kinase activities from the 0-h control comparison.
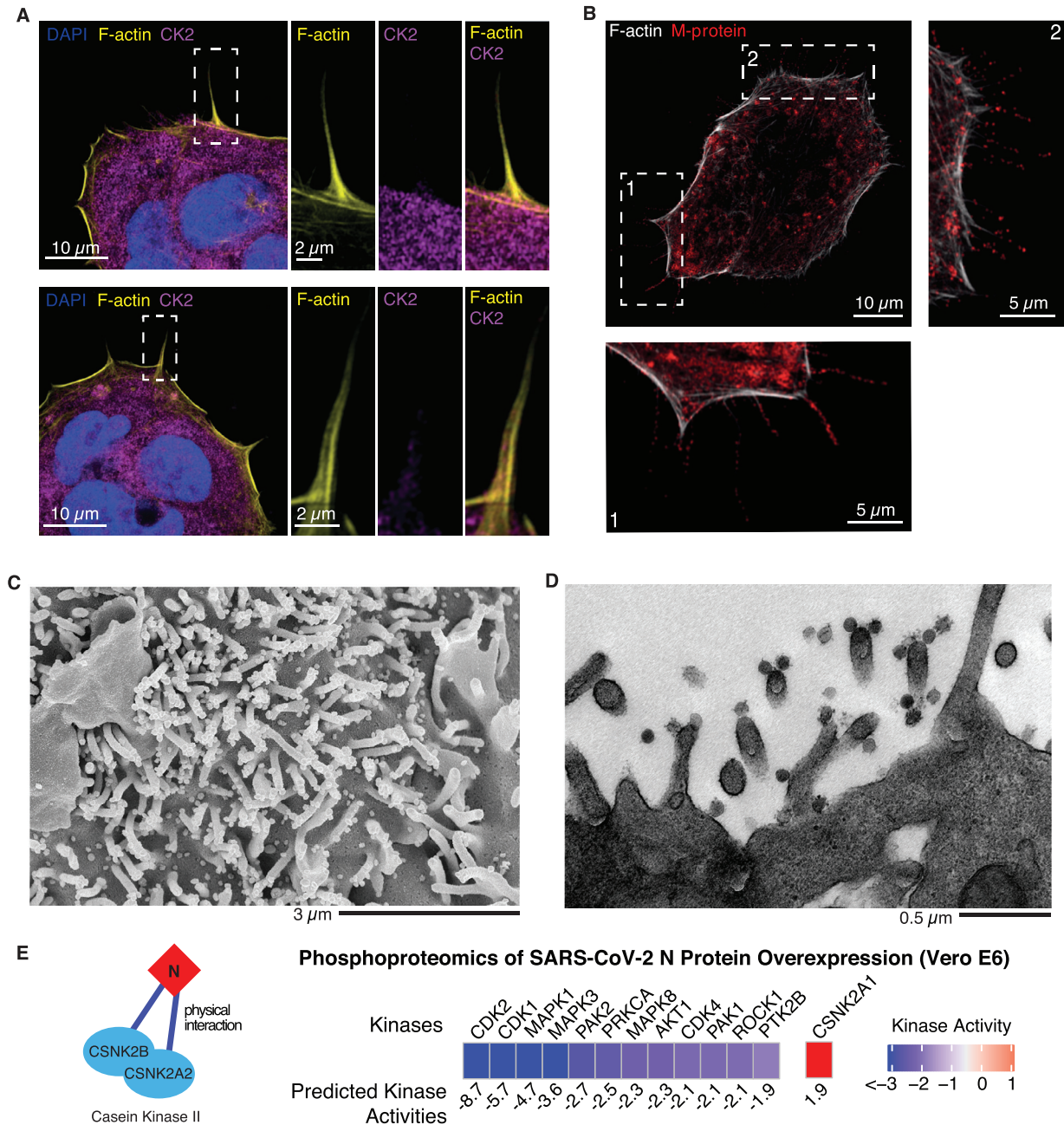
Figure S3. Microscopy Images Showing Response to SARS-CoV-2 Infection, Related to Figure 5

(A) Non-infected Caco2 cells co-stained for F-actin, CK2 and nuclei (DAPI). Magnification of the indicated area is displayed as a single channel and merged images on the right panels. (B) Caco2 cells infected with SARS-CoV-2 at an MOI of 0.1 for 24 h prior to immunostaining for F-actin and M-protein, as indicated. See lower (1) and right (2) panel for magnification of regions indicated by dashed boxes. (C) Scanning electron microscopy and (D) transmission electron microscopy image of SARS-CoV-2 budding from Vero E6 cell filopodia. (E) N protein was found to physically interact with casein kinase II subunits (cartoon, left), CSNK2B and CSNK2A2 (Gordon et al., 2020). To test whether N protein could directly control CK2 activity, N protein was transduced via lentivirus in Vero E6 cells and stably induced via doxycycline for 48 hours followed by phosphoproteomics analysis. Kinase activities were calculated as before (STAR Methods) and top up- (> 1.5, red) and downregulated (< 1.5, blue) kinases are shown. See Table S1 for full phosphoproteomics data and Table S4 for full list of predicted kinase activities.
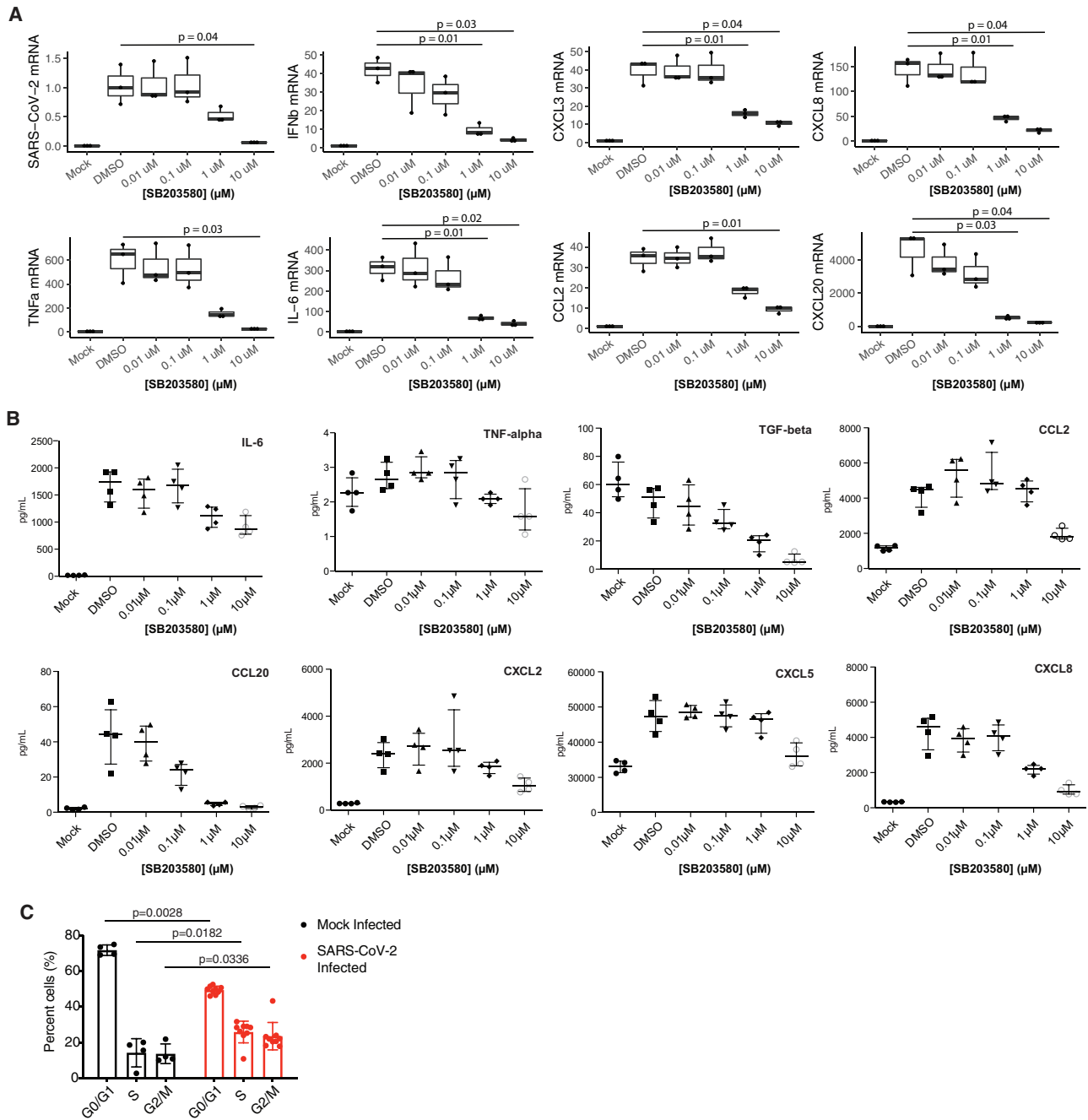
Figure S4. Cytokine Profiling upon Infection, p38 Inhibition, and Cell Cycle Analysis, Related to Figure 6
(A) RT-qPCR analysis of indicated mRNA from A549-ACE2 cells pre-treated with p38 inhibitor SB203580 at indicated concentrations for one hour prior to infection with SARS-CoV-2 for 24 hours. Statistical test is Student's t test. Error bars are SD. (B) Same as in (A) but a Luminex-based quantification of indicated cytokines. Error bars are SD. (C) Cell cycle analysis of Vero E6 cells (same as in Figure 6I) upon SARS-CoV-2 infection at an MOI of 1. Cell stained with DAPI DNA stain prior to flow cytometry analysis. Statistical test is Mann-Whitney test. Error bars are SD.

Figure S5. Pharmacological Profiling for Viral Titers and Cell Viability, Related to Figure 7

Dose response of phosphoproteomics-informed drugs and compounds. Assays performed in New York (N; red, anti-NP; blue TCID$_{50}$) and Paris (P; red, RT-qPCR; purple, plaque assays) across two cell lines (A549-ACE2 and Vero E6). Cell viability shown in black. Mean of three biological replicates is shown. Error bars are SEM.